J Mater Sci (2022) 57:14135–14187

Review

Powder bed fusion additive manufacturing of Ni-based superalloys: a review of the main microstructural constituents and characterization techniques

Michael P. Haines[1], Vitor V. Rielli[1], Sophie Primig[1,*], and Nima Haghdadi[1,*]

[1] School of Material Science and Engineering, UNSW Sydney, Sydney, NSW 2052, Australia

Received: 23 February 2022
Accepted: 27 June 2022
Published online: 27 July 2022

ABSTRACT

Metal additive manufacturing (AM) has unlocked unique opportunities for making complex Ni-based superalloy parts with reduced material waste, development costs, and production lead times. Considering the available AM methods, powder bed fusion (PBF) processes, using either laser or electron beams as high energy sources, have the potential to print complex geometries with a high level of microstructural control. PBF is highly suited for the development of next generation components for the defense, aerospace, and automotive industries. A better understanding of the as-built microstructure evolution during PBF of Ni-based superalloys is important to both industry and academia because of its impacts on mechanical, corrosion, and other technological properties, and, because it determines post-processing heat treatment requirements. The primary focus of this review is to outline the individual phase formations and morphologies in Ni-based superalloys, and their correlation to PBF printing parameters. Given the hierarchal nature of the microstructures formed during PBF, detailed descriptions of the evolution of each microstructural constituent are required to enable microstructure control. Ni-based superalloys microstructures commonly include γ, γ', γ'', δ, TCP, carbides, nitrides, oxides, and borides, dependent on their composition. A thorough characterization of these phases remains challenging due to the multi-scale microstructural hierarchy alongside with experimental challenges related to imaging secondary phases that are often nanoscale and (semi)-coherent. Hence, a detailed discussion of advanced characterization techniques is the second focus of this review, to enable a more complete understanding of the microstructural evolution in Ni-based superalloys printed using PBF. This is with an expressed goal of directing the research community toward the tools necessary for a thorough investigation of the processing-microstructure-

Handling Editor: P. Nash.

Address correspondence to E-mail: s.primig@unsw.edu.au; nima.haghdadi@unsw.edu.au

https://doi.org/10.1007/s10853-022-07501-4

property relationships in PBF Ni-based superalloy parts to enable microstructural engineering.

Introduction

Additive manufacturing (AM), also known as 3D printing, is a disruptive technology that has seen continued adoption and development in academia and industry primarily due to its ability to create complex geometries, minimize material losses, and shorten development and production lead times [1]. AM is often described as a layer-by-layer process that enables building intricate parts through the construction of multiple complex 2D layers. Due to the complex nature relating to the building of 3D geometries, the initial development and commercialization of AM did not occur until sufficiently powerful computer systems that allowed for more complicated control systems became available. Therefore, despite earlier references to the basic concept of AM, the first patents for modern AM systems did not appear until the 1980s when computer technologies began to mature [2]. A large amount of work within AM has initially aimed to develop understanding of the relationship between processing techniques and engineering properties within AM manufactured materials. These initial studies have only examined the microstructural evolution on a larger scale, e.g., via imaging defects such as porosities. This is despite AM microstructures being highly complex and hierarchical [3]. Further AM advancements are highly dependent on establishing a more complete understanding of the detailed processing-microstructure-property relationships. Currently, more research needs to be done to extend the existing understanding of the microstructural evolution across different length scales. The subsequent interest from industry will enable a systematic development of components with consistent engineered properties, regardless of part geometry.

Numerous metal alloy classes have been explored and successfully processed via AM including Fe-, Al-, Ni-, Ti-alloys, and many others [4, 5]. These alloys play a critical role in different industry sectors such as defense, aerospace, automotive, medical, and construction. Ni-based superalloys are of vital importance to many of these industries including defense and aerospace due to their excellent mechanical, creep, corrosion, and wear resistance at ambient and elevated temperatures [6, 7]. However, following conventional manufacturing routes including casting and forming, Ni-based superalloys are often difficult to process due to their complex compositions. For instance, Ni-based superalloys often need to be annealed prior to forming and machining, to promote ductility and formability, which results in a compromise in material properties [8]. Further, the complex geometries often required in typical applications of Ni-based superalloys lead to high buy-to-fly ratios due to complex machining operations, resulting in increased waste and expenditures. AM can offer increased part complexity for optimal functionality, minimized material losses, and reduced lead time of manufacturing at no extra cost [9]. For these reasons, Ni-based superalloys have recently seen extensive applied and fundamental

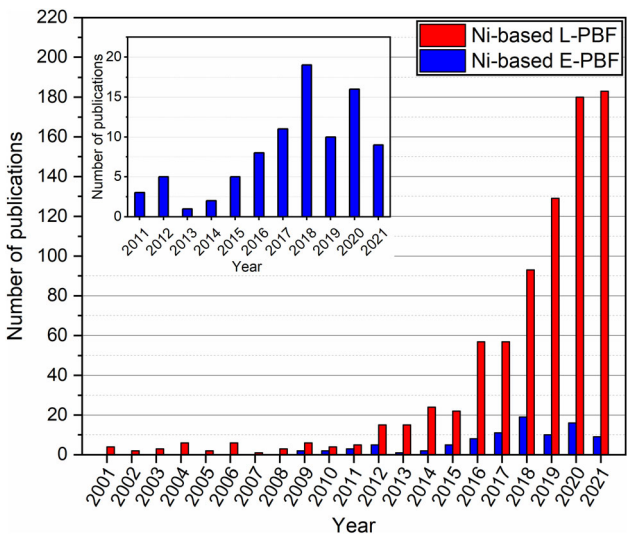

Figure 1 Number of publications in the last two decades for Ni-based superalloys processed through electron beam powder bed fusion (E-PBF) and laser powder bed fusion (L-PBF). Data were extracted from Scopus on 09 February 2022 using the following search terms for L-PBF: "L-PBF or LPBF or SLM or DMLS and Nickel" and for E-PBF: "E-PBF or EPBF or SEBM or EBM and Nickel".

research within the AM field with increasing numbers of publications in the last decade (Fig. 1).

Scope of this review

The past decade has seen numerous metal AM techniques explored, with powder bed fusion (PBF) processes and directed energy deposition (DED) seeing the most rapid development for Ni-based superalloys. There have been several reviews on the AM of metals discussing process specifics, microstructure, and/or mechanical or corrosion properties [4, 5, 9–16]. PBF has seen a large amount of development due to its ability to create complex geometries with the prospect of simplifying manufacturing routes and improving performance in many engineering applications. The PBF process involves the layer-by-layer construction of a part in a bed of powder usually attached to a substrate for structural support. Powder is spread across the substrate forming a powder bed through the use of a rake. Subsequently, an energy source is used to melt a layer of powder, based on a given part geometry using a defined scan strategy. These processes are repeated layer-by-layer to create a defined geometry. There are two types of PBF processes commonly used: laser (L-PBF) and electron (E-PBF). In L-PBF, a laser is used to melt the powder, and parts are processed under an atmosphere usually composed of either Ar or N. In E-PBF, an electron beam is used, and parts are built under vacuum. The biggest difference in process between L-PBF and E-PBF is in the cooling rates experienced. E-PBF can experience orders of magnitude lower cooling rates compared to L-PBF, with cooling rates in E-PBF ranging from 10^4 to 10^6 K/s and in L-PBF ranging from 10^5 to 10^8 K/s [17]. Multiple factors contribute to the difference in thermal conditions and melt pool properties between the processes. These include increased absorption of the electron beam compared to laser, lack of heat dissipation due to no convection effects in E-PBF, and the significantly higher preheating capabilities under E-PBF [18]. In considering these effects, the biggest difference in thermal conditions can primarily be attributed to the high preheat temperatures in E-PBF that may be used often in excess of 1000 °C [9]. These high preheat temperatures are possible under E-PBF due to the use of magnets instead of mirrors which permits the beam to move at much faster rates. A direct comparison of thermal conditions between the processes is challenging due to difficulties in obtaining in situ observations; however, detailed computational simulations can give insight into the different thermal signatures present in the two processes. Figure 2 demonstrates cooling rates for L-PBF (Fig. 2a) and E-PBF (Fig. 2b). Overall, the L-PBF process saw peak cooling rates twice that of the E-PBF process based on these simulations. Further, due to the lack of preheating, the L-PBF part cools faster compared to its E-PBF counterpart.

DED, on the other hand, can either use blown powders or wires similar to that used in welding to construct 3D parts. In the "blown powder process," powder is deposited directly onto a substrate using a carrier gas. The powder is subsequently melted with either a laser or electron beam. Wire DED processes work similar to welding processes in that a wire is melted onto a substrate. Multiple passes permit the building of a 3D structure. Compared to DED, PBF is capable of greater part complexity, accuracy, and surface finish and is, therefore, often used for making complex engine components in the aerospace industry. DED is primarily used in the construction of large scale parts [19–22] or the repair and reclamation of Ni-based superalloy components [15, 23, 24]. It does not offer the same part resolution as PBF and, therefore, is rarely used in the construction of smaller individual engineered parts [25, 26]. DED processes offer opportunities for fabricating parts with volumes of a couple cm^3 to over a m^3, resulting sometimes in large variations in the mechanical and microstructural properties [22]. Due to the large variations in type of deposition, part scale, and applications, DED processes see a large range of microstructures that deserve their own review. Therefore, our review primarily focuses on PBF processes only.

As discussed previously, Ni-based superalloys offer excellent mechanical, creep, corrosion, and wear resistance at ambient and elevated temperatures [6, 7]. Enhancement of gas turbine engines has been a driving force for the improvement of these properties since the first modern Ni-based superalloys started to appear in the 1940s [27]. Today, Ni-based superalloys typically constitute anywhere between 40 and 50% of the total weight of an aircraft engine [28]. Overall, the aerospace global market is expected to grow 30% by 2025 although this may experience some delays due to the global pandemic. However, in order to achieve a 50% reduction in aviation emissions by 2050, lighter and more efficient aircraft engines will be required

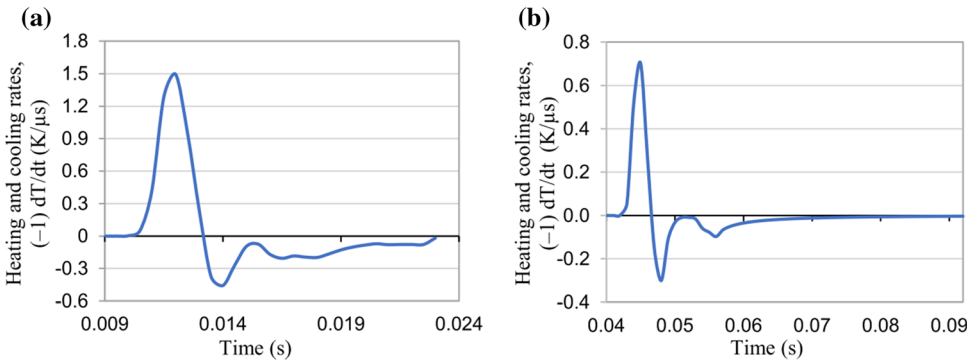

Figure 2 Finite element analysis simulated heating and cooling rates versus time plots for **a** L-PBF and **b** E-PBF. Reproduced from [18] with permission.

[29]. Complex geometries and part consolidation, enabled by AM, have the potential to provide mass reduction for load bearing structures and increased performance for turbine-based engines [30].

Reviews on Ni-based superalloys have been published on generalizations of the process-microstructure-property relationships [6, 31, 32]. Other reviews focused on individual alloys such as IN718 [33] and IN625 [34]. Graybill et al. [6] looked at the basics of DED and PBF processes and the process parameter-mechanical property relationships for Ni-based superalloys without providing a detailed overview of the microstructural properties. Sanchez et al. [31] comprehensively covered the development of mechanical properties for PBF processed Ni-based superalloys, outlining PBF process control and quality inspection, the impact of processing parameters on microstructure evolution, and the resulting mechanical properties in as-built and heat-treated states for numerous Ni-based superalloy systems. However, their review lacks discussion on the development of individual phase constituents in different Ni-based superalloys processed under PBF, and primarily focuses on the microstructures of well-established alloys such as IN718 and IN625. Adegoke et al. [32] reviewed AM of γ' strengthened Ni-based superalloys only. Their review specifically addressed cracking, microstructure, phase development, and mechanical properties for γ' forming Ni-based superalloys, but they do not cover in-depth nanoscale microstructure characterization. Hosseini et al. [33] specifically reviewed IN718, outlining microstructure development in as-built and heat-treated conditions and the resulting mechanical properties. Tian et al. [34] reviewed IN625 and its associated reported microstructure and mechanical properties. While most of these studies discuss the impact of microstructure on the mechanical properties, there is little comprehensive discussion on the phase constituents and their related hierarchical morphology that can range from the nanoscale to the macroscale. Neither do these studies discuss in detail the accompanying solidification and solid-state mechanisms (i.e., liquid–solid and solid–solid phase transformations) that influence phase formations and phase morphologies. Detailed discussions of phase constituents are critically important considering the complex morphology of the phases that form during AM of Ni-based superalloys and the significant role each of these phases play in mechanical, corrosion, and other engineering properties.

While the formation of defects can be a common occurrence within PBF, to keep the review focused on phase formation and morphology, the reader is directed toward the following works [35–38]. Further, we do not discuss mechanical properties as there have been several reviews on this subject [7, 10, 31, 33]. Lastly, we do not discuss heat treatment routines as the numerous heat treatment routines covered in literature and the resulting variation in phase constituents that occur from these routines would greatly extend the current length of the review. As such, this work will primarily focus on providing detailed descriptions of the resulting phase formation and morphology found within PBF and how different processing conditions may impact these phases. We will comparatively review in detail the different microstructure constituents found in E-PBF and L-PBF Ni-based superalloys. Specifically, we approach the review by first covering the main microstructural constituents found in Ni-based superalloys in "Overview of main microstructure constituents in common Ni-based superalloys" section, followed by a review of basic solidification and solid-state phase transformations mechanisms in relation to PBF in "Review of solidification and solid-

state phase transformations and context in AM" section. More specific discussion in the context of PBF begins at "γ matrix phase" section with the covering of the γ matrix phase. "γ' phase", "γ'' and δ phase" and "Other secondary precipitates and TCP phases" sections cover the γ', γ'' δ, other secondary precipitates, and TCP phases, respectively. We also provide an overview on hierarchical microstructure characterization from macroscale to nanoscale techniques in "Review of characterization techniques" section. We conclude this section with a case study. This will outline the tools and techniques needed to successfully characterize the microstructural evolution in PBF Ni-based superalloys, which would, in turn, enable microstructural engineering.

Overview of main microstructure constituents in common Ni-based superalloys

Unique microstructures and phase morphologies have been reported during AM due to high cooling rates and thermal cycling. Therefore, understanding of the resulting phase morphology from PBF processes has also been established. Here, a short overview on the type of Ni-based superalloys and their most common phases is given. Next, the details concerning each individual constituent are outlined in the following sections. A summary of phases that have been reported to form in Ni-based superalloys is given in Table 1. Note that not all of these phases are necessarily present in as-built AM processed materials.

Typically, Ni-based superalloys contain up to 40 wt.% of a combination of 5 to 10 different elements [28]. Further, they can be classified into solid solution and precipitate forming alloys with the latter being further broken down into primarily γ' or γ'' forming alloys [39, 40]. Hastelloy X and IN625 are examples of the most common solid solution forming alloys used in AM. IN718 is the main γ'' precipitate forming alloy used in AM and is a popular choice due to its high weldability, and its extensive prior characterization in the literature. γ' alloys are more challenging to print in AM as high γ' content is known to contribute to cracking. Most γ' alloys are processed by E-PBF where the use of high preheat temperatures can minimize cracking, however, some researchers have successfully processed alloys such as Haynes 282, Rene 41, and IN738 using L-PBF [41–44]. Overall, CMSX-4 has seen the greatest amount of research for γ' forming alloys and has even been used to successfully print single crystal microstructures using E-PBF [45, 46].

Table 1 A summary of common phases found in Ni-based superalloys [39, 48, 49]

Phase	Crystal structure	Chemical formula
γ	FCC	
γ'	FCC (ordered L_{12})	$Ni_3(Al,Ti)$
γ''	BCT (ordered $D0_{22}$)	Ni_3Nb
R	Rhombohedral	$Cr_{18}Mo_{31}Co_{51}$
P	Orthorhombic	$Cr_{18}Mo_{42}Ni_{40}$
μ	Rhombohedral	Co_2W_6, $(Fe,Co)_7(Mo,W)_6$
σ	Tetragonal	FeCr
		FeCrMo
		CrFeMoNi
		CrCo
		CrNiMo
Laves	Hexagonal	Fe_2Nb
		Fe_2Ti
		Fe_2Mo
		Co_2Ta
		Co_2Ti
MC	Cubic	TiC
		NbC
		HfC
$M_{23}C_6$	FCC	$(Cr,Fe,W,Mo)_{23}C_6$
M_6C	FCC	Fe_3Mo_3C
		Fe_3W_3C-Fe_4W_2C
		Fe_3Nb_3C
		Nb_3Co_3C
		Ta_3Co_3C
M_7C_3	Hexagonal	Cr_7C_3
M_3B_2	Tetragonal	Ta_3B_2
		V_3B_2
		Nb_3B_2
		$(Mo,Ti,Cr,Ni,Fe)_3B_2$
		Mo_2FeB_2
MN	Cubic	TiN
		(Ti,Nb,Zr)N
		(Ti,Nb,Zr)(C,N)
		ZrN
		NbN

The primary matrix phase in Ni-based superalloys is the face centered cubic (FCC) γ. This phase is often strengthened through forming a solid solution of Ni with other elements including Co, Fe, Cr, Mo, W, V, Ti, and Al. At high temperatures above 0.6 $T_{melting}$, strengthening is impacted by diffusion, thus most of

the strengthening of the γ matrix is provided by slow diffusing elements such as Mo and W. Applications for primarily solid solution strengthened alloys include industrial furnaces, and jet engine tailpipes, afterburners, turbine blades, and vanes [47].

Precipitation-hardened Ni-based superalloys typically form two different types of primary strengthening precipitates, γ' and γ''. The γ' phase is an FCC-like $L1_2$ ordered phase of the composition Ni_3X, where X is primarily the element Al [39], however Ti and Ta can often replace the Al in γ' when present [40]. With increased aging, γ' transforms from spherical to cuboidal shape [39]. Examples of γ' alloys include CMSX-4, Mar M247, Rene N5, and IN738. Because γ' is stable up to high temperatures close to the melting point of the alloy, these materials are often used in power and aerospace turbine blade applications to improve efficiency at higher service temperatures.

The γ'' phase is a body centered tetragonal (BCT) ordered $D0_{22}$ phase with a chemical composition of Ni_3Nb [39]. Typically, γ'' forms as plate-like particles. While the γ'' phase is primarily composed of Nb, Fe is required to stabilize its formation. Due to its metastable behavior, γ'' will transform to δ with an orthorhombic $D0_a$ structure above $\sim$ 885 °C [39]. Large fractions of δ can be detrimental to mechanical properties, although its presence as dispersed small particles at low fractions is often desirable for grain size control [48]. The γ'' to δ phase transformation limits high temperature applications of γ'' forming alloys. The most well-known example of a primarily γ'' strengthened alloy is IN718. Partly due to its comparably lower cost and higher workability, IN718 has found use in many applications including gas turbines, turbocharger rotors, nuclear reactors, liquid fueled rockets, and in other corrosive and structural applications [47].

Depending on the detailed composition, carbides such as MC, M_6C, M_7C_3, and $M_{23}C_6$ may form, which may help to strengthen Ni-based superalloys further through exerting grain boundary pinning if present in suitable quantity and dispersion. Multiple morphologies have been reported for carbides in Ni-based superalloys ranging from spherical, cuboidal, to "script"-like. Their size will largely depend on the solidification conditions and heat treatment. Other secondary precipitates such as nitrides, oxides, and borides have also been known to form dependent on the amount of N, O, and B in the given alloy. Topology closed-packed (TCP) phases are less desirable and often occur due to the high number of elements found in Ni-based superalloys. These include R, P, μ, Laves, and σ. These phases often form due to excessive amounts of Mo, Cr, W, and Re. They often appear in needle-like morphologies and are known to lower rupture strength and ductility. High degrees of solute segregation can increase the probability of forming such phases [39, 48].

Review of solidification and solid-state phase transformations and context in AM

Due to the complex solidification routes common within PBF processes, a review of solidification is important for understanding the various microstructures that can potentially form during printing. It has been noted for IN718 under AM processing that the formation and morphology of the Laves and δ phases is often controlled by the solidification conditions and related solid-state phase transformations [50, 51]. For example, the formation of the Laves phase is usually the result of Nb segregation to the grain boundaries during solidification due to non-equilibrium solidification conditions [50]. For δ, various morphologies can form, particularly in E-PBF. Further, it has been shown that the location as a function of build height and related differences in thermal profiles may result in bottom regions of a build having an aged microstructure while the top of the build often remains unaged [51].

During solidification, the partitioning of elements occurs due to differences in equilibrium composition between the solid and the liquid phases. As outlined by Aziz [52], if the solid–liquid interface is moving fast enough, non-equilibrium solidification conditions may occur where the solute diffusing away from the interface can become trapped in the solid. This is known as solute trapping [53]. Typical cooling rates in PBF do not lead to a complete solute trapping (i.e., planar growth); however, they lead to a non-equilibrium solidification of elements where certain solutes can be found partitioned into the matrix [54, 55]. For instance, it has been shown via lattice constant measurements using X-ray diffraction (XRD) of IN625 processed through L-PBF, that high amounts of strengthening elements such as Nb and Mo are embedded into the matrix instead of segregating to grain and cellular boundaries. This is due to the occurrence of trapping of some of the solute due

to high cooling rates [56, 57]. Likewise, Laves has been shown to be influenced by the rate of solidification. Faster solidification rates reduce Laves formation due to trapping of Nb in the matrix phase [54].

Solid–solid phase transformations within Ni-based superalloys are predominantly diffusional processes. The diffusion of elements and the nucleation and growth of new phases are time- and temperature-dependent processes [58]. δ, γ', and γ'' form in the solid state and, therefore, are influenced not only by the length scale of elemental partitioning after solidification but also by the thermal history experienced within the part [59, 60]. Therefore, process parameters and scan strategy can play a large role in influencing their phase fractions and morphologies. For example, during E-PBF printing of IN718, the diffusion of Nb out of the γ'' and into the δ phase located at the grain boundaries has been reported [51]. The formation of the δ phase occurs due to the elevated preheat temperatures between 900 and 1000 °C that causes the dissolution of the γ'' phase, and depletion of γ'' from Nb around the newly formed δ [51].

During the L-PBF process, however, there is often a lack of δ, γ', and γ'' formation due to the very high cooling rates prohibiting these diffusional processes from occurring as temperatures decrease too quickly [61]. Manipulation of the thermal history through changes in the processing parameters and scan strategy to either reduce or increase the cooling rate can change the formation and morphology of such phases. The link between phase nucleation, growth, and morphology is discussed in more details for each of these individual phases in "γ' phase", "γ'' and δ phase", and "Other secondary precipitates and TCP phases" sections.

γ matrix phase

For PBF processes, the microstructural evolution during solidification most often involves the epitaxial growth of columnar grains in the <100> direction aligned with the build direction, however, processing parameters and geometry can play a large role in influencing the resulting microstructure. Studies by Thijs et al. [62, 63] on L-PBF first showed how variations in the scan strategy can result in changes in the direction of elongated grains away from the typical <100> direction. These changes in grain structure were attributed to differences in the local heat transfer conditions. Further, Carter et al. [64] showed that a more complex island scan strategy could form a bimodal microstructure of both fine grained regions less aligned to the build direction, and elongated grains with very strong alignment to the build direction due to variations in solidification conditions. Many studies have since looked at the impact of scan strategy on thermal conditions [65–67], phases [68], cracking [69] and grain structure [70–75]. Numerous studies have also expanded on the processing parameters' (i.e., laser power, speed, hatch spacing, beam diameter, etc.) impact on the microstructure and outlined how changing thermal conditions can affect resulting grain size and orientation [76–82]. Due to the higher degree of beam control within E-PBF, the formation of either equiaxed or columnar grains is possible at specific locations [73, 83–85]. Control over equiaxed and columnar grain formation in L-PBF is possible, however it is greatly limited compared to E-PBF. This is due to mechanical limitations in the movements of the mirrors making similar high-speed movements of the laser impossible [86]. Further considerations on the build layout, part orientation, and the impact of build height on the microstructure and properties have also been extensively studied [87–94].

An example of the impact of solidification conditions on Ni-based superalloys from work by Gokcekaya et al. [82] is shown in Fig. 3a, b and c where preferential crystallographic orientations were tailored in L-PBF of IN718 by changing the laser speed and power. Figure 3a shows a region of crystallographic lamellar structure with <110> main layers and <100> sub-layers aligned with the build direction (BD) formed using a laser speed of 1 m/s and laser power of 360 W. Figure 3b shows microstructures with a <110> fiber texture along the BD that is single-crystal-like produced with a faster 1.4 m/s laser speed and 360 W laser power. Materials with polycrystalline-like microstructures, as shown in Fig. 3c, were also manufactured and had tensile strength superior to cast IN718. This microstructure was produced using a lower 180 W laser power and 1.4 m/s laser speed. In brief, the differences in grain structure can be attributed to differences in the evolution of melt pool boundaries due to the different scanning parameters (Fig. 3a, b, c). An examination of a dendritic structure, which makes up individual grains and associated melt pool from a different

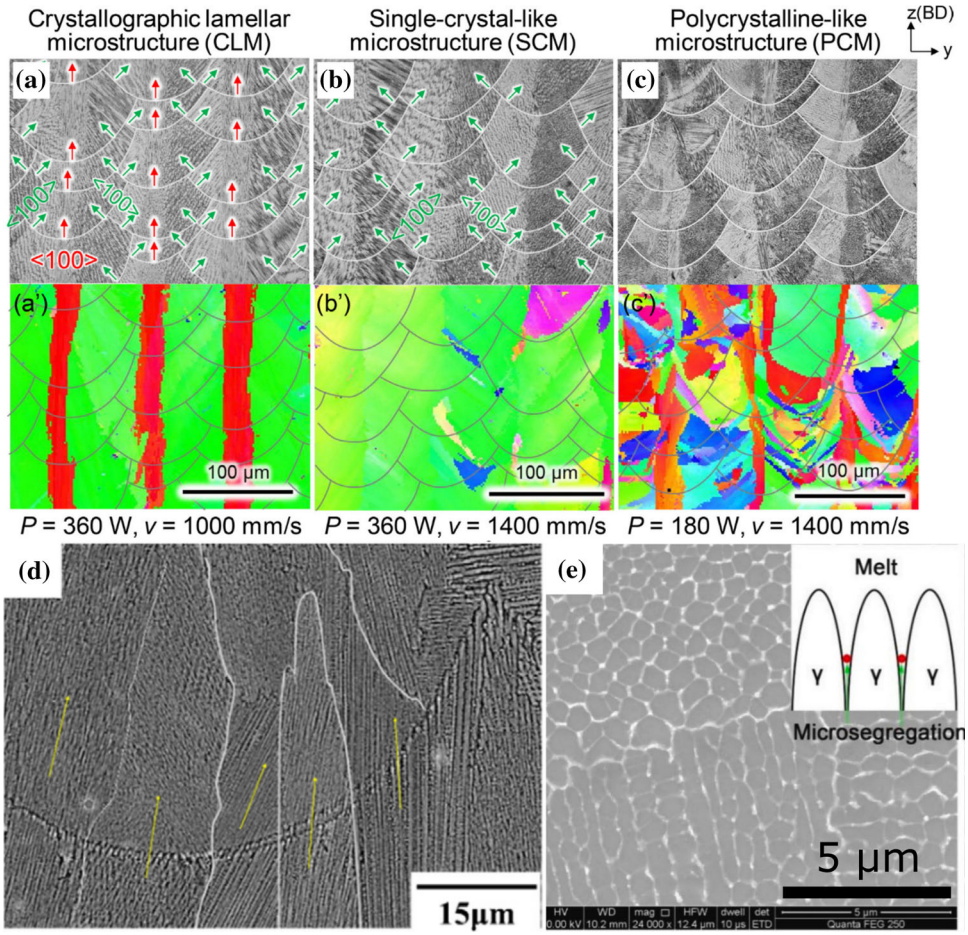

Figure 3 **a**, **b**, **c** The impact of solidification conditions on the microstructure in L-PBF IN718 as a function of laser power and speed with a′–c′ the inverse pole figure of the same areas. **d** Epitaxial growth of dendrites across the melt pool for L-PBF IN718. **e** Cellular dendritic structure of γ in L-PBF GH648 showing microsegregation. **a**, **b**, **c** are reproduced from [82], **d** from [96], and e was adapted from [97] with permission.

work is shown in Fig. 3d. It can be concluded that during the solidification of the subsequent melt pool, the previous dendritic structures will continue to grow. Since dendrites grow fastest in line with the direction of the thermal gradient (schematics given in Fig. 3a, b), the preferred growth of dendrites will change depending on the melt pool solidification conditions [95].

Within L-PBF produced Ni-based superalloys, each γ grain interior exhibits a cellular dendritic structure (Fig. 3e). Based on the literature, the noted range of primary dendritic arm spacings (PDAS) is between 0.2 and 1.8 μm [98, 99]. Most studies report no secondary dendrite arms due to the fast solidification rates. Overall, the dendritic structures in L-PBF have been reported to be around two orders of magnitude finer than in traditionally cast Ni-based superalloys [57]. Within the dendritic and interdendritic structures a substructure exists that has been reported as cellular networks of dislocations (Fig. 4a, b) [100]. The formation of these substructures is due to thermal stresses resulting in yielding and distortion of the material that is constrained by surrounding material around the melt pool. This leads to a large build up in residual stresses [101]. Figure 4 shows examples of different cellular networks that can occur within Ni-based superalloys [102, 103]. Due to the complex solidification conditions within L-PBF, it is difficult to point to a single contributing factor to the differences in dislocation networks where geometry, scan strategy, process parameter, and alloy composition may play a role.

In general, due to elemental segregation, the γ phase is primarily enriched in Cr, and Fe [104, 105]. However, due to the high solidification rates, a certain amount of solute trapping may be found. For instance, it has been reported for IN718 that in systems using a pulsed laser instead of a continuous laser, a higher content of Nb can be found in the γ phase due to increased cooling rates resulting in increased solute trapping [54].

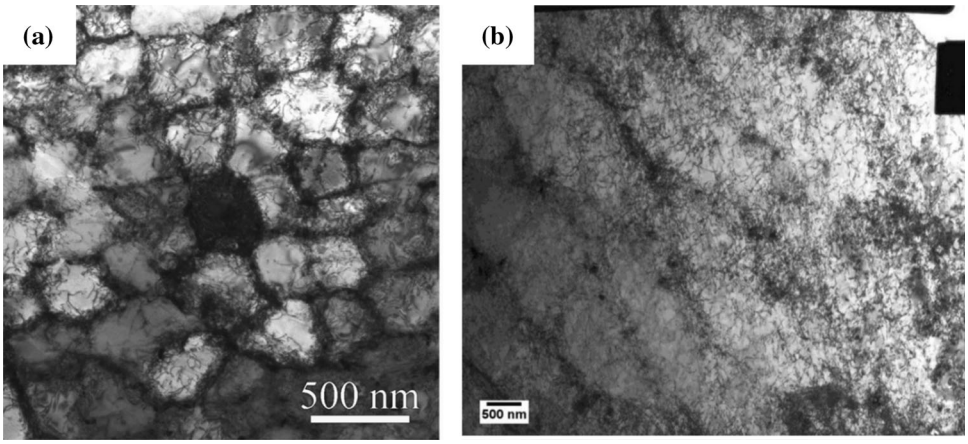

Figure 4 Conventional bright-field transmission electron microscopy (BF-TEM) micrographs of L-PBF **a** IN718 and **b** Nimonic 263 samples showing the formation of sub-grain cellular dislocation structures. **a** is reproduced from [102] and **b** from [103] with permission.

Generally, the overall structure of γ in E-PBF is more complex due to the intrinsic heat treatment that often occurs as a result of the high preheat temperature. Therefore, the characteristics of γ is location dependent along the build height. The dendritic structure is specifically outlined in Fig. 5a, b, and c and can be divided into three distinct regions. At the top of the build, a well-defined dendritic structure exists (Fig. 5a) [106, 107]. Due to the slower cooling rate compared to L-PBF, secondary arms might form dependent on solidification conditions. The primary dendrites are noticeably coarser compared to L-PBF

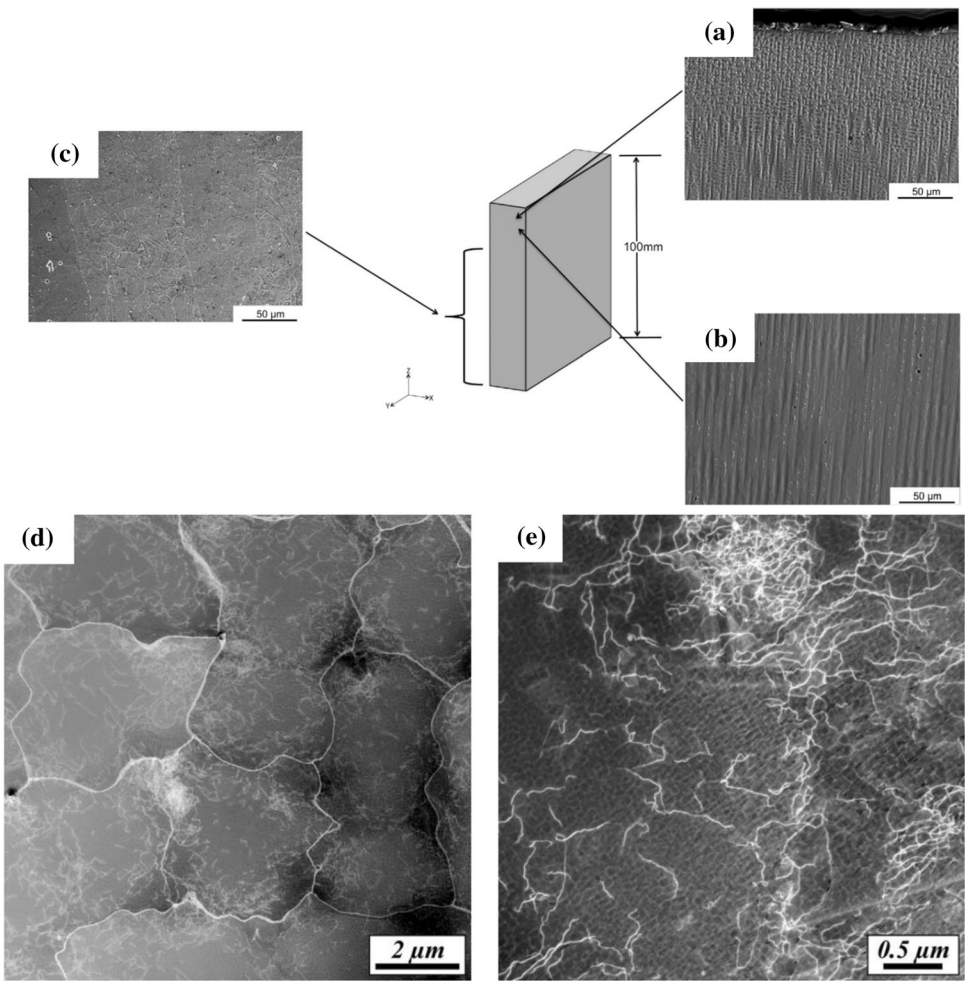

Figure 5 **a**, **b**, **c** Schematic showing the spatial variation in microstructure for E-PBF IN718 with **a** showing a dendritic structure at the top of the build, **b** showing a more diffuse dendritic structure 2 mm from top of build, and **c** representative of the bulk microstructure starting from 5 mm from top of build [107]. **d**, **e** Scanning transmission electron microscopy–High-angle angular dark field (STEM-HAADF) image of the dislocation structure for E-PBF CMSX-4 showing **d** complex sub-grain dislocation boundaries and ingrown dislocation nests, and **e** higher magnification of an interdendritic region with an ingrown dislocation nest. **a**, **b**, and **c** adapted from [107] and **d** and **e** from [108] with permission.

with studies reporting PDAS between 2.1 and 30 μm [108, 109]. Further down the build height, the dendrites start to homogenize due to the diffusion of elements occurring from the elevated build temperatures as illustrated in Fig. 5b. At a certain height which is process dependent, a steady state is reached, and a dendritic structure may no longer be present as shown in Fig. 5c. Compared to L-PBF, E-PBF does not always form an organized cellular sub-grain structure within the bulk of the sample. Instead, dislocations are reported to build up at regions that hinder dislocation slip activity (i.e., around precipitates and grain boundaries) for example in interdendritic regions as shown in Fig. 5d. Figure 5e shows the occurrence of a dislocation nest at the interdendritic region toward the top of the image, as an example of some of the complex dislocation structures that may form in E-PBF. Overall, the dislocation density in E-PBF has been reported to be lower compared to L-PBF. This is largely due to the preheating step which lowers thermal gradients and therefore the resulting residual stress [110].

γ' phase

The Ni–Al system can be considered as the basis for the binary system for most Ni-based superalloy compositions. While the matrix phase for this system is a Ni-rich γ phase, an increase in the fraction of Al results in precipitation of γ'. These precipitates impede dislocation slip at high temperatures mainly through the formation of anti-phase boundaries [111]. γ' therefore imparts advanced high temperature creep and strength properties in Ni-based superalloys. A high-volume fraction of γ' can, however, make alloys non-weldable due to challenges such as solidification cracking, strain-age cracking, and hot tearing. γ' may accumulate at the grain boundaries, and in turn develop high gradients of residual stress therein. This will make the part highly susceptible to cracking. Due to this, AM of Ni-based superalloys with a high volume of γ' remains challenging [28].

From conventional processing, it is known that the chemistry, length, and distribution of γ' particles are dependent on the temperature at which they form and grow [112]. Therefore, the rate at which the alloy is cooled below the solvus temperature plays a substantial role in the characteristics of γ'. Generally, an accelerated cooling rate ($> \sim 40$ K/min) results in a unimodal distribution of γ' with a length or diameter of around 300 to 500 nm. Cooling at a slower rate has been reported to result in a multimodal size distribution of large (> 50 nm) and small (< 50 nm) γ' particles [113]. Different alloying elements show a different behavior with regards to partitioning into γ versus γ'. Usually, Mo, Re, Cr, and Co partition into the γ matrix, while Ti, Al, and Ta partition into γ'. Some particular elements like Ru and W are soluble in both γ and γ' [114]. The partitioning behavior of elements within γ and γ' plays a significant role in the properties of the material. As γ' is coherent with γ, the main factor affecting the lattice parameter difference (i.e., misfit) between these phases is related to their chemistry variation. This misfit defines the morphology of γ' as well as the elastic and plastic stresses at the γ-γ' interphase boundaries, which in turn influence the mechanical properties of the material [115].

Alloys with high content of γ' such as CMSX-4, Rene N5, and MarM247 are rarely processed by L-PBF. This is due to the potential challenges well-known in the field of AM based on the prior knowledge on crack and defects formation during welding of these alloys [15]. L-PBF of high γ' Ni-based superalloys is challenging due to their chemistry. Presence of significant amounts of Al and Ti adversely affects the processability and stimulates liquation and hot crack formation. In the following, the limited studies existing on L-PBF of these alloys are summarized.

In a CM247LC processed by L-PBF, Divya et al. [116] demonstrated that very fine γ' particles form during printing. They observed two types of γ' precipitates, intracellular ones of ~ 5 nm and intercellular ones of ~ 50 nm. Otto et al. [117] have shown that γ' of ~ 20–30 nm can be observed in L-PBF processed Haynes 282. These authors have, however, pointed out that heating the build plate at 300 °C during L-PBF was a critical factor for mitigating cracks. The lack of significant precipitation of γ' and carbides observed at the grain boundaries limits the amount of buildup of residual stresses therein minimizing cracking.

The prior results on CM247LC are of primary interest as with increased build heating a decrease in thermal gradients is expected, resulting in a lower likelihood for the suppression of γ' due to high cooling rates. Therefore, results where precipitation mechanisms of γ' change based on changes to thermal

gradients need more study. Further, the fact that the high cooling rate associated with L-PBF usually bypasses γ' formation means further heat treatments are required for γ' to be precipitated. Studies on L-PBF of Haynes 282, for example, report no γ' precipitation during the build process [41]. This has been attributed to two factors; the exceptionally high cooling rate associated with L-PBF and the sluggish γ' formation kinetics in this alloy. Rene 41 processed by L-PBF also showed no signs of γ' formation during the printing process [42]. In a similar fashion, no γ' was detected in the microstructure of IN738 alloy processed by L-PBF [43]. Finally, after L-PBF processing of a Ni-8Cr-5.5Al-1Ti model alloy, STEM HAADF confirms that high cooling rates associated with L-PBF generally suppresses γ' formation [44].

The in situ precipitation of γ' during E-PBF printing has been more widely observed in several Ni-based superalloys. For example, CM247LC superalloys processed by E-PBF show a gradient in the microstructure, including in the characteristics of γ' [118]. As E-PBF of alloys with substantial γ' volumes are carried out at high preheat temperatures (usually close to the solvus temperature), the area adjacent to the substrate base-plate experiences prolonged aging at elevated temperatures following initial solidification. Areas at the top of the built are exposed to much shorter aging prior to the final cooling. This is the main reason behind the gradient in the decomposition of $\gamma \rightarrow \gamma + \gamma'$, and in turn variation of the γ' size across the build height [119].

Haynes 282 has been successfully processed via E-PBF. This alloy is a relatively new γ'-strengthened Ni-based superalloy with outstanding high-temperature and weldability properties which has great potential to be used in industrial and turbine engines. This alloy has been designed in such a way that it forms only up to 19 vol.% γ' to obtain a good balance of strength and processability [120]. After E-PBF processing of Haynes 282, producing samples of $15 \times 15 \times 120$ mm^3 rods and $15 \times 100 \times 120$ mm^3 plates, a relatively uniform distribution of γ' was observed throughout the microstructure and no depletion at the grain boundaries was seen [120]. A detailed analysis of the size and morphology of γ' along the build direction shows that there was a minor change in the morphology of γ' across the height (Fig. 6). Close to the top of the build, γ' displays more sphericity and has a size (for which size here refers to the length along a given side) of

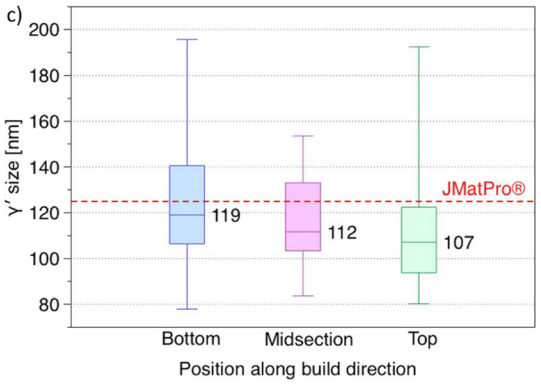

Figure 6 Size distribution of γ throughout an E-PBF processed Haynes 282 build overlaid on the JMatPro simulations of average γ' size of $\sim$ 125 nm. Reproduced from [120] with permission.

$\sim$ 107 nm. At the bottom of the build, the morphology changes to a more cuboidal morphology with an increase in the size to $\sim$ 119 nm. The larger size and more cuboidal morphology at the bottom of the build is the result of the material in this region being exposed to high temperatures for a longer time. It is common for γ' to coarsen and change its morphology from spherical to cuboidal during extended thermal exposure [121]. The size of the γ' measured by back-scatter scanning electron microscopy (SEM) is in line with calculations from JMatPro, shown by the red dashed line in Fig. 6, that was carried out using the approximate thermal history of the material during E-PBF reported in [120] as input.

Another γ' forming Ni-based superalloy successfully processed by E-PBF is Rene-N5 [106]. This study reports on a less common triangular prism geometry with length and width of 30 mm which is compared to square geometries to unveil the impact of geometry on the microstructure. Solidification of Rene-N5 starts with the formation of γ dendrites, which later decompose to γ and γ' through a solid–solid phase transformation during cooling. Hence, γ' particles are not expected to be distributed evenly across the build. Assuming a Gulliver–Scheil solidification for E-PBF, with no back-diffusion within the solid phase, there will be strong microsegregation during solidification, with both Al and Ti (which have partition coefficients of < 1) segregating into the interdendritic regions. This results in the formation of γ' in the interdendritic regions rather than the dendrite cores during the build process. The interdendritic γ' coarsens going from top to bottom of the build which is related to the increase in time the material was held

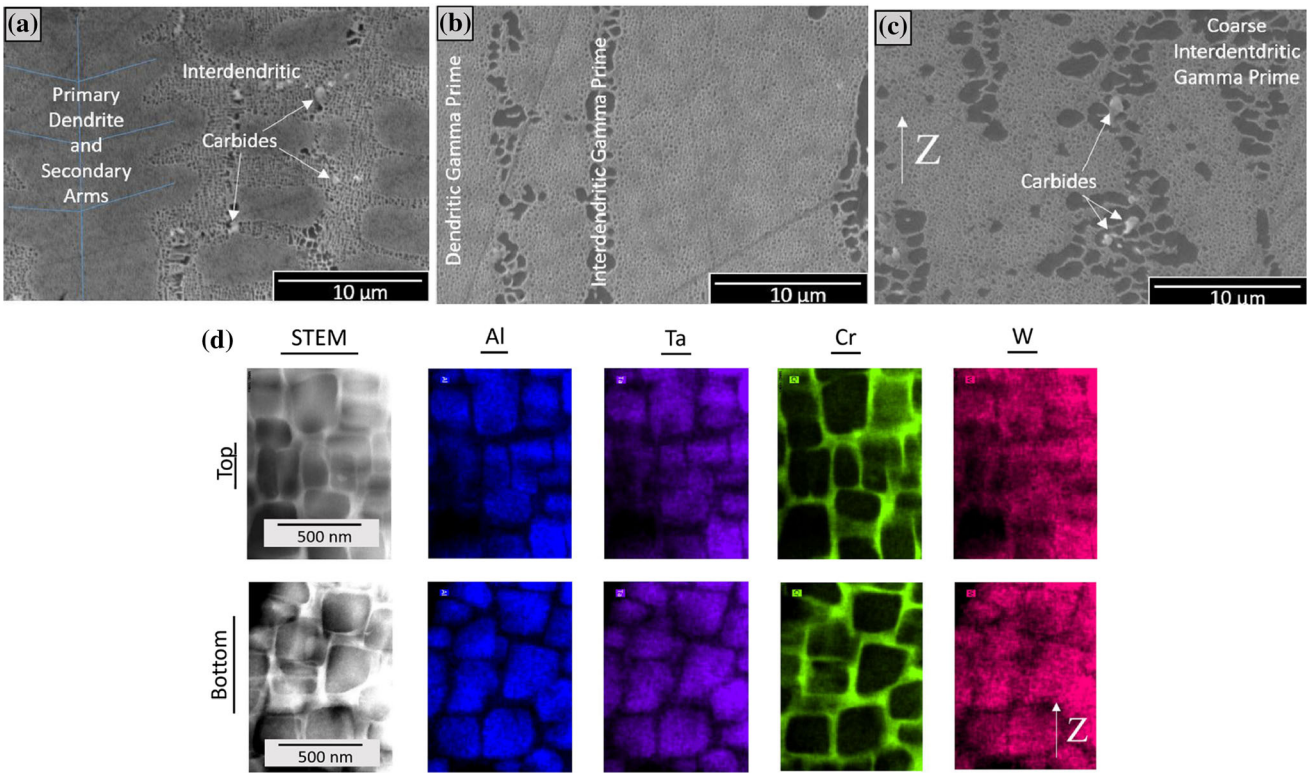

Figure 7 SEM images of the E-PBF processed Rene-N5, showing the microstructure evolution across the build. **a**, **b**, **c** refer to last solidified layer, middle of the build and region just above the substrate, respectively. **d** Dendritic regions of Rene-N5 processed by E-PBF showing segregation of Al, W, and Ta to the cuboidal γ' particles. Adapted from [106] with permission.

at the preheat temperature (Fig. 7a, b, and c). Once printing is completed and the build cools, the remaining γ' will precipitate from the dendritic cores. This results in two distinct populations of γ' throughout the build (Fig. 7) with the interdendritic γ' size reported to range from around 0.5–2 µm from top to bottom of the build, and the γ' in the dendritic cores averaging 230 nm exhibiting a consistent cuboidal morphology.

In another study on CMSX-4 processed by E-PBF [122], a regular γ-γ' morphology is observed and γ' particles are cuboidal (Fig. 8). Again, a γ' size gradient is reported with precipitates having a $\sim$ 100 nm size at 0.5 mm below the top of the build, and $\sim$ 380 nm at 15 mm from the top. The volume fraction of γ' is relatively consistent across the build. Similarly, in this study, the same coarsened interdendritic and smaller dendritic γ' structures can be seen as in the Rene N5 study. Likewise, this microstructure can be associated with the initial formation of γ' in the interdendritic regions followed by coarsening during printing. During cooling, the γ' will nucleate and grow in the dendritic core.

In an unspecified non-weldable Ni-based superalloy (Ti + Al = 8.6 wt%) with substantial amounts of Cr, Co and Mo, a significant variation in the size of γ' across the build height after E-PBF processing has been reported [123]. In general, one can see a decrease in the size of γ' from the bottom to the top of the build (Fig. 9). For instance, γ' at the top is $\sim$ 100 nm in size while it is around 600 nm at just 5 mm above the substrate. Similarly, a CMSX-4 alloy processed by E-PBF showed heterogeneity with regards to γ' particles at different locations [124]. The size of γ' precipitates in the dendrite core is $\sim$ 250 nm while the size of γ' precipitates in the interdendritic region is almost twice as large. The partitioning of alloying elements between the γ' and the matrix is similar to the behavior observed in cast material [124]. Rene 142 has also been successfully processed via E-PBF with a high volume fraction of γ' in the as-built state [125]. In Rene 142, a similar bimodal distribution of γ' was noted with the average size of γ' being about 275 nm and a total volume content of $\sim$ 60%.

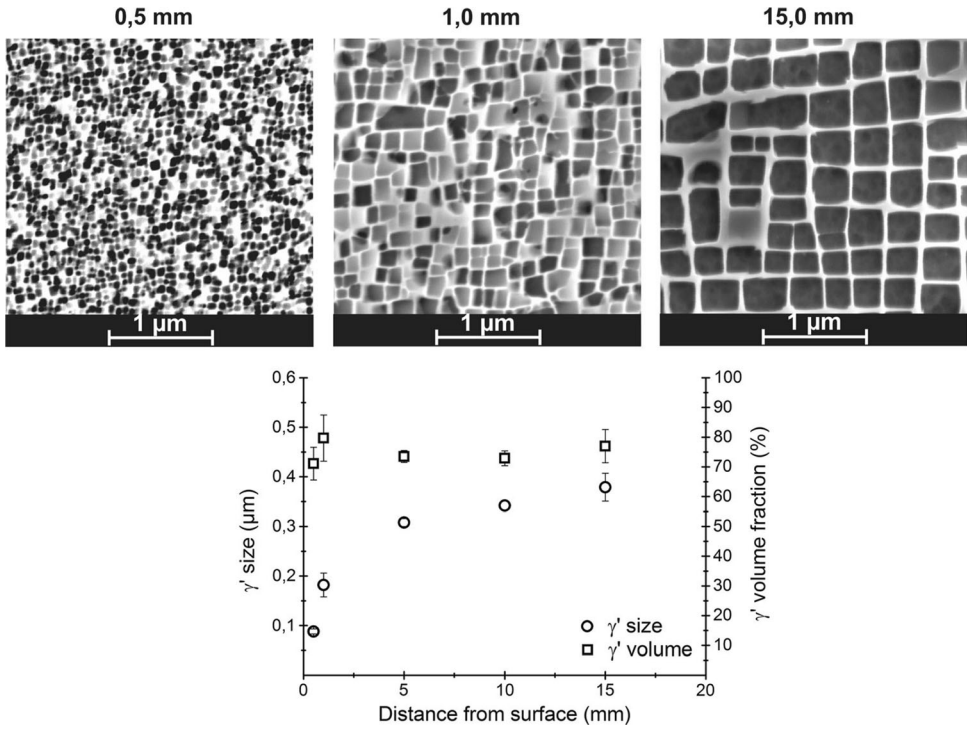

Figure 8 SEM images of the CMSX-4 alloy processed by E-PBF showing the evolution of γ' size with build height. The graph below summarizes the evolution of size and morphology of γ' throughout the build height. Reproduced from [122] with permission.

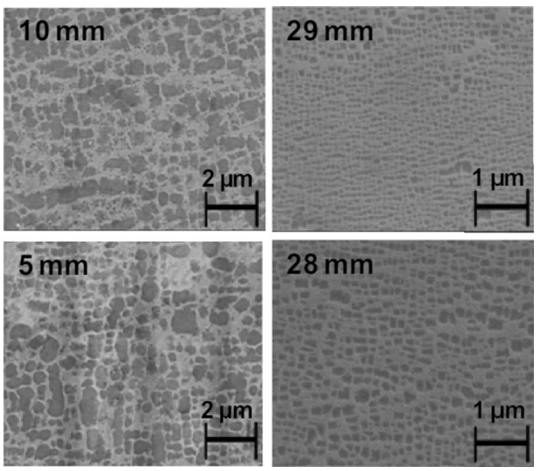

Figure 9 SEM images showing the size of γ' along the build height in a non-weldable Ni-based superalloy (Ti + Al = 8.6 wt%) processed by E-PBF (inset numbers show the distance from the substrate). Adapted from [123] with permission.

Based on further work from Frederick [126] using a custom Ni–Cr–Al alloy, it is possible to limit the height-dependent γ' size variation due to coarsening from the in situ heat treatment. The consistent γ' distribution in this study resulted from processing of the alloy with a preheat above the γ' solvus. It is only during cooling after the build is complete that γ' nucleates and grows through a solid-state transformation while the build temperature decreases and enters the γ' precipitation window. It is to be noted that one downside with processing above the γ' solvus is sintering of the powder surrounding the part, leading to difficulties in extracting the part from the process [126].

In a study by some of the current authors [127], traditionally non-weldable IN738 was processed successfully under E-PBF without cracks and showed extensive formation of γ' in the as-built condition. Successful processing was accomplished due to controlled heat input and reduced deposition cooling rate (temperature gradient) as well as a high preheat temperature of ~ 1000 °C. These factors significantly reduce the thermal stresses during printing and provide enough time and activation energy for γ' particles to precipitate from the supersaturated matrix. In the middle region of the build, where this study focused on, γ' particles have a bimodal size distribution with primary γ' of 400–600 nm and secondary γ' of 5–50 nm (Fig. 10). The authors related this bimodality to the transformation path of γ' particles, including primary eutectic γ' precipitation in the interdendritic regions during solidification, dissolution of a fraction of these precipitates due to the high preheat temperature (1000 °C), and precipitation of smaller γ' particles at lower temperatures upon final cooling to room temperature. A slight

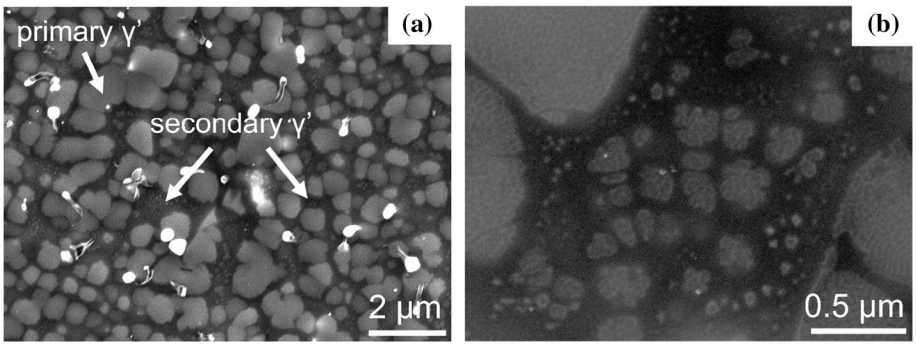

Figure 10 SEM images of middle region of E-PBF processed IN738 at **a** low and **b** high magnifications revealing bimodal size distribution of γ' particles. Reproduced from [127] with permission.

difference in the chemical composition of primary and secondary γ' particles was observed which was attributed to the fact that they had been formed at different temperatures and within matrices that had different chemical compositions during different stages of solidification and cooling.

Similar to other studies, coarser γ' particles in this study exhibit a cuboidal morphology while the finer ones are predominantly spherical. As mentioned above, the γ' morphology is a function of misfit between γ' and matrix γ as well as the diffusion field and chemistry of the surrounding matrix. As reported by Hagel and Beattie [128], γ' takes a spherical, cubic, and plate-like morphology when the lattice mismatch of γ-γ' is 0–0.2%, 0.5–1.0% and above 1.25%, respectively. In more detail, the strain energy induced growth along the {100} planes change the morphology from spherical to cubic once it exceeds a certain amount. Lattice misfit may also create anisotropic strain energy resulting in the formation of protrusions [121]. This explains the spherical morphology of fine γ' particles and the gradual change to a cubic morphology for the grown γ' particles in the studied microstructure.

Further in-depth analysis of the same E-PBF processed IN738 by some of the current authors [119] through the use of atom probe microscopy (APM) reveals extensive precipitation of γ' throughout the entire build (Fig. 11). At the top of the build, only cuboidal primary γ' particles are detected. In the middle and bottom of the build, however, there are two different populations of γ' particles: primary cuboidal ones, as seen at the top, and secondary γ' particles of spherical shape with sizes of < 50 nm (Fig. 11). There is a $\sim$ 35% reduction in the size of primary γ' from bottom to the top of the build. Only slight differences in chemistry are observed between the primary and secondary γ' particles throughout

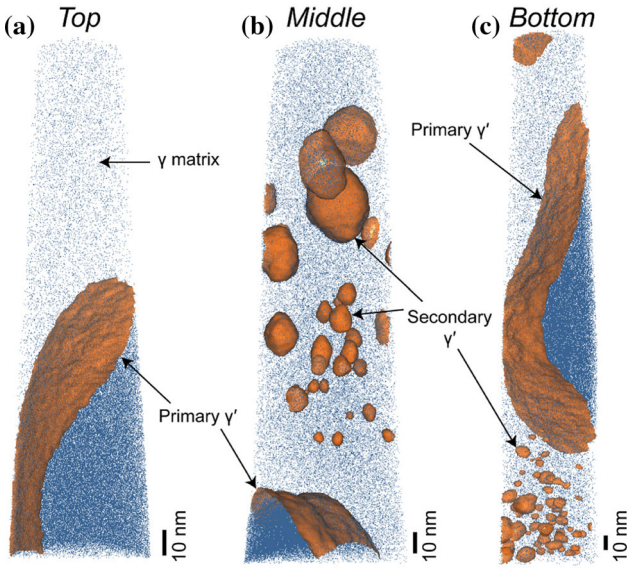

Figure 11 Atom maps of different regions of E-PBF processed INC 738 with 10% (Al + Ti) iso-concentration surfaces. Reproduced from [119] with permission.

the build. APM also shows that the combined content of Al + Ti is only 19 at.% which deviates from the ideal $Ni_3(Al,Ti)$ stoichiometry. This implies that Al sublattices can be substituted by other solutes such as Cr and Ta [129, 130].

Finally, in a single crystal (SX) Ni-based superalloy with the composition of Ni–5.5Al–7.4Ta–4.4 W–7.1Co–7.5Cr–1.2Ti–2.0Mo (wt%) processed by E-PBF, different populations of γ' precipitates were observed. Nanoscale γ' ($\sim$ 20 nm) was observed in the as-built state in particular in the bottom few layers [131]. Larger (primary) γ' precipitates of $\sim$ 100 nm with a spherical morphology were also identified throughout the γ matrix. Based on the selected area electron diffraction (SAED) patterns, the authors suggested that γ' precipitates may form via a spinodal decomposition mechanism. An interesting observation in this work is the smaller size of γ'

precipitates at the bottom of the build within a columnar to equiaxed transition region. This is in contrast to other studies where coarser γ' particles were observed at the bottom of the build. This is likely due to changes in the solidification conditions as is evident by the change in grain structure.

Although rarely, γ' precipitation has been reported in the as-built microstructure of IN718 in some studies. Yang et al. [132] have shown that by controlling the in situ aging behavior of IN718 alloy through manipulating the types and durations of the thermal cycles during L-PBF, sequential precipitation of γ' and the composite morphology of primary-secondary γ' covered by a γ'' shell can be achieved. Zhao et al. [133] also reported the formation of γ' in IN718 during L-PBF based on XRD of the as-built samples. This result may, however, be questioned considering the overlap of XRD peaks for γ, γ', and γ'' [134]. Further, based on other works, even if γ' and γ'' were formed, they may have been below the detection limits of XRD and other techniques used.

From the literature covered above, the question on the impact of changing processing parameters on γ' size and morphology has only been explored in detail by one study based on the currently available literature. Peng et al. [135] showed that there was no difference in γ' size for both the dendritic core and interdendritic regions when changing the energy input. It should be noted, however, that the change in energy input between the two samples was small, leading to the hypothesis that a larger difference in processing parameters might lead to appreciable changes. Most other studies explore only one single processing parameter set with only a subsection of processing parameters reported, making it difficult to interpret how changing processing conditions may impact γ' during the PBF process. Further difficulties are added when considering the impact of changing composition on the γ' kinetics. Therefore, we look at more fundamental aspects of γ' precipitation here instead to make an assessment on the impact of processing parameters on the γ' evolution.

Many high γ' alloys printed using PBF show a bimodal γ' distribution [106, 116, 127, 131, 135]. Based on solidification theory, as the melt pool solidifies, elements partition either to the dendritic core or interdendritic regions [53]. As the partition coefficients of the elements commonly associated with γ' formation (e.g., Al, Ti, and Ta) have a value lower than unity, these elements prefer to partition to the interdendritic regions [106, 136]. The length scale of this partitioning and the amount of solutes that partition is directly related to the cooling rate. As the cooling rate increases, the length scale between the dendritic core and interdendritic region decreases. At high enough cooling rates solute trapping may occur resulting in a decrease in solute partitioning [95]. After solidification, once the temperature falls below the γ' solvus, γ' begins to nucleate. The driving force for nucleation is the degrees of undercooling and supersaturation. Therefore, γ' will nucleate first in the supersaturated interdendritic region due to solute partitioning. Further increasing of the cooling rates result in greater undercooling, therefore, higher cooling rates lead to a greater number of γ' particles nucleating while reducing their growth time. The larger number of particles is also correlated with a decrease in γ' size. Depending on thermal conditions, the γ' contained in the dendritic core region will see a delayed nucleation due to reduced driving force that comes from the elemental partitioning as discussed previously. The γ' in the dendritic core region will, therefore, precipitate and grow at slower rates resulting in a bimodal size distribution between the dendritic core and interdendritic regions [137]. Outside of AM context, directional solidification experiments show these correlations; e.g., increasing cooling rates result in a decrease in PDAS and a decrease in γ' size [136–138].

With respect to E-PBF, the phase formation can be complex due to the preheating process, large variations in process parameters and possible changes in geometry. As mentioned previously, currently no straightforward conclusion can be drawn from the existing literature on the exact impact of process parameters on γ' other than size and morphology are expected to be impacted. For instance, the reported variation in PDAS for γ' alloys is between 2.1 μm and 15 μm [108, 139]. While changes in the PDAS have been correlated to processing conditions in E-PBF [140], it has not been experimentally verified how much a change in PDAS might impact γ' size, morphology, and distribution due to changes in the spacing between dendritic core and interdendritic regions along with changes in elemental partitioning. Further, it is difficult to make assessments from other processes. For instance, under directional solidification at higher solidification rates, the difference in γ' size and PDAS diminishes for different cooling rates [137], however, these experiments do not take into

consideration the thermal fluctuations that are common in the PBF process.

Finally, the impact of the preheat temperature on γ' needs to be considered. Based on the previous covered literature, the impact of the preheat temperature is better understood. At temperatures above γ' solvus, γ' will not nucleate until after the build process is completed and the build begins to cool. Depending on the alloy composition, the same bimodal γ' will form due to differences in the kinetics in the dendritic core and interdendritic regions. As γ' precipitates form during cooling, their size is homogeneous across the build height. The downside of processing at such high temperatures is heavily sintered powder surrounding the part [126]. At temperatures below the γ' solvus, γ' is likely to form at the interdendritic regions due to the high amount of solute. The dendritic core is not likely to nucleate due to the sluggish γ' kinetics in a region depleted in Al, Ti, and Ta. Due to the high preheat temperature, some dissolution of primary particles is expected. The formation of smaller particles in the dendritic core then occurs during the cooling period where the temperature drops low enough such that small spherical γ' can form [127]. Reports often show cuboidal γ' in the interdendritic region that varies based on build height due to in situ aging and spherical γ' in the dendritic core region that can be consistent in size across the build [106]. It should be noted, however, that the above morphology description applies most often to high γ' alloys. For alloys with lower γ' fractions such as Haynes 282, spherical morphologies have been cited to form across the build instead [120].

For L-PBF processes, cooling often occurs fast enough and γ' kinetics is sluggish enough that γ' nucleation is avoided, however, a few factors may allow it to form. First, depending on the alloy composition, γ' kinetics may be fast enough to permit its formation despite the high cooling rate. Second, if processing parameters result in slower cooling rates and/or greater number of thermal fluctuations, then γ' formation may be possible. Lastly, a sufficiently high build plate temperature has been shown to permit γ' formation during L-PBF due to the decrease in cooling rate [117]. Discussion on process parameters and their impact on the γ' size and morphology in L-PBF have been less frequently reported due to the difficulty in obtaining this phase in the first place. This section is concluded up by a summary of γ' sizes reported for Ni-based superalloys processed by PBF in Table 2.

γ'' and δ phase

Ni-based superalloys containing Nb and Fe can form the meta-stable γ'' phase [112]. This phase becomes a main contributor to strength via formation of coherency strained areas at the interphase region with the γ matrix due to its lattice misfit [141]. Most γ'' containing alloys also have additions of the γ' forming elements, Al and Ti. In conventionally manufactured Ni-based superalloys, co-precipitate (stacked γ'-γ'' duplets, triplets and more complex morphologies) formations have been widely reported by various groups including by some of the current authors, where their morphology and configuration are linked to the (Al + Ti) to Nb ratio [142] and thermo-mechanical processing routes [143, 144]. In PBF materials, similar phenomena correlated to the aforementioned mechanisms of γ'' strengthening and coarsening [145], and γ'-γ'' co-precipitation have also been reported in heat-treated materials [37, 102, 146].

IN718, as the most popular γ'' strengthened alloy processed by AM, has good weldability properties due to the sluggish formation of precipitates, and low susceptibility to cracking. In recent years, it has been subjected to several studies aimed at understanding its mechanical properties as a function of microstructural features introduced by varying parameters during PBF processing [55, 147–149]. In conventionally manufactured IN718, the high strength is a result of a combination of strengthening factors including grain size, solid solution, residual stress, and precipitation [150, 151]. Zhang et al. [145] recently demonstrated the influence of these strengthening effects in L-PBF IN718, where precipitation is reported to be the largest contributor to strength. Additionally, the presence of TCP phases, and the dendritic solidification structure are important aspects to consider in the evaluation of AM parts mechanical properties [149, 152].

In conventionally manufactured materials, the formation of precipitates prior to ageing in γ'' forming alloys occurs during slow cooling from forging or solution annealing. Continuous cooling transformation (CCT) diagrams describe that for IN718, cooling rates below 20 °C/min from temperatures between 1100 and 1000 °C passing through the precipitation

Table 2 γ' size (diameters) overview based on the reviewed literature in "γ' phase" section

References	Ni alloy	AM process	γ' size
[116]	CM247	L-PBF	Dendritic core: 5 nm Interdendritic: 50 nm
[117]	Haynes 282	L-PBF	20–30 nm
[120]	Haynes 282	E-PBF	118 ± 23 nm
[106]	Rene N5	E-PBF	Dendritic core: 230 ± 48 nm Interdendritic: 500–2000 nm
[122]	CMSX-4	E-PBF	100 ± 50–380 ± 50 nm
[123]	Unspecified (Ti + Al = 8.6 wt%)	E-PBF	100 ± 20–600 ± 100 nm
[125]	Rene 142	E-PBF	~ 275 nm
[127]	IN738	E-PBF	Dendritic core: 5–50 nm Interdendritic: 400–600 nm
[131]	Ni–5.5Al–7.4Ta–4.4 W–7.1Co–7.5Cr–1.2Ti–2.0Mo (wt%)	E-PBF	Dendritic core: ~ 20 nm Interdendritic: ~ 100 nm

temperature range from 700 to 900 °C [153] will enable γ'' formation [154, 155]. Similar diagrams have been proposed for AM IN718 [25, 146, 156, 157], which show that higher cooling rates inhibit precipitation of γ''. However, during PBF processing, preheating the build has been shown to play an important role in the formation of γ'' in IN718 [146].

For IN718 manufactured via E-PBF, the preheat temperature is generally set between 975 and 1025 °C [146, 158]. Due to these high preheat temperatures above the γ'' dissolution temperature of ~ 900 °C, γ'' may not form until after the printing process and cooling of the build. The time spent at the preheat temperature and the cooling rate after the process play major roles in the resulting γ'' size and morphology. For instance, Kirka et al. [51], who used a preheat of 975 °C, showed that γ'' size and morphology was build-height dependent. Their microstructure was reported as follows: within the top 100 µm of the part, γ'' forms in the matrix with a size of ~ 80 nm. The γ'' within this top layer was assumed to have formed shortly after the build completed during cooling. The γ'' size decreases down the build until about 5 mm where a steady state is reached at 35 nm. Further, regions surrounding δ at the grain boundaries and within the matrix were depleted of γ'' due to its decomposition into δ. At higher preheat temperatures of 1025 °C, a study by Deng et al. [158] showed that the formation of γ'' can be suppressed until after the build process, resulting in a homogeneous distribution of γ'' across the build height that formed during cooling.

Overall, the knowledge pertaining to the impact of processing parameters except for the preheat temperature on the formation of γ'', much like γ', is limited due to the small number of studies reporting on the microstructure evolution as a function of different processing parameters. While the impact of preheat temperature has been well explained, no direct correlation can be made for other processing conditions. Like for γ', the partitioning of elements impacts the formation of γ'', with Nb primarily segregating to the interdendritic regions and grain boundaries [25]. Similarly, as discussed in "γ' phase" section, the potential impact of cooling rate in PBF on the partitioning of elements and the potential impact on the formation of γ'' remains unexplored. Looking at E-PBF studies more broadly, sizes of γ'' precipitates vary from 2 nm to hundreds of nanometers depending on the build height and processing conditions [37, 94, 107, 158].

The presence of Laves phase, which consumes Nb from the γ matrix, also impacts the size and volume fraction of γ'' [50]. Coarse precipitates have been identified at low angle boundaries [159], in agreement with theories of accelerated γ'' formation due to pipe diffusion of Nb along dislocation structures [144]. Sun et al. [94] demonstrated that hardness increases from top to bottom due to the precipitation of γ' and γ'' closer to the build plate. However, these phases are also found at the top of the as-built part as shown in Fig. 12. The same authors attributed the variation in hardness to larger amounts of precipitates at the bottom regions which are exposed to

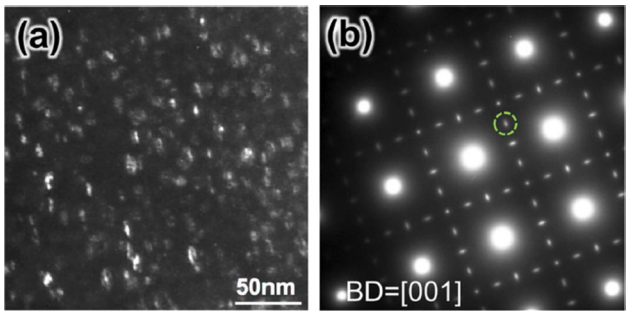

Figure 12 **a** dark-field (DF) TEM image showing γ'' precipitates on the top portion of as-built E-PBF IN718 and **b** selected-area diffraction patterns where the green dashed circle represents the (1/2 1 0) diffraction spot used to image the γ'' precipitates in (**a**). Reproduced from [94] with permission.

higher temperatures for a longer time due to reheating cycles imposed by subsequent deposited layers and extended times at elevated preheat temperatures. In agreement with these findings, Sames et al. [146], based on CCT curves, proposed that the complex evolution of precipitates at different build heights affects the mechanical strength. Co-precipitate formation, found in conventionally manufactured materials as shown by some of the current authors [143, 144] have also been identified in E-PBF IN718 via APM as shown in Fig. 13 [37]. Investigation with XRD [160], differential thermal analysis, and field ion microscopy [159] have also allowed researchers to confirm the presence of γ' and γ'' in E-PBF IN718.

In L-PBF, lower build plate temperatures and faster thermal cycling limit the formation of precipitates [61]. However, several studies have reported the precipitation of γ' and γ'' in the as-built condition. Amato et al. [161], for instance, found ellipsoidal γ'' precipitates measuring 100 nm in the major axis, arranged in a columnar fashion and aligned with textured grains. In situ precipitation has been demonstrated by Yang et al. [132] via adjustments of the thermal cycles placing the laser peak temperature between the precipitation temperature and the melting temperature. Some investigations only provide evidence of γ'' precipitation via XRD [133, 162, 163], however, in this technique overlapping diffraction peaks between the γ matrix and the precipitate phases of interest might jeopardize an accurate determination of precipitate presence or lack thereof, as mentioned above. In these circumstances, synchrotron XRD provides higher resolution and better separation of the peaks, facilitating the evaluation of the phases in the material [164]. It also seems that variations in the L-PBF printing parameters allow a wide range of morphologies of precipitates to be formed. Gallmeyer et al. [102], using high resolution transmission electron microscopy (HRTEM), were not able to confirm the identity of nanoprecipitates

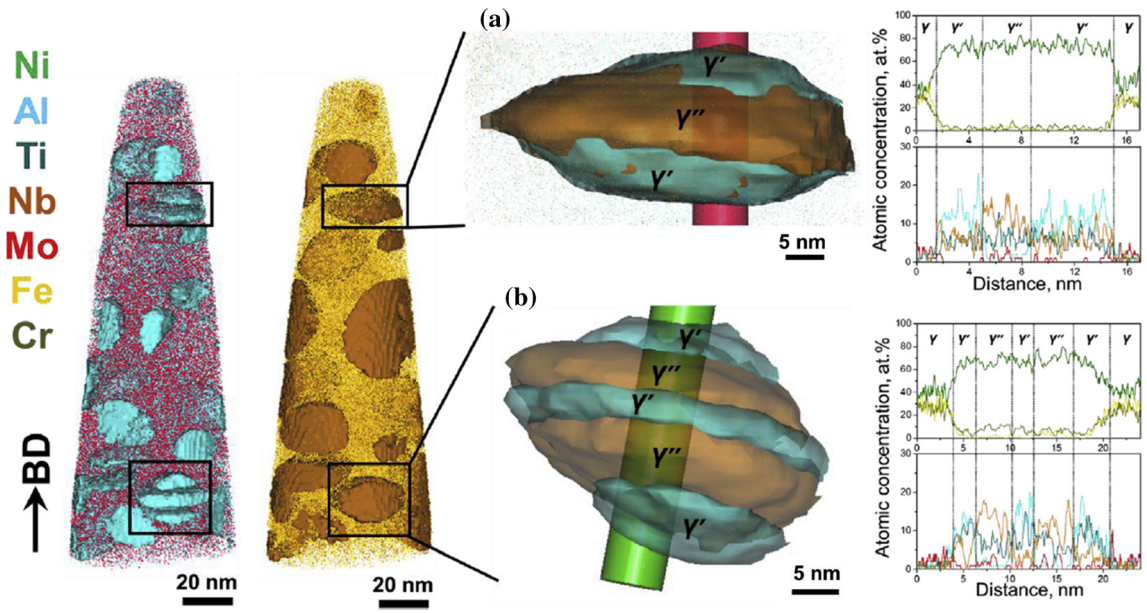

Figure 13 APM of co-precipitates of γ' and γ'' in E-PBF IN718 with **a** $\gamma'/\gamma''/\gamma'$ and **b** $\gamma'/\gamma''/\gamma'/\gamma''/\gamma'$ with respective atomic concentration profiles of Ni, Al, Nb, Mo, Fe, and Cr along the cylinder across the precipitates. Isosurface concentrations of 3 at.% of Al and 3 at.% of Nb were determined to delineate γ' and γ'', respectively. Reproduced from [37] with permission.

due to their small size. Additionally, inhomogeneous precipitation seems to occur within the build part, with re-melted regions becoming preferential precipitation sites as they are subjected to slower cooling during repeated melting cycles [165, 166]. The shape of the component influences precipitation, as shown in the study of Yang et al. [167] where thin walls manufactured under keyhole mode enabled the formation of γ' and γ'' precipitates within the fine dendrites in the faster cooling central regions. However, coarser Laves phase particles at the marginal zones hindered the formation of precipitates.

IN625 is typically categorized as a solid solution strengthened alloy, however, the presence of Nb in its chemical composition enables the formation of γ'' precipitates that further improve its strength and is therefore discussed here. Used in the aerospace industry due to its high strength and fatigue resistance, in addition to oxidation resistance and good weldability [168], IN625 has been gaining attention as a suitable alloy for PBF AM [56, 57, 169–172]. The study by Amato et al. [173] provides a comprehensive analysis of precipitation phenomena in both E-PBF and L-PBF IN625. Columnar structures containing γ'' precipitates parallel to the build direction are found in both E-PBF and L-PBF, however, in the latter, finer precipitates are observed due to faster cooling that inhibits coarsening. Larger phases are identified in L-PBF at the melt pool boundaries; however, it is not clear if these are γ'' or δ phase, since only limited phase identification has been conducted. In agreement with these finding, Murr et al. [174] found γ'' precipitates coinciding with the {111} planes of the γ matrix after E-PBF processing.

As a meta-stable phase, the γ'' phase is susceptible to transformation into δ. The δ phase will often form from meta-stable γ'' when IN718 spends extended periods of time at elevated temperatures between $\sim$ 650 and $\sim$ 1000 °C [104, 175]. When δ forms, it often has a needle or platelet like morphology [51, 94, 102, 158, 176–178]. Under L-PBF, δ has been reported to form in some studies [102, 179] while others have not reported the presence of δ [180]. The lack of δ formation in those studies is largely attributed to the high cooling rate and abundance of Laves, decreasing Nb content within the matrix [180]. Due to the generally small size of phases precipitated in L-PBF, identification of δ may be difficult. Looking at a study that has reported δ formation [96], there are some questions on whether it could be indeed misidentified Laves or (Nb,Mo)-carbides due to their typical spherical to blocky morphology. Further, it is hard to confirm this purely by energy dispersive spectroscopy (EDS) analysis, as the excitation volume of the electrons result in the sampling of the surrounding matrix too [181]. Other authors such as Sarley et al. [182] and Gribbin et al. [183] have, however, provided evidence for δ phase formation in as-built L-PBF IN718 via synchrotron and XRD, respectively, with the latter identifying a 3.81% volume fraction of δ phase. A study by Ferreri et al. [181] also confirms the presence of δ through neutron diffraction. Interestingly, in this work, the δ phase is also visible in SEM images, whereas in most studies the δ is too small to be resolved. The larger size may be attributed to the high laser power of 285 W and lower laser speed of 960 mm/s. However, as many studies are not reporting a complete list of processing parameters such as hatch spacing, it is not possible to give an exact explanation on the differences of δ formation within L-PBF IN718.

Within E-PBF, the formation and morphology of δ shows a strong dependence on the preheat temperature and location along the build direction due to the in situ heat treatment that occurs. Kirka et al. [51] specifically outlined three zones in their samples shown in Fig. 14a where the evolution of δ containing microstructures in E-PBF printed with a preheat temperature of 975 °C can be observed. The 975 °C preheat temperature is noted to be within the temperature range in which δ nucleates. In these regions, δ was noted to form in regions 2 and 3 as shown in Fig. 14b, c. δ did not form in region 1. The reason for the lack of formation of δ in region 1 can be largely attributed to insufficient time at the preheat temperatures to cause δ nucleation. This region encompasses the top 600–750 μm of the build. Starting at region 2, which occurs after region one and spans $\sim$ 3.5 mm, δ phase was noted to form at the grain boundaries in a zipper-like morphology in large parts due to the diffusion and partitioning of Nb toward the interdendritic regions, and the likely dissolution of Laves phase that occurs due to the intrinsic heat treatment. Region 3 represents the steady-state bulk microstructure of E-PBF IN718. Here, the δ phase is present across the columnar grains in both zipper-like and globular morphologies. Further, it was noted that regions of intergranular δ formation were stripped of γ'', shown through TEM-EDS, and that overall,

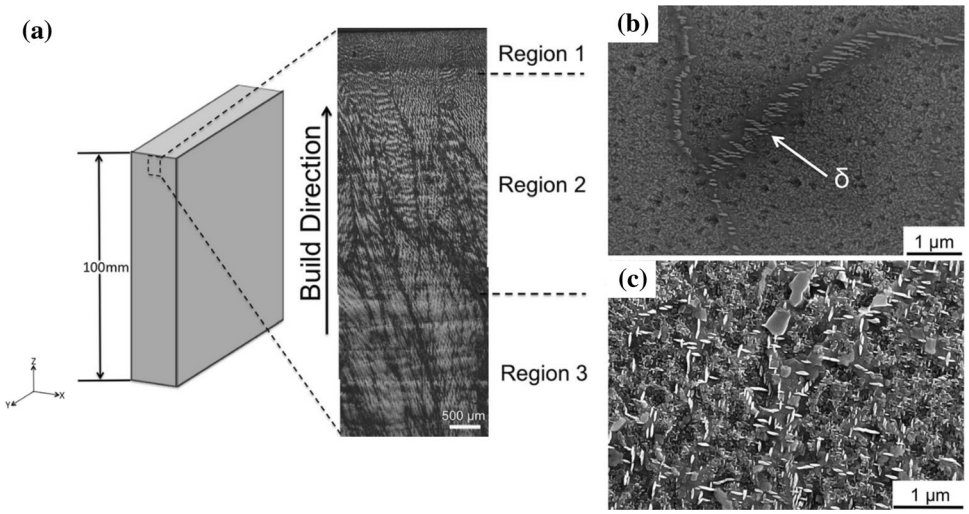

Figure 14 **a** Schematic diagram showing the three distinct microstructure regions for E-PBF IN718 where region 1 encompasses the top 600–750 µm, region 2 spans the proceeding 3.5 mm below region 1, and region 3 represents the bulk of the sample. **b**, **c** back scatter (BS) SEM images showing **b** zipper-like δ formation commonly present along grain boundaries in region 2 and **c** bulk needle-like δ morphology common in region 3. Adapted from [51] with permission.

the γ'' phase within region 3 had decreased in size pointing toward the transformation of γ'' to δ.

In general, many studies have shown the zipper-like morphology of δ under E-PBF as well as the formation of interior platelet δ [90, 146, 178]. However, this morphology of δ is dependent on a preheat temperature that allows for the nucleation and growth of δ during the printing process. A study by Deng et al. [158] showed that it is possible to limit the formation of δ through the processing of IN718 at preheat temperatures above 1000 °C. Above the given preheat temperature, δ is unable to form and the cooling process after build completes occurs fast enough to suppress its formation outside intergranular regions. It was only after a solution heat treatment at 980 °C that δ nucleated in the zipper like morphology which is characteristically reported in many published E-PBF studies on IN718 that were printed at lower preheat temperatures. Further, Lee et al. [37] studied processing of IN718 in E-PBF at 1025 °C showing similar results on limited δ formation while also linking the cooling rate from the processing conditions to the amount of δ formation.

Other secondary precipitates and TCP phases

The formation and morphology of TCP and other secondary precipitates vary between L-PBF and E-PBF processes due to the differences in cooling rate and the intrinsic heat treatment that occurs in E-PBF. For Ni-based superalloys, the TCP phases usually include σ, μ, R, P, and Laves, and their occurrence is largely dependent on the alloy, solidification conditions, and preheat conditions if applicable. Table 3 lists TCP phases, carbides, nitrides, oxides, and borides typically found in various L-PBF and E-PBF printed Ni-based superalloys.

Overall, carbides regardless of the PBF process were noted to be mostly MC-type with a few exceptions [117, 184, 185]. MC-carbides are generally more stable than M_6C and $M_{23}C_6$ [40, 186]. These carbides are stable to high temperatures up to ~ 1350 °C and form within the mushy zone [25, 187–189]. Therefore, their morphology is heavily influenced by solidification conditions such as the solidification velocity and thermal gradients [188, 190]. Within PBF processed Ni-based superalloys, carbide morphologies have been found to range from spherical to "script"-like. Spherical carbides tend to form at faster cooling rates. As the cooling rate decreases the size of the spherical carbides increase. At slower cooling rates, the carbides begin to form "script"-like morphologies. Therefore, processing parameters that result in fast

Table 3 List of various TCP and carbide, nitride, oxide, and boride phases found in various L-PBF printed Ni-based superalloys

Alloy	L-PBF	E-PBF
CM247LC	(Hf, Al)–oxides [116] Ti, Hf, Ta, Mo, W–carbides [116]	
CMSX-4	Laves [80]	Re, W–TCP phase [124, 139, 196] μ [108]
DZ125		Hf–carbides [135]
Hastelloy X	No TCP or carbides reported [197, 198] Mo–carbides [199–201] Mo–M_xC_y carbides [195, 202] Mo–M_6C carbides [202, 203] Mo–$M_{12}C$ carbides [202]	Mo, Cr, Ni, W, Si-M_6C Carbides [204–206] Cr–$M_{23}C_6$ carbides [205, 206]
Haynes 230	Cr, Mo–$M_{23}C_6$ carbides [184]	
Haynes 282	Ti, Al–oxides [117] Ti, Mo–MC carbides [41] Cr, Mo–$M_{23}C_6$ carbides [117]	Ti, Mo–MC carbides [120]
IN625	No TCP or carbides [57, 207] Nb, Mo–carbides [56, 192] Nb–MC carbides [171] Laves [192]	
IN718	δ[96, 181] No TCP or carbides reported [96, 133, 208] Laves [98–100, 102, 191, 209] Nb, Ti, Al, Mo–carbides [98, 99, 102, 181, 191, 209]	δ[37, 94, 107, 177] Laves [37, 50, 107] Nb, Ti–carbides [37, 50, 94, 107, 159, 177] Nb, Ti–borides [37, 94, 107, 159] Ti–nitrides [38, 50, 159]
IN738	Nb, W, Ti–carbides [43, 185, 210] Cr–$M_{23}C_6$ carbides [185]	Nb, W, Ti, Mo–MC carbides [127]
Nimonic 263	Ti–carbides [103]	
Rene 142		Hf–carbides [125]

solidification conditions are more likely to lead to smaller spherical carbides, while processing parameters that result in slower solidification conditions are more likely to lead to either larger spherical or "script"-like carbides. The types of carbides, based on the selection of alloys presented in Table 3, are strongly dependent on the alloy composition. Carbides are most often found at grain boundaries and interdendritic regions. Elements conducive to carbide formation, such as Mo, Nb, and Ti, partition to these locations due to solidification conditions triggering carbides formation [116, 191].

The formation of carbides in Ni-based superalloys provides superior creep properties due to their potential pinning effect minimizing grain growth and cellular boundary migration at high temperatures, as well as serving as obstacles for dislocation slip during deformation [40]. However, the general type and morphology of carbides found in PBF processes lead to challenges for their use as strengtheners. For example, in Haynes 282, with only 19 vol.% γ' formation, the amount and morphology of carbides contribute significantly to the high temperature creep strength [120]. Haynes 282 has been specifically designed to be heat-treated to form blocky $M_{23}C_6$ and/or M_6C carbides at the grain boundaries. Under E-PBF, however, MC carbides were noted to form instead with a spherical morphology at the grain boundaries (Fig. 15a), and at lower volume fractions when compared to wrought Haynes 282 counterparts. EDS analysis further confirmed that these carbides were mainly composed of Ti and Mo (Fig. 15b) compared to traditionally wrought Haynes 282 where carbides also contained Cr. Consequentially, due to the differences in carbide morphology and volume fraction, making them insufficient to block dislocation motion, E-PBF Haynes 282 was noted to have inferior mechanical properties compared to its

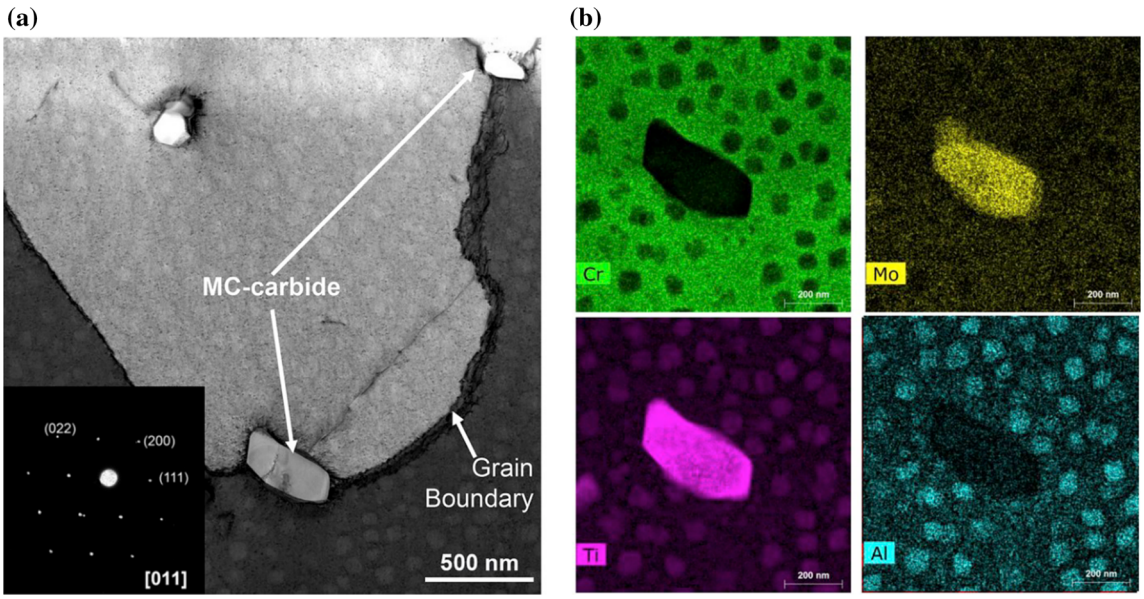

Figure 15 **a** Bright-field STEM of Haynes 282 showing the formation of MC-carbides at a grain boundary, **b** EDS results showing these carbides to be composted of Mo and Ti. Reproduced from [120] with permission.

wrought counterpart, demonstrating some challenges within AM for the use of carbides for strengthening [120].

There are some differences in carbide formation between L-PBF and E-PBF due to differences in solidification conditions. The general spherical or "script"-like morphology has the potential to form under both processes based on the reviewed literature in Table 3 (as shown in Fig. 16g, h). However, under L-PBF, the size of these particles tends to be sub-micron (Fig. 16g) and generally smaller than E-PBF carbides due to the faster solidification conditions. They often form in a spherical morphology and are observed to be smaller than ~ 500 nm

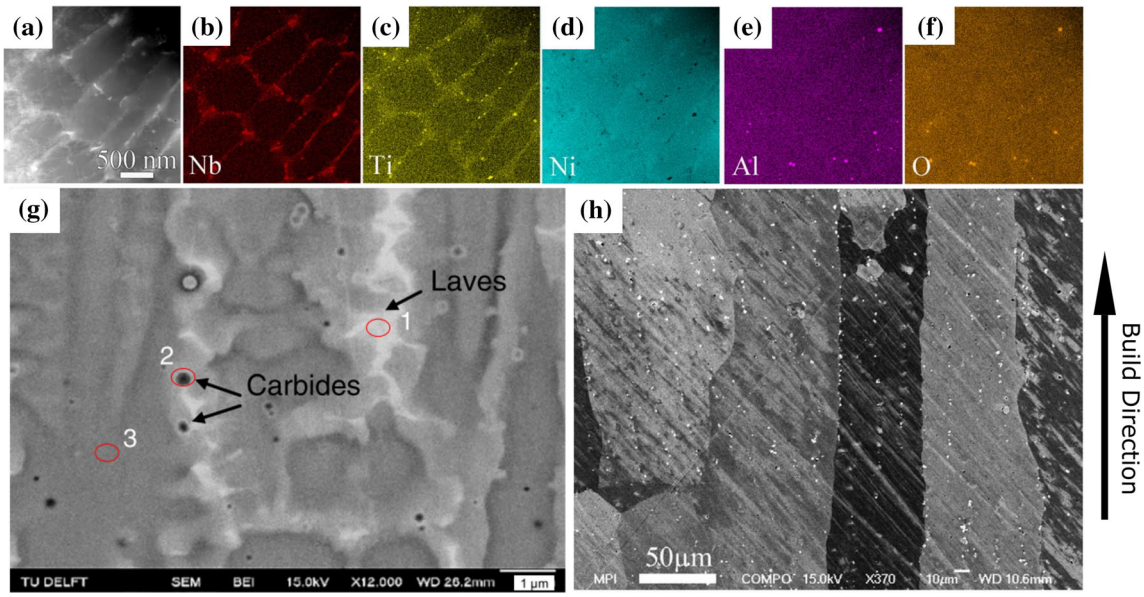

Figure 16 **a** HAADF-STEM micrograph and **b–f** STEM-EDS maps highlighting segregated elements and percipitation of carbides and oxides [102]. **g** Backscatter SEM image of L-PBF IN718 showing the formation of sherical carbides and Laves phase [191]. **h** High resolution SEM image of E-PBF IN718 showing long chains of carbides that follow the build direction at grain boundaries and within grains [159]. **a**, **b**, **c**, **d**, **e** and **f** adapted from [102], **g** from [191], and **h** from [159] with permission.

[98, 116, 171, 191, 192]. It has also been found that fewer carbides form during L-PBF compared to E-PBF. During processing by E-PBF, due to the slower solidification rates, larger chains of carbides form along the grain boundaries, following the build direction as seen in Fig. 16h. These carbides are more likely to be of a script-like morphology due to the slower solidification rates [190]. The intrinsic heat treatment that occurs within E-PBF builds seems to not largely impact carbide morphology within any of the examined Ni-based superalloys given in Table 3 and therefore, most carbides do not exhibit similar microstructure gradients as seen with γ', γ'', Laves, and δ. In regards to $M_{23}C_6$, they are found in conventionally manufactured Ni-based superalloys but are only rarely reported in AM [187, 189, 193, 194]. Here, MC will transform into $M_{23}C_6$ such that $\gamma + MC \leftrightarrow \gamma' + M_{23}C_6$ [193] particularly at lower temperatures around 732–760 °C [193]. Due to high cooling rates and, specific to E-PBF, high preheat temperatures, the transformation is most likely suppressed for most Ni-based superalloys. In general, for AM Ni-based superalloys, $M_{23}C_6$ has been shown to nucleate during heat treatments [41, 171, 185] leading to some indication that its lack of formation may be in part due to a lack of aged microstructure. Of interesting note however, is that many studies have also shown no impact on carbides during heat treatment dependent on temperature and alloy composition [158, 176, 195]. Overall, there is complexity in the impact of heat treatment on carbides that needs to be studied in more detail in the future.

As mentioned earlier, most carbides formed during L-PBF and E-PBF have been reported to be of the MC type. Only a few studies show the formation of other carbides such as $M_{23}C_6$ [117, 184, 185]. For example, within the Haynes 282 alloys printed via L-PBF, there are conflicting reports on carbide formation. One study reports only the formation of Ti and Mo containing MC-carbides [41]. Another investigation reports the formation of mixed Cr and Mo rich $M_{23}C_6$ carbides in samples printed without a heated build plate, and no carbide formation in samples printed with a heated build plate [117]. One explanation for the difference in carbide formation may be differences in energy density. The study which reported the formation of $M_{23}C_6$ carbides used a higher volumetric energy density compared to the one that only reported the formation of MC carbides. The higher energy input would likely contribute to higher sample temperatures and decreased cooling rate during the AM process and thus, might enable the formation of $M_{23}C_6$ carbides [71]. However, it is interesting to note that the study that reported the formation of $M_{23}C_6$ carbides reported it in a build with no preheat. However, the build produced with a 300 °C preheated build plate showed no $M_{23}C_6$. Traditionally, the use of build plate preheating would result in lower cooling rates. As carbides are important for controlling Haynes 282's mechanical properties, more work needs to be conducted to verify the types of carbides that form during AM of this alloy. Further consideration needs to be made on how changing solidification conditions and cooling rates may impact carbide formation.

Hastelloy X, known as a solid solution Ni-based superalloy, is unique in that it does not form any γ' or γ'' phases. Instead, it achieves its strength through the additions of primarily solid solution elements and carbide formation. For this reason, compared to other Ni-based superalloys discussed here, it contains a relatively high amount of Mo for strengthening. It also forms several carbides which have not been commonly seen in other PBF processed Ni-based superalloys. Under traditional manufacturing routes, Hastelloy X is known for forming M_6C and $M_{23}C_6$ carbides rich in Mo and Cr [189, 211]. Under L-PBF, however, there have been conflicting reports on the carbide formation. Multiple studies [197, 198, 212] have reported no carbide formation in as-built samples while other studies [195, 199–203] have reported the formation of complex carbides that are uncommon in most PBF alloys. For that reason, Hastelloy X is discussed in depth here. In the former case, Harrison et al. [198] reasoned that the occurrence of solute trapping of elements due to the high cooling rates in L-PBF resulted in a lack of elemental segregation of Mo and Si, and a lack of depletion of primary matrix elements, i.e., Ni, Cr and Fe, to the interdendritic regions, thus, resulting in the absence of formation of any secondary particles. SEM imaging showed a lack of secondary particle formation. EDS line scans performed at cracked regions, often the site for elemental segregation and carbide formation, showed no indication of elemental segregation. The lack of elemental segregation next to the cracked region was used as supporting evidence for their theory that solute trapping had occurred, and secondary precipitate formation was suppressed.

However, other studies report conflicting results. For instance, using TEM-EDS, Han et al. [213] showed the occurrence of elemental segregation in the region of a crack rich in Mo, and C. They similarly report no formation of carbides in their as-built samples using the original Hastelloy X composition. A potential explanation for the reported difference in elemental segregation could be the extremely fine microstructure variation due to the high cooling rates. These fine microstructures may make it difficult to pick up variations in the elemental segregation in regions of interest such as cracks using standard EDS-SEM techniques. Furthermore, elemental partitioning may not only be impacted by the cooling rate but also by other solidification parameters such as the solidification velocity, thermal gradient, and undercooling [214] that may have not been considered in the initial studies.

Notably, other studies have reported carbide formation in Hastelloy X after L-PBF processing [195, 199–203]. The carbide phases reported by these researchers are primarily spherical Mo-enriched M_6C, $M_{12}C$, and M_nC_m and, therefore, are notably different from the predominantly MC carbides seen in most other Ni-based superalloys processed by PBF. A summary from various studies on their reported phases, PDAS, and cooling rate are given in Table 4. Overall, the variation in reported PDAS, which is often used to estimate cooling rate, leads to the conclusion that cooling rate is likely not a factor that will impact the type of carbides forming. By extension there is no indication from the PDAS that a faster cooling rate could be suppressing the elemental partitioning that would lead to carbide formation. From the observed studies L-PBF processed Hastelloy X carbides had a spherical morphology and were mostly Mo-enriched M_6C or M_nC_m particles of sizes as small as $\sim$ 55 nm to sizes up to 500 nm [195, 200–203]. One primary reason for the formation of other carbide types compared to most other alloys produced by L-PBF may come from the fact that the high Mo content within Hastelloy X makes M_6C carbides more stable. Therefore, from the covered literature on Hastelloy X and the understanding that most Ni alloys form some type of carbides, the conclusion can be made that during L-PBF, Hastelloy X will form primarily spherical Mo-enriched M_6C, $M_{12}C$, and M_nC_m. Further, in L-PBF, there appears to be little control over their morphology when changing solidification conditions based on cooling rate.

Looking at Hastelloy X processed by E-PBF, Karapuzha et al. [205], showed that carbides larger in size and higher in number density formed compared to those in L-PBF. These carbides, seen along grain boundaries, were noticeably elongated compared to L-PBF carbides. Another study by the same authors [206] has also shown that the morphology of carbides within Hastelloy X can range from rod-shape to globular while carbides ranged from $\sim$ 0.2 to 1.5 μm in size. Through EDS, these carbides were identified as enriched in W, Mo, and Cr and thus, were most likely (W, Mo)-rich M_6C and Cr-rich $M_{23}C_6$. It was also noted that M_6C carbides contained increased Cr content when compared to the matrix. As M_6C decomposes into $M_{23}C_6$ at temperatures above 650 °C the authors postulated that due to the preheat temperature of 750 °C some of the M_6C had decomposed or were in the process of decomposing into $M_{23}C_6$ carbides. Further work on the geometric variation of carbides across the build height of such parts would likely confirm this.

Depending on the content of impurities in the powder used in PBF, it is possible for other secondary precipitates such as oxides, borides or nitrides to form. For instance, in E-PBF multiple studies noted the precipitation of Ti-nitrides in IN718. These nitrides were also noted to be potential nucleation sites for (Nb, Ti)–carbides, therefore creating core-

Table 4 List of PDAS, cooling rates and associated reported carbides for various studies on Hastelloy X processed by L-PBF

References	PDAS (um)	Cooling rate (K/s)	Carbides
[202]	0.65 ± 0.25	4.5×10^5	Spherical, globular, and elongated Mo-enriched M_6C, $M_{12}C$, and M_nC_m
[215]	0.5, 1–2	Not reported	Spherical carbides reported for both low and high-power laser modes
[198]	0.9–1.2	3×10^5	No carbides reported
[201]	0.4 ± 0.06	$1 \sim 2 \times 10^6$	Spherical Mo-enriched M_6C or M_nC_m
[195]	0.5	Not reported	Spherical Mo-enriched M_6C or M_nC_m
[216]	< 1.0	Not reported	Spherical carbides

shell structures [50, 159]. The Ti–nitride and Ti–carbide core-shell structure has been reported under traditional manufacturing routes as well for IN718. During casting and directional solidification, primary Ti–nitrides first precipitate from the melt followed by nucleation of Ti–carbides on the Ti–nitride surfaces, resulting in the core-shell structure [217, 218].

Likewise, a limited number of studies have reported the nucleation of oxides and borides. For instance, a report on IN718 showed the formation of spherical Al–oxides, as shown by EDS analysis presented in Fig. 16a–f where coinciding concentrations of Al and O can be seen [102]. Similar results have been shown for CM247LC where (Hf, Al)–oxides were noted [116]. Aluminum oxides have also been reported to be accompanied by a TiN shell similar to what has been reported previously for carbides in IN718 [219]. In some studies on E-PBF IN718, due to concentrations of B in the processed powder, spherical borides have also been reported to form [37, 94, 107, 159]. These borides, carbides, oxides, and nitrides, often being nm-sized and spherical in morphology, can potentially look similar to nanometric gas porosity, and can be difficult to differentiate using SEM. This necessitates the use of other methods such as EDS for proper identification of elements [219].

Looking at TCP phases, based on our review of the existing literature, only Laves and μ phase are reported to form amongst the given alloys listed in Table 3 after processing by PBF. The lack of formation of other TCP phases can likely be attributed to the lack of in situ aging in the microstructure and fast cooling rates. The Laves phase specifically, has an AB_2 HCP structure and a chemical composition of $(Ni, Fe, Cr)_2(Nb, Mo, Ti)$ [48, 50]. Generally, Nb, Al, Si and Ti are considered to promote Laves formation [40]. During PBF processing, alloys such as CMSX-4, IN625, and IN718 were noted to be prone to the formation of this phase. Overall, Laves may improve properties if present in small quantities in a granular morphology through promoting a pinning effect, and minimizing grain growth and cell boundary migration during high temperature exposure [102, 178, 179, 220, 221]. In its globular chain-like morphology, in contrast, it is highly detrimental to ductility [145, 152, 221]. Looking at IN718 as an example, the formation of TCP phases should not occur during L-PBF based on typical CCT diagrams [146]. The expected lack of Laves formation is further supported by simple cooling experiments on IN718 which seem to indicate that Laves formation should be suppressed at cooling rates experienced during L-PBF [222]. However, based on several reports in AM literature, it becomes clear that non-equilibrium formation of Laves does occur [50, 98, 99, 191, 209, 223]. This may be due to the repeated melting that occurs from the layer-by-layer process within L-PBF, and the high level of Nb microsegregation. Laves phase formed in these alloys is noted to be of an irregularly shaped eutectic morphology, in either γ + Laves or divorced forms, which can coexist with carbides and can be located within the interdendritic regions, cell boundaries, or grain boundaries as shown in Fig. 17a for L-PBF [99]. In general, Laves formation comes at the expense of Nb depletion in the matrix, a known solid solution strengthener [40], and can decrease the formation of γ'' in IN718 [50, 167, 223]. Through APM (Fig. 17b, c, and d), it has been shown in IN718 that from the surrounding matrix into the Laves phase, the Nb concentration increases from 2 to 20 at.% (Fig. 17d) [179, 223]. Overall, the size of Laves phase in L-PBF printed alloys varies greatly with cited measurements ranging between as low as 17 nm and as high as 1–2 μm [80, 191]. These variations are likely dependent on the processing parameter selection, which will influence resulting thermal conditions and alloy local composition.

In the literature, there are numerous instances where Laves is impacted by changing thermal conditions. For instance during L-PBF, it has been shown that changing the angle at which the part is printed by up to 45° can result in an increase in the phase fraction of Laves, and a switch from discrete (Fig. 18b) to long-chained continuous networks (Fig. 18a) [89]. As changes in part orientation have been shown to impact thermal conditions in a build, likely the rotated samples experienced slower cooling compared to the parts aligned with the build direction [224]. The change in cooling rate from changing the part orientation likely resulted in increased partitioning of Nb to the grain and cell boundaries. The increase in Nb thus permits a greater phase fraction of Laves to form as a continuous network. Similarly, a switch from a continuous laser to a pulse laser in L-PBF resulted in a similar change in the morphology of Laves. The continuous laser (Fig. 18c) showed more long-chained networks of Laves while the pulse laser showed more discrete regions (Fig. 18d) [54]. These differences were attributed to solidification conditions with the continuous laser resulting in

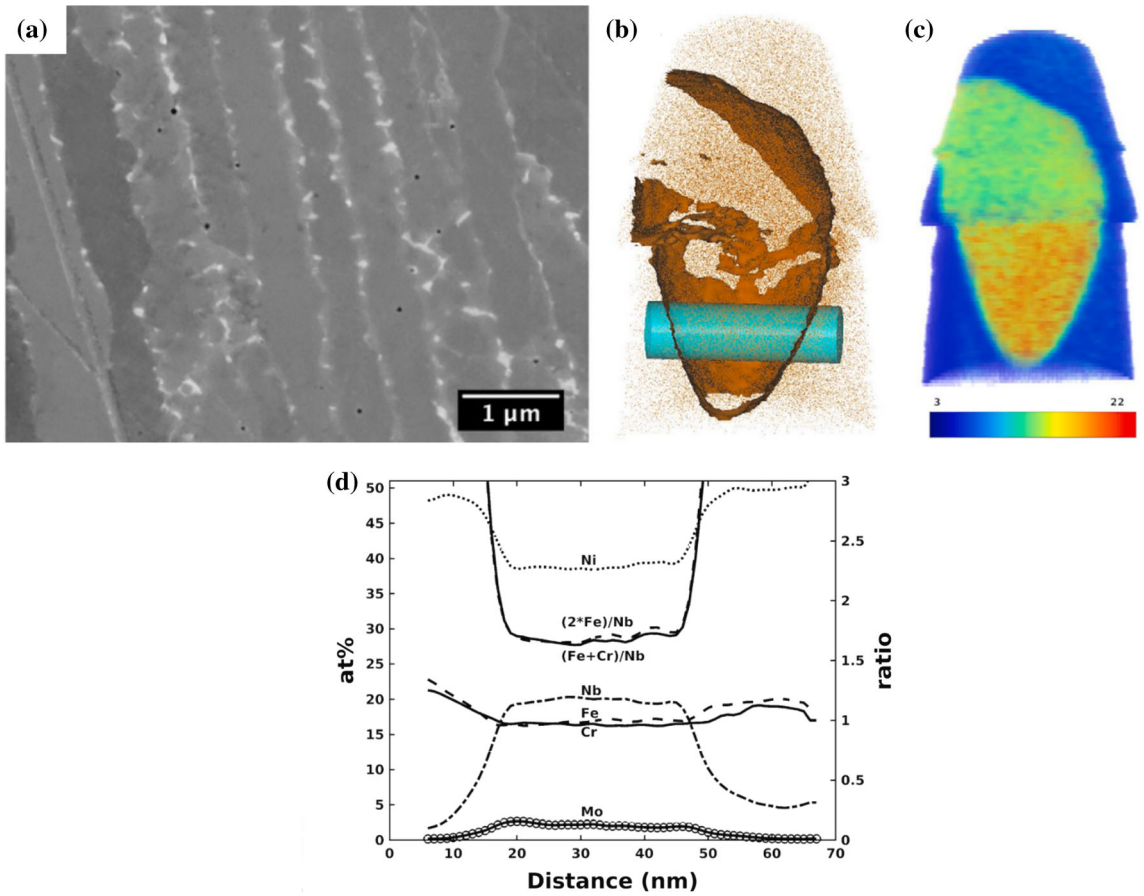

Figure 17 **a** Field emission gun (FEG)-SEM image of chain-like Laves phase formation along the build direction of the interdendritic region in a L-PBF IN718 sample [99]. **b** APM Nb map and color maps for an L-PBF IN718 sample showing Nb distribution along an interdendritic region. **c** Elemental distribution along a cylindrical ROI shown in **d** confirming the formation of Laves phase along interdendritic regions. **a** Reproduced from [99] and **b**, **c**, and **d** from [179] with permission.

coarse columnar dendrite growth due to a consistent solidification direction that permitted the continuous growth of Laves from partitioned Nb. The pulse laser, however, leads to multi-directional solidification of the melt pool that results in more fine equiaxed dendrites that split the partitioned Nb content in the interdendritic region resulting in more discrete Laves. Likewise, a similar trend can be seen between samples using a bidirectional and checkerboard scan strategy. The bidirectional scan strategy resulted in continuous networks of Laves (Fig. 18e) while the checkerboard scan strategy resulted in discrete Laves (Fig. 18f) [149]. Therefore, the processing conditions will play a role in determining the phase fraction and morphology of Laves by changing the resulting grain boundary and interdendritic distribution of Nb that is needed for Laves to nucleate and grow.

During E-PBF, the distribution and morphology of Laves will be impacted by similar factors as in L-PBF; however, under E-PBF, one must also consider the additional impact of the high preheat temperatures. In this case, due to the intrinsic heat treatment effect, the morphology of Laves changes based on the build height as outlined in Fig. 19. Overall, Laves is present in only the top layers of builds. A study by Deng et al. [50] looked at the evolution of Laves phase along the build direction. They showed a spherical morphology at a region 50 µm below the top of the build. The Laves phase continues to coarsen into a script-like morphology until around 150 µm before fully dissolving back into the matrix due to the diffusion of Nb caused by the elevated build temperatures [50]. Past $\sim$ 1800 µm, the Laves fraction was noted to reach $< 0.1\%$ and the microstructure was considered fully homogenized. In the case for IN718, the locations inhabited by the dissolved Laves phase will

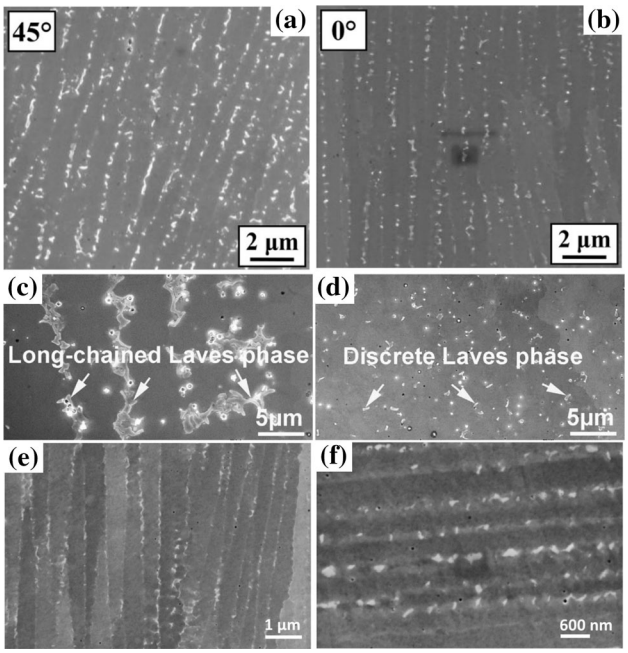

Figure 18 Examples of how changing thermal conditions can lead to either long-chained continuous Laves phases **a**, **c**, **e** or discrete Laves phases **b**, **d**, **f** in IN718. **a**, **b** show the impact of part orientation, **c**, **d** show the impact of changing from a continuous laser **a** to a pulse laser **b**, and **e**, **f** show the impact of changing scan strategy. **a** and **b** adapted from [89], **b** and **c** from [54], and e and f from [149] with permission.

traditionally precipitate δ-phase due to the increased local Nb contents. Overall, the exact location across the build height for which the Laves phase evolves will be process and alloy dependent.

Lastly, differences in the TCP phases between L-PBF and E-PBF have only been reported in CMSX-4 alloy. While elongated Laves phase was noted to form in L-PBF CMSX-4 [80] there is no report on Laves formation during E-PBF [108, 124, 139, 196]. Instead, Ruttert et al. [124] and Ramsperger et al. [122] identified the formation of a small spherical TCP phase along grain boundaries rich in refractory metals such as Re. Parsa et al. [108] used STEM SAED and identified a TCP phase to be most likely μ phase and showed that it had a rather elongated spherical morphology.

Review of characterization techniques

The first part of this review highlighted the complex hierarchical microstructures of Ni-based superalloys with constituents of different sizes (from mm down to atomic scale). This reveals the significant role that microstructural characterization plays in further development and assessment of critical parts manufactured by AM. As such, we now provide an overview of the main techniques that can be used to characterize the microstructure of these complex engineering alloys. We intend the following section to be used as a guide for researchers aiming to establish a link between processing, structure and performance of Ni-based superalloy AM parts. We conclude this section with a case study on the characterization of E-PBF IN738, where it is shown how different aspects of microstructure can be unveiled using a variety of correlative microscopy methods.

Optical microscopy

Light optical microscopy (LOM) provides a straightforward view of macro- to microscopic features of materials. By using visible light and a combination of lenses in the objectives and the eyepieces, magnifications of typically up to 1000× can be achieved [225]. However, lower magnifications are more commonly used to show large areas, where several images can be stitched together with the aid of specialized computer software. LOM is often used for initial macroscopic examination of AM Ni-based superalloys, as a myriad of adjustable processing parameters enables the formation of multiple morphologies of grains and melt pools [56, 161, 226]. For instance, LOM has been used to show that the meander scanning strategy generates a finer and more homogeneous distribution of melt pools in comparison to chessboard strategy in IN718 [223]. Higher laser power produces deeper melt pools while faster scan speeds make the melt pool shallower [227]. Other features of interest such as pores and cracks can be observed in polished surfaces [228], while additional microstructural constituents such as grain and melt pool boundaries might require chemical etching to be revealed [229]. The main reagents used for this purpose in Ni-based superalloys are Glyceregia and Kalling's reagent [230, 231], although several other HCl-based etchants are used to attack specific phases such as γ'. Micron-scale secondary phases such as carbides, Laves, and δ phase are likely to be seen via LOM, however, additional characterization techniques might be necessary to chemically distinguish and identify them.

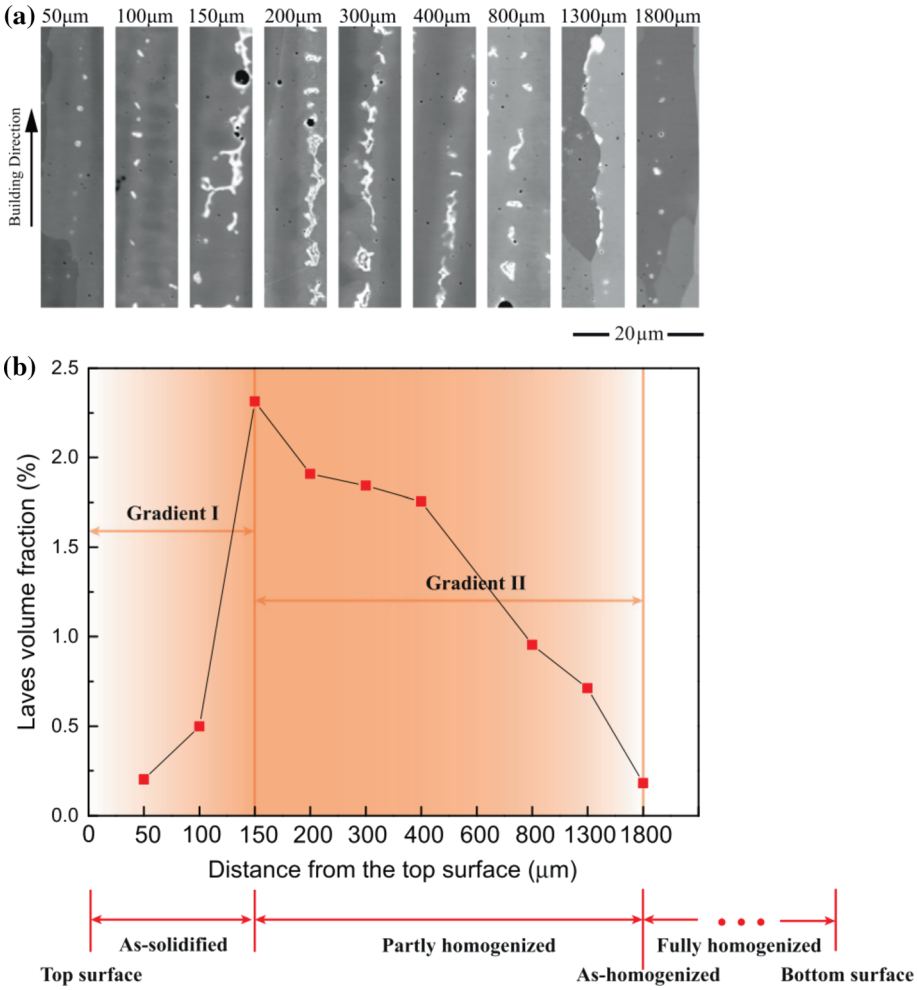

Figure 19 **a** Examples of Laves morphology in E-PBF IN718, demonstrating a location dependent morphology due to preheat temperature. **b** Laves volume fraction for the corresponding regions presented in (**a**). Reproduced from [50] with permission.

Scanning electron microscopy (SEM)

SEM is the most convenient and versatile electron microscopy method for studying the microstructure of AM Ni-based superalloys. As can be seen in Figs. 3, 5, 7, 8, 9, 14, 16, 18, and 19 for example, SEM can provide reliable insights into the morphology of γ, γ' and other phases that are of sizes $> \sim 20$ nm due to its 2 nm resolution. Further examples of the extensive uses of SEM include characterizing initial powders, cracks and porosities, and melt pool boundaries [54, 149, 223, 232–234]. SEM operates on the basis of an electron beam scanning the surface of a conductive sample in a vacuum chamber. The two main imaging modes of secondary electron (SE) and backscattered electron (BSE) imaging have been useful within Ni-based superalloys depending on the features of interest. Under SE contrast, the image develops depending on the surface topography. SE contrast therefore is most useful with etched samples where the features exposed are dependent on the etchants used. For example, melt pool and dendrite analysis is possible under SE as shown in Fig. 3d which gives useful clues related to solidification conditions. SE can also be used to help in the identification of μm-scale phases such as in Fig. 7a, b, and c where SE helped in identifying carbides, coarse interdendritic γ', and dendritic γ' in E-PBF printed high γ' forming Rene-N5. Figure 14b, c shows its use in identifying the formation of δ within E-PBF IN718.

BSE, on the other hand, provides density contrast between elements, therefore being useful for identifying microsegregation and phases with significantly different Z-numbers. Under certain circumstances, BSE detectors can also be used to provide channeling contrast to reveal areas of different orientations [235]. An example of the use of BSE can be seen in Fig. 3e, where microsegregation of elements seen as a lighter shade of gray occurs around the darker colored γ matrix. BSE has also often been used in the

characterization of γ' formation in E-PBF samples as seen in Fig. 9 through Fig. 10. Further examples can be seen in Fig. 16g, h where carbides and Laves phase were identified in the γ matrix through differing Z contrast for L-PBF and E-PBF IN718. It should be noted, however, that SEM has resolution limitations and therefore is not always suitable for the identification of all phases within Ni-based superalloys, especially those that are nanoscale. The study by Lee et al. [37] highlights SEM limitations by showing the formation of nanoscale sandwich $\gamma'/\gamma''/\gamma'$ structures under APM which are not generally visible under SEM.

As has been reviewed in this paper, chemical analysis is also important in the characterization of phase constituents. SEM fitted with EDS quantifies the chemistry based on the X-ray photons that are released from electron beam/sample inelastic interactions. Overall, EDS is only semi-quantitative and is only reliable for elements that have a Z number higher than 14. Furthermore, the excitation volume from which X-rays are emitted can be as large as 1 μm in SEM, which correspondingly limits the spatial resolution of analysis [236]. Due to the small size of microstructure constituents, only a limited number of features can be identified such as TCP phases [54], large carbides [120], or in some case elemental segregation [55]. SEM–EDS is usually not capable of identifying γ', γ'', and in certain cases δ. SEM–EDS, therefore, may be ideal for initial observations, however, more accurate chemical analysis of PBF samples and the elemental characterization of γ, γ', and γ'' may be better carried out using other methods such as TEM-EDS, where, due to using thin samples, EDS has a much smaller excitation volume.

Electron back scatter diffraction (EBSD)

EBSD is an SEM-based technique that can provide local information regarding crystal structure and orientation at the surface of a polished specimen. This method is based on the collection of elastically scattered BSEs that are emitted with special angular distributions [237]. Those electrons which constructively satisfy the Bragg's law will diffract and form Kikuchi bands. These bands are unique for different planes in different crystalline structures; therefore, they can be used to extract the crystalline structure and orientation of different regions of a microstructure. EBSD analysis in the SEM is highly automated and has emerged as a widespread technique in the analysis of crystallographic information of metal microstructures. SEM machines that are used for EBSD analysis are furnished with a special holder that tilts the specimen $\sim 70°$ with regards to the electron beam, and a detector with a phosphor screen that collects the diffracted BSEs over a large solid angle.

The crystallographic orientation of a grain is specified as the relative position of the crystal coordinate compared to the reference coordinate system (see for example Fig. 3). From orientations of two adjacent grains, their crystallographic misorientation can be determined, a parameter that can affect different types of properties of a polycrystalline material. EBSD readily provides information on the phase, grain orientation, density of dislocations, interface character, and texture, to name a few.

For Ni-based superalloys produced under PBF processes, EBSD often has been used for gaining insights on the solidification conditions. Many studies on both E-PBF and L-PBF have tracked how changing the processing parameters or part geometry may influence the resulting solidification conditions and, therefore, change the resulting grain structure [71, 82, 140, 238]. One example is the study by Gokcekaya et al. [82], shown in Fig. 3a, b, and c, where EBSD has been able to show how L-PBF parameters can affect the microstructure and in turn mechanical anisotropy. It should be noted, however, that while EBSD can be a good indicator on potential solidification conditions, it does not necessarily correlate well to phase evolution within a given part as it is unable to separately identify γ, γ', and γ'' and their evolution after solidification.

EBSD can also be used for dislocation analyses. For such purposes, the sample preparation is pivotal. This is because the possible surface plastic deformation from grinding/polishing or scratches can lead to unreliable analyses. There are several studies using EBSD to analyze dislocations and residual stresses in PBF processed Ni alloys. Terris et al. [172] printed IN625 samples using L-PBF with three different build plate temperatures. By looking at the geometrically necessary dislocations (GNDs), they showed that dislocations distribution was heterogeneous for L-PBF IN625 and largely built up around the subgrain boundaries. Further, increasing the build plate temperature resulted in a decrease in the GND density due to a decrease in residual stresses. Leicht et al.

[239] showed that higher local misorientations can be seen when using a lower energy density in L-PBF. This was justified since a high energy density will result in higher heat input and annihilate dislocations in situ. Serrano-Munoz et al. [240] revealed that scanning strategies can significantly influence the residual stresses not only through the different amounts of thermal stresses they induce but also the change they cause in the grain morphology. Zhang et al. [145] revealed that the orientation that a IN718 part is printed in L-PBF results in a change in the average density of GNDs therefore contributing to an explanation in variation in mechanical properties dependent on print orientation.

The most recent development in EBSD of AM microstructures is the emergence of 3D EBSD. This technique is based on an automated serial sectioning of the samples inside an SEM using focused ion beam (FIB) milling coupled with EBSD data acquisition. This method has been used for example to understand columnar-to-equiaxed transition [241], map geometrically necessary dislocations [242], and study defect formation and microstructural inhomogeneities [38] in IN718, using a so-called tri-beam microscope developed at UC Santa Barbara by Prof. T. Pollock's group.

Transmission electron microscopy (TEM)

Transmission electron microscopy (TEM) characterizes internal structures of materials based on the transmission of electrons across a very thin (few nanometers) sample via a beam of high energy [243]. TEM plays an important role in the characterization of sub-micron size features in metallic materials and has been used in the characterization of phases, identification of elemental distribution, observing dislocation interactions, and measuring dislocation densities. As AM materials usually have a high density of imperfections like pores, standard electropolishing techniques for preparation of the required thin samples may be challenging. FIB milling can therefore be a better option though care needs to be taken to ensure no artefacts such as dislocations created by radiation damage are introduced [244].

There are two major imaging modes in TEM namely bright-field (BF) and dark-field (DF). BF imaging is the product of insertion and adjustment of an objective aperture in such a way that only the incident beam goes through while the diffracted beams are blocked. BF-TEM has been used extensively in characterizing AM Ni-based superalloys [99, 119, 125, 173, 179, 200, 213, 215]. Such examples include the identification of solidification structures in L-PBF Hastelloy X [213], the characterization of dislocation interaction with secondary precipitates in E-PBF Inconel 690 [245], the identification of subgrain cellular structures in L-PBF IN718 [102], and the characterization of secondary precipitate morphology and γ' in Haynes 282 [120]. A DF image, on the other hand, is produced by the objective aperture at the back focal plane of the objective lens selecting a diffracted beam. Examples of the use of DF-TEM in PBF is demonstrated in the imaging of Laves, γ' and γ'' phases formed in L-PBF and E-PBF printed IN718 [37, 94, 159]. BF- and DF-TEM for imaging and identifying nano-scale features in PBF Ni-based can be seen in Figs. 4, 12, and 15 which show sub-μm cell/dislocation boundaries, γ'/γ'', and carbides, respectively.

TEM provides further information regarding the phases and crystallographic structures via electron diffraction. The most common methods for this purpose are convergent-beam electron diffraction (CBED), selected area electron diffraction (SAED) and microdiffraction [246]. With the most common technique, i.e., SAED, the orientation relationship between a precipitate and the matrix, the coherency of the interfaces, and the crystal structure of individual phases can be determined. There are numerous examples of SAED being used in the characterization of PBF Ni-based superalloys (e.g., see Fig. 11). Within E-PBF IN718, it has been used not only in the confirmation of the existence of γ' and γ'' [37, 50], but also in identifying the orientation relationships between γ, γ', and γ'' [94, 159]. In studies of high γ' forming alloys, it has been used similarly for identifying the formation mechanism of γ' [116, 125, 247] and its orientation relationship with the γ matrix [125]. Further, SAED is often applied for the identification of secondary precipitates. Examples include the identification of μ in E-PBF CMSX-4 [108], Laves and δ in IN718 [50], and carbide formation in Haynes 282 (Fig. 15a) [117].

Scanning transmission electron microscopy (STEM) is a method very similar to TEM. In STEM, the lenses are adjusted to converge the electron beam into a focal point. The beam is then rastered across the sample as the transmitted signals are collected point-

by-point. STEM has been useful in identifying nano-scale microstructural features within AM Ni-based superalloys. For instance, STEM operating under high-angle annular dark-field (HAADF), offering enhanced contrast, showed dislocation interactions and strain fields with secondary precipitates and cell walls in numerous superalloys [44, 56, 248]. An example can be seen in Fig. 5d in the imaging of the dislocation substructure in E-PBF processed IN718. BF-STEM, on the other hand, has been used in numerous works to reveal the formation and morphology of needle like δ-phase, cuboidal γ', and disk and rod shape γ'' within Ni-based superalloys [146, 249].

As briefly discussed previously, just like SEM, TEM can be furnished with EDS, in which X-rays emitted in response to the electron bombardment are used to detect elements. For Ni-based superalloys under PBF processes, TEM-EDS is useful in the identification of nano-scale phases. For instance, in Fig. 7d TEM-EDS shows the elemental segregation between the γ matrix and γ' precipitates. Figures 16b–f and 15b use TEM-EDS in the identification of carbides and oxides within their IN718 and Haynes 282 alloys, respectively. Similarly, and not shown here, TEM-EDS has been used in the identification of TCP phases such as Laves in IN718 [98]. Lastly, analysis of the chemical composition at almost atomic scale can be done via TEM by an electron spectrometer that creates an energy-loss spectrum (i.e., EELS) [243]. EELS in TEM can be of great importance in characterizing AM microstructures when studying elements like O and other difficult to analyze species.

In situ electron microscopy

A recent advancement from which the AM field can significantly benefit is in situ microscopy. In situ microscopy refers to the live observation of microstructural evolution in a microscope e.g., a TEM or an SEM while material is subjected to stimuli of interest e.g., mechanical loading or thermal cycling [250]. AM materials are known to experience complicated mechanical/thermal hysteresis during printing, as outlined above. As the microstructural evolution occurs dynamically, even while the material is cooling to room temperature, post-mortem microscopy of the final microstructure will not always shed light on the sequence of evolution of microstructural events. In contrast, in situ examination of the microstructural evolution during heating/cooling cycles may help to unambiguously clarify this. In situ observation of microstructures was initially inspired by a constant development of new stages and capabilities in TEM. With the development of focused ion beam capabilities, however, there has been a significant boost in in situ microscopy via SEM in recent years [251–253].

For example, a SEM chamber equipped with a tensile testing stage can unveil real-time correlation between tensile properties and microstructural evolution. One example is the propagation of cracks with deformation [254]. Such study of a PBF sample can further clarify the role of structural imperfections such as pores and lack of fusion defects in part failure. In situ TEM analysis of foils under heating/cooling or stress/strain cycles is another example of how these advanced techniques can help in understanding the physical metallurgy of AM. One example is the capability of in situ TEM to image dislocation activities, precipitation evolution, and dislocation-precipitation interactions in response to thermal/mechanical hysteresis [255–258].

Transmission Kikuchi diffraction (TKD)

AM microstructures usually consist of fine sub-grains and a generally high density of dislocations that results from extremely high cooling rates inherent to AM. Such fine scale features may be challenging to study with standard EBSD, that at best can provide resolutions of 20–50 nm [259]. In addition to the spatial resolution, highly dislocated regions cause distortion in the diffraction patterns which deteriorates the indexing accuracy. These issues have paved the way toward development of a technique named transmission Kikuchi diffraction (TKD) [260]. This method uses an EBSD detector in an SEM chamber to collect Kikuchi patterns from underneath an electron-transparent sample (e.g., a typical TEM sample) subjected to the electron beam. The replacements of back-scattering with forward scattering brings about significant improvement in the resolution (i.e., $\sim$ 2 nm). As TKD does not need tilt correction or dynamic focus, it also maximizes the indexing rate. Examples of applications of TKD are shown in a few studies where they reveal dislocations, grain boundaries, and subgrain boundaries in L-PBF AM Ni-based superalloys [261, 262]. Another study involving L-PBF IN718 has also applied the technique in the

identification of phase through the use of diffraction patterns revealed by TKD showing the presence of the FCC matrix and sub-μm Nb-carbides [72].

Atom probe microscopy (APM)

APM is a three-dimensional characterization technique with sub-nanometer resolution that allows identification of the position and the elemental nature of individual atoms [263]. APM is a destructive analysis that requires the use of needle shaped samples with sharp shank angles (< 20°) and curvature radii of ~ 50 nm at the tip apex [264] that are created through a multi-step electropolishing for bulk materials, or focused ion beam milling for site-specific investigations [265–267]. The sample is inserted in a cryogenically cooled (< 80 K) ultra-high vacuum (< 10^{-10} torr) chamber, where the tip is aligned in front of the aperture of the straight-flight-path local electrode.

The destructive process of ionization and desorption of atoms from the apex of an atom probe tip, generated by intense electric fields, is a phenomenon known as field evaporation. The ionized atoms are accelerated away from the surface through the electrode toward a position sensitive detector. Since evaporation only occurs during a few hundreds of picoseconds from each pulse, and the distance from tip to detector is known, the time-of-flight of the ions between the evaporation and detector hit events can be determined. This parameter is used to identify the chemical nature of each type of ion on mass spectrum histograms [268]. The sequentially evaporated and detected ions constitute a three-dimensional dataset that is reconstructed as a magnified image projection of the tip, as for example shown in Fig. 13.

The use of APM in AM has provided significant advances in the field of quantitative investigations of nanoscale phases, atomic ordering, and clustering [80, 119, 269]. Regions with local segregation of elements such as precipitates in Ni-based superalloys can be enveloped by chemical isoconcentration surfaces according to a determined compositional threshold. From these objects, quantitative data regarding their morphology and configuration, size, volume fraction, chemical composition, number density, and interface location can be extracted [269]. For instance, imaging nanoscale γ' and γ'' is a challenging task to be achieved via other characterization techniques due to the small sizes of these particles. APM provides sub-nanometer resolution required to differentiate these phases based on their morphology and chemical composition. In E-PBF IN718, the occurrence of the coprecipitate γ'/γ'' sandwich structure, as seen in Fig. 13, is not easily identifiable without APM. The study of the chemical profile at interphase and grain boundaries in AM Ni-based superalloy has benefited from APM, where chemical concentration across regions of interest can be identified, enabling findings related to element segregation on interphase, grain, melt pool, and cell boundaries [44, 149, 210, 270]. These have included the identification of Nb segregation to the grain boundary in IN718 [165] and the identification of Nb segregation to the interdendritic region and its role in the formation of Laves phase [179], the reporting of segregation of Zr, B, C, Mo, and Si to the grain boundaries in IN738LC [271], the partitioning behavior of elements between γ and γ' in a primarily γ' forming Ni-based superalloy [131], and the analysis of the interface between γ' and borides in a non-weldable Ni-based superalloy [123], just to name a few. In addition to phase analysis, the near atomic resolution of APM also enables atomic clustering studies [223] where numerous tools have also been developed for statistically significant quantification of clusters [272, 273].

X-ray and neutron diffraction

X-ray diffraction techniques are commonly used in AM investigations to qualify and/or quantify phases, and determine their crystal structure, lattice parameters, residual stresses, and crystallographic texture. An X-ray diffraction pattern is generated once constructive interference occurs in a range of scattered angles between the incident rays and the crystal structure, where the Bragg's law is satisfied. The resulting diffraction peaks in the diffractogram are analyzed in regard to their position, which determines the size and shape of the unit cell, their intensity, related to the position of the atoms within the cell, and their width [274]. Standard XRD can be obtained with laboratory-based diffractometers. Many studies have used crystallographic information gained from XRD to confirm PBF's tendency to form textures oriented in the build direction [97, 159, 163, 226, 275]. It can also be used to compare the impact of the processing technique on the resulting texture as shown in a study by Amato et al. [161]. They reported

that in IN625 different textures may be formed dependent on the use of E-PBF and L-PBF. Identification of the lattice parameter through XRD, on the other hand, has been used with Ni-based superalloys to assess residual stress and elemental partitioning in alloys [56, 57]. For example, it has been reported in L-PBF IN625 that high amounts of Nb and Mo may be in solution with the γ matrix due to the high lattice parameter reported [56, 57]. Lastly, XRD can also be used for phase identification of γ and γ'/γ'' with some limitations [163, 191, 208].

Despite the information that can be gained from laboratory-based XRD, the technique has limitations that should be discussed. The crystallographic information gained is only qualitative and pole figures cannot be generated. Residual stress measurements can only be taken at the surface of the sample due to the limitations in penetration depth of laboratory X-rays. When studying phase identification results, it has to be taken into account that they are only quantitative, with resolution limitations in the technique making certain phases difficult to identify. For instance, in Ni-based superalloys such as IN718 which contain multiple phases, overlapping diffraction peaks jeopardize their accurate identification [163, 191, 208]. Overall, a large number of studies have noted the overlap of the γ, γ', and γ'' peaks making it difficult to identify these phases [56, 161, 163, 207, 276]. Furthermore, many studies have identified other precipitated phases such as carbides like those in Fig. 15 through to Fig. 17 in SEM and TEM that are missed by laboratory-based diffractometers due to their small size and low quantity. It should be noted, however, that a few studies have managed to report other phases outside the γ matrix using laboratory-based diffractometers, pointing toward the potential process and material dependent nature of characterizing AM samples. For instance, in L-PBF CM247LC, the presence of (Ta,Ti)–carbides were detected through XRD [116]. In E-PBF IN718, MX carbides were also detected through XRD. The detection of these phases may be due to larger quantities and larger sizes of these secondary precipitates. To overcome these limitations, synchrotron or neutron sources are needed dependent on the information one wishes to gather.

For higher resolution or in situ experiments, synchrotron sources of radiation are more appropriate. These facilities, in a simplistic explanation, generate electromagnetic radiation by diverting the path of an electron beam accelerated close to the speed of light in a storage ring [277]. The resulting monochromatic or pink/polychromatic X-ray beam is then used for characterization methods such as X-ray imaging, diffraction, or scattering [278]. For diffraction, the interaction between the sample and X-rays is similar to that of laboratory-based XRD, however, higher energy X-rays permit deeper penetration of the sample and greater resolution in the resulting spectrum, enabling the resolution of the individual γ, γ', and γ'' peaks and quantitative phase fraction analysis. Under SAXS, the X-ray beam is transmitted through the sample, generating an angle of scattering typically lower than 0.1° [279]. This provides higher resolution, enabling proper quantification of nanoscale defects and particles [280, 281]. There has currently been limited use of synchrotron sources in metal AM research on Ni-based superalloys. The limited number of publications can be partially attributed to the difficulty in accessing these resources which usually requires the submission and approval of a scientific proposal before these tools can be accessed. A few works have used synchrotron X-ray diffraction in PBF Ni-based superalloys [164, 182, 282]. For instance, Sarley et al. [182] used synchrotron diffraction measurements to detect δ, γ, and γ' in L-PBF IN718. In the same study, the synchrotron measurements also revealed more pronounced δ formation in a sample taken at the center of the build when compared to a sample at the bottom of the build. The use of wide angle, small angle, and ultra-small angle X-ray scattering (WAXS, SAXS, and USAXS) has the unique ability to study the precipitation evolution in situ in AM, however, only few works have utilized these characterization techniques to date. There are currently studies available on the in situ development of precipitation during heat treatment [282, 283], the precipitation of γ' in CMSX-4 processed under simulated E-PBF [284], and precipitation of γ' in CMSX-4 under L-PBF [285].

Similar to synchrotron radiation, neutron diffraction offers superior capabilities in comparison to laboratory-based X-ray diffraction techniques, where generally only a few tens of microns below the sample surface can be probed. Neutron interaction occurs mainly with the atomic nucleus, whereas X-rays are scattered by electrons [280]. Neutron diffraction uses Bragg's law to disclose measurements used for studies of residual stress, texture, lattice parameters, and phase analyses [286–290].

Measurement of residual stresses, common in E-PBF and L-PBF materials, and measurement of deformation behavior are the most common applications due to sample penetration on the order of centimeters (maximum of 2 cm for Ni [291]) allowing the strain measurement in a number of directions in the bulk of the material [76, 164, 292–295]. Only one known study has used neutrons for phase fraction analysis prior to heat treatment in PBF Ni alloys [181]. In this work, the authors used the Rietveld analysis to fit the neutron diffraction histograms of IN718 processed via L-PBF, to determine the presence of 6.5% of γ', 8.4% of γ'', δ and MC-carbides.

Case study (multi-scale characterization of PBF processed IN738 alloy)

To showcase how microscopy can shed light on the multiscale hierarchical microstructure of AM Ni-based superalloys, Fig. 20 illustrates the resulting images obtained from several of the aforementioned characterization techniques applied to an AM IN738 alloy. Figure 20a, b shows printed parts of an

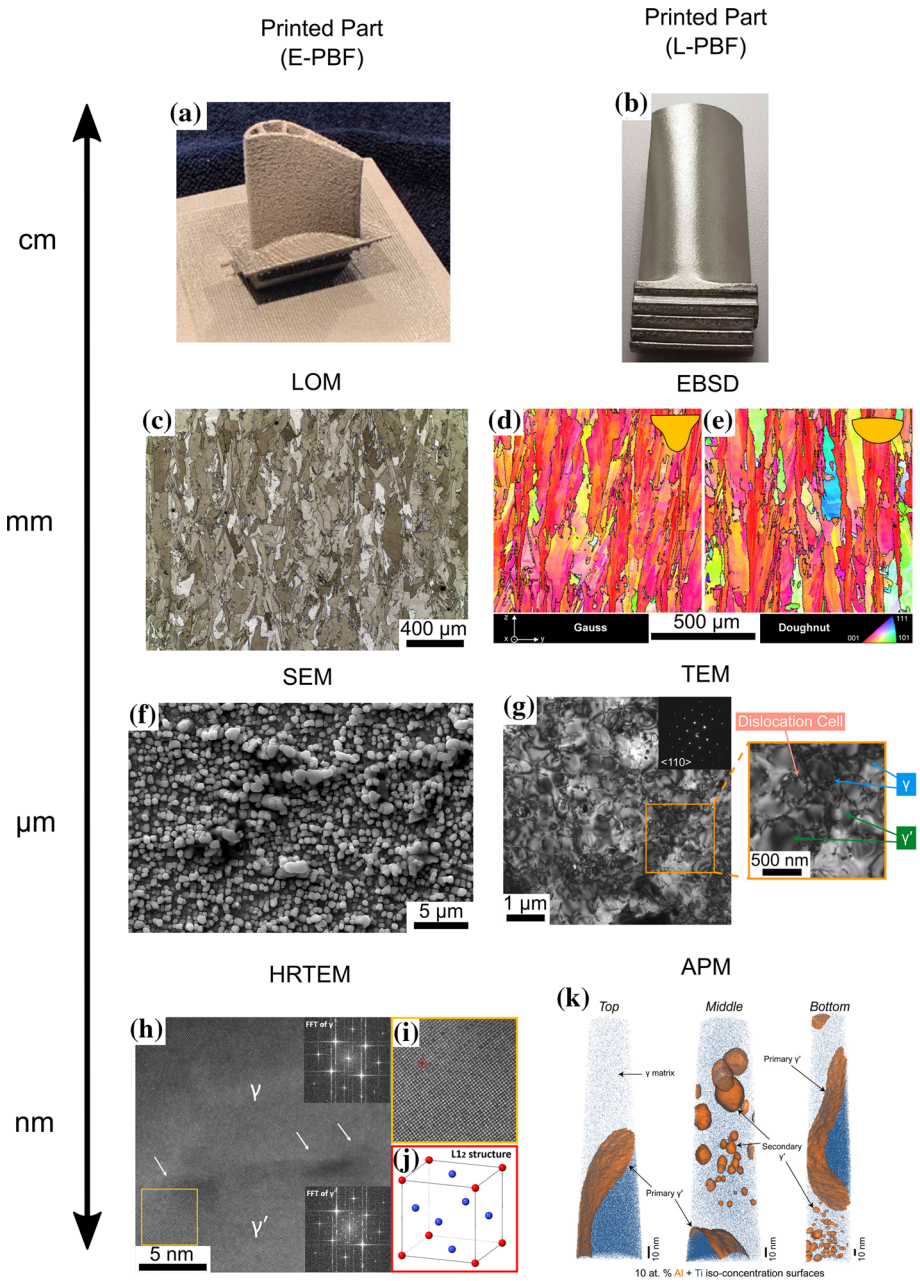

Figure 20 Examples of blade-like parts printed by **a** E-PBF and **b** L-PBF; **c** LOM image showing columnar grain structure in E-PBF IN738; EBSD maps showing grain orientation of L-PBF IN738 samples printed using a **d** Gauss shaped laser and **e** doughnut shaped laser. **f** SEM micrograph of γ' precipitates in deep-etched E-PBF IN738; **g** TEM micrographs of E-PBF IN738 in <110> zone axis and with magnified region showing dislocation cells and γ' precipitates in detail. **h** HRTEM of matrix region showing γ' precipitates in E-PBF IN738 with higher magnification of selected area in **i** and crystal structure of γ' in (**j**). **k** APM reconstructions of γ matrix region containing primary and secondary containing γ' precipitates on top, middle, and bottom regions in E-PBF IN738. a and b adapted from [296]; c and f image courtesy of Nima Haghdadi and Sophie Primig (UNSW Sydney); d and e from [271]; g and k from [119]; **h**, **i**, and **j** image courtesy of Zibin Chen and Bryan Lim (University of Sydney), with permission.

aeroengine turbine blade, where the former was manufactured via E-PBF and the latter via L-PBF. Light optical microscopy (LOM) (Fig. 20c) reveals melt-pool boundaries, a feature that usually cannot easily be resolved using any of the other more sophisticated imaging techniques. EBSD (Fig. 20d, e) is a complementary technique used to image the grain structure of AM materials. Only through using EBSD, the orientation of the grains and the micro-texture of the material can be determined. For example, while the elongated nature of γ grains was seen in LOM images too, only EBSD can show the crystallographic orientation of individual grains along the Z-direction as a function of scanning strategy, as reported in [195]. EBSD can also reveal the misorientation between grains, an important parameter in determining the cracking susceptibility of Ni-based superalloys. Despite these opportunities, EBSD cannot resolve γ from γ'. This is mainly due to very similar lattice structures of these two phases in many Ni-based superalloys.

Figure 20f shows an SEM image of γ' precipitates after deep etching. Such SEM imaging can provide valuable insights into the size, morphology and distribution of γ'. For example, using SEM, it has been shown that an E-PBF process with a random scanning strategy can develop a bimodal distributions of γ' particles in the mid height of IN738 alloy [127]. SEM, however, has a limit in terms of size. To image fine features of few nm in the microstructure, TEM is required. TEM enables higher magnification and better resolution of micro—to nanoscale features such as dislocation cells illustrated in Fig. 20g. The character of transmission of electrons allows the investigation of the arrangement of columns of atoms via high resolution transmission electron microscopy (HRTEM), as well as the crystallographic relationship between γ and γ' via fast Fourier transform (FFT) as shown in the inset in Fig. 20h. TEM has been used to study the dislocation densities within γ and γ' in IN738 [119].

APM is another powerful characterization tool particularly for the cases when a thorough analysis of size, morphology and chemistry of nanometric features (such as γ') is required. In a study by some of the current authors [119] for example (Fig. 20k), APM has shown the bimodal size of γ' at the bottom and middle of an E-PBF IN738, while such bimodality was not detected at the top regions. Moreover, APM analysis revealed that the Ni, Al, Ti, Cr and Co content is different not only within the primary and secondary γ' but also within each of these types of precipitates across the build height. APM also revealed that W segregates at the γ/γ' interface. Such detailed correlative analysis of size, morphology, distribution, and chemistry of γ' and the interfacial segregation of alloying elements can only be achieved via APM.

Finally, as an overview, the advantages, disadvantages, ease of sample preparation and ease of operation of each of the technique discussed in this section are summarized in Table 5.

Summary and concluding remarks

This review highlights hierarchical nature of the microstructure evolution during PBF printing of Ni-based superalloys and introduces suitable characterization methods from the part to the atomic scale. A review of the detailed processing-structure–property relationships is given. The information presented within this review can be used as a roadmap for future research aimed at developing new AM processes for current and future Ni-based superalloys. The main conclusions from the existing literature on phases in Ni-based superalloys processed by PBF can be summarized as follows:

γ matrix phase

- The microstructural evolution during solidification most often involves the epitaxial growth of grains in the build direction. However, changes in the processing parameters and sample geometry can influence the formation of grains to appear in equiaxed or even mixed structures.
- For L-PBF Ni-based superalloys, the γ matrix is most often composed of a cellular dendritic structure which ranges in size dependent on solidification conditions. These dislocation structures are usually in the order of two magnitudes smaller than in traditional cast Ni-based superalloys. The substructure is composed of cellular networks of dislocations due to thermal cycling resulting in a large buildup of residual stresses generated by constrained material around the melt pool.
- For E-PBF Ni-based superalloys, the γ matrix can be divided into three distinct regions due to the

Table 5 Summarized uses and limitations of individual characterization techniques

Characterization technique	Main uses	Sample preparation complexity	Microscope operation complexity	Limitation
LOM	Macroscopic examination of pores, melt pools, grains, and coarse secondary phases	Low	Low	Limited magnification and resolution, no chemical and crystallographic analysis
SEM/BSE/EDS	General microscopic examination of microstructure, with possibility of detection of local enrichment of elements	Low	Medium	Chemical analysis of regions smaller than 1 μm not feasible, no crystallographic analysis
X-ray diffraction	Quantification of phases, crystal structure, and lattice parameters, residual stresses, and crystallographic texture	Low	Medium	Overlapping diffraction peaks might jeopardize proper investigation of present phases, no visual inspection or local investigation of the microstructure
Neutron diffraction	Residual stress analysis, phase fractions, grain orientation	Medium	High	No visual inspection or local investigation of the microstructure
EBSD	Investigation of phase, grain orientation, density of dislocations, interface character, and texture	Medium	Medium	Time consuming, Possible low indexing accuracy of highly dislocated regions, distinction of coherent phases such as γ' impossible
TEM/EDS	Characterization of phases, identification of elemental distribution, dislocation interactions, and measuring dislocation densities	High	High	Highly local, challenging distinction of coherent phases such as γ', challenging chemical quantification of materials containing low atomic number elements
In situ TEM	Analysis of microstructural evolution during heating/cooling or stress/strain cycles	High	Very High	Requires sophisticated tools, mechanical testing at low loads can be subjected to multiple sources of disturbances and inaccuracies
TKD	Crystallography and phase analysis of electron-transparent samples	High	High	Samples can be contaminated with C deposited during electron scanning
APM	Three-dimensional investigation of precipitates, grain and melt pool boundary segregation, and clusters of atoms	High	High	Limited field of view, and volume of material analyzed might not be representative of different nanostructures in heterogeneous samples

high temperature of the preheat. At the top of the build a clear dendritic structure exists, however, moving down the build the microstructure begins to homogenize. After a set distance that is process and material dependent, the microstructure reaches a steady-state condition. Dislocations are often reported to build up around obstacles, creating complex dislocation structures.

γ' phase

- The γ' phase is an intermetallic phase desirable to enhance the strength of Ni-based superalloys. The chemistry is primarily $Ni_3(Al,Ti)$, however, in certain cases Ta can play a similar role to Al and Ti. Generally, the size, shape, and composition of γ' will be dependent on both the cooling rate upon solidification, cooling from the γ' solvus, and the presence of associated alloying elements.
- Processing of high γ' Ni-based superalloys through L-PBF is highly sensitive to its detailed parameters and the chosen alloy, with certain studies showing the formation of γ' occurring under L-PBF and other studies showing the suppression of γ'. The variation in the nucleation of γ' is attributed to its sensitivity to cooling rate and accompanying alloy dependent kinetics of γ' formation.

- High γ' Ni-based alloys processed by E-PBF show a wide range of size and morphology of γ' due to greater control of cooling rates and the high preheat conditions. If the preheat temperature is close to the γ' solvus, then a gradient is seen where larger aged γ' is found toward the bottom of the build compared to smaller γ' toward the top. At temperatures above the γ' solvus, however, it is possible to form a more homogeneous distribution of γ'.
- The morphology of γ' shows heterogeneity between the dendrite and interdendritic regions depending on the alloy, with the interdendritic regions associated with a primary γ' of cuboidal morphology and the dendritic cores associated with a secondary γ' of spherical morphology. This heterogeneity is attributed to different phase transformation paths for the primary and secondary γ'.

γ'' phase

- γ'' is the main strengthening phase within IN718, and is a meta-stable body centered tetragonal ($D0_{22}$) phase (Ni_3Nb) that is stable up to 650 °C.
- In alloys processed by L-PBF, there is debate over the precipitation of γ'' with various studies reporting no γ'' formation while other studies provide evidence of its precipitation. Of those that do report γ'', variation exists in the reported size and morphology. A likely reason for the variation in γ'' is the variation in processing parameters and part geometry impacting the resulting thermal conditions of the given samples.
- In E-PBF, considerable differences in the size and morphology are noted to occur along the build height due to ageing of the γ'' at lower build heights caused by high preheat temperatures that coarsen the phase.
- Within E-PBF, the coprecipitation of γ'/γ'' "sandwich"-like structures is noted to occur in IN718. Further, Laves phase has been noted to deplete Nb from the matrix, suppressing the nucleation and growth of γ''.

δ phase

- δ phase often forms from metastable γ'' when IN718 spends extended periods of time at elevated temperatures between $\sim$ 650 and $\sim$ 1000 °C. When δ forms, it has often been reported to exhibit a needle or platelet like morphology.
- Many studies report no formation of δ in IN178 during L-PBF. The lack of precipitation is largely attributed to the high cooling rate leaving IN718 parts in an unaged condition, and the formation of Laves phase which decreases Nb content in the matrix for δ precipitation.
- For alloys processed by E-PBF, the size and morphology of δ is dependent on the preheat temperature. If the preheat temperature is within the range for the precipitation of δ, then the size and morphology become dependent on the build height. Morphologies of δ have been reported to be zipper- or globular- like at the top or the bottom of the build, respectively. Processing IN718 with a preheat above 1000 °C was noted to largely suppress the formation of δ outside of the inter-granular regions.

Carbide, oxide, nitride, and boride phases

- Of the reviewed literature, studies on most alloys only report MC carbides, with the exception of Haynes 282, Hastelloy X, and IN738. Studies on Haynes 282 report the formation of MC and $M_{23}C_6$ carbides. Investigations on Hastelloy X report M_xC_y, M_6C, $M_{12}C$, and $M_{23}C_6$ carbides, and those on IN738 report the formation of MC and $M_{23}C_6$ carbides. The prominence of MC carbides is associated with its fast kinetics during solidification.
- The elemental composition of carbides is dependent on alloy composition, and carbides are primarily composed of elements that strongly segregate to the interdendritic regions.
- The size and morphology of carbides are dependent on solidification conditions and can range from spherical to "script"-like morphology during faster or slower solidification conditions, respectively.
- In L-PBF, carbides are more likely to be spherical in morphology and smaller due to the faster solidification conditions. In E-PBF, however, carbides are larger and often form large chains following the build direction.

- Dependent on the number of contaminants, a limited number of studies have shown that the formation of nitrides, oxides and borides is possible. Nitrides were noted to form in IN718 as the core structure from which carbides nucleate. In IN718, spherical borides have been noted to form, while in IN718 and CM247LC formation of spherical oxides was reported.

TCP phases

- Due to the high cooling rates associated with PBF processes, only Laves and μ have been reported to form within Ni-based superalloys. The Laves phase has an AB_2 HCP structure primarily composed of Nb and Mo, and therefore, only occurs in alloys with a sufficiently high content of Nb or Mo. μ phase is a rhombohedral phase that occurs in alloys with high elemental contents of W and Mo.
- In L-PBF, Laves has been reported to form with an irregularly shaped eutectic morphology, as either γ + Laves or divorced form, which can coexist with carbides and can be located within the interdendritic regions or grain boundaries.
- In E-PBF, Laves size and morphology are dependent on the build height due to the in situ heat treatment that occurs due to the high preheat temperatures. Laves is primarily only present in the top layers of the build and has morphologies ranging from spherical to "script"-like. With decreasing build height, Nb diffusion results in Laves dissolution.
- Within E-PBF CMSX-4, μ phase has been reported with an elongated spherical geometry. So far, there is only one case in the reviewed literature where a TCP phase other than the Laves phase forms in the as-built condition.

Amongst the discussed literature, there have been some noted inconsistencies in reported phase size and morphology that can likely be attributed to the complex nature of AM. These include differences in reported carbide formation such as seen in L-PBF Hastelloy X, differences in reported size and morphology of γ' in E-PBF CMSX-4, and differences in the reported occurrence of nucleation of δ within L-PBF IN718, just to name a few. Further, outside noted inconsistencies, there are currently some gaps in knowledge in correlating scan strategy, process parameters, and geometry to phase fraction, morphology, and distribution. For example, the extent to which the γ' and γ'' phases distribution, fraction, and morphology could be manipulated using either E-PBF or L-PBF is yet to be fully understood. In the characterization of these microstructures from macro- to nanoscale, the associated variations in thermal conditions due to differences in processing parameters or differences in sample geometry need to be considered in tandem. As shown in our case study on IN738, the multiscale hierarchical microstructure evolution during PBF printing of Ni-based superalloys, resulting from spatial and temporal variations in the thermal conditions, is best resolved using a variety of correlative microscopy methods.

AM Ni-based superalloys will continue to play a significant role in many important industries such as defense, energy, and aerospace due to the design freedoms permitted. With the perspective of site-specific control of microstructure already realized through an understanding of the relation between grain structure and process parameters, future work should focus on developing further understanding of the relationship between phase, processing parameters, and geometry. Only then will the full design freedom of engineered AM components be realized. A thorough understanding of the microstructure using different characterization techniques remains the Rosetta stone for unveiling process-property relationships. Microstructural characterization methods continue to play a key role in the development of advanced alloys and processing methods in a traditional manufacturing context. Similarly, it will enable re-inventing the physical metallurgy for metals additive manufacturing.

Acknowledgements

Funding from the AUSMURI program administered by the Australia's Department of Industry, Science, Energy and Resources is acknowledged. The authors acknowledge the facilities, as well as the scientific and technical staff support of the Electron Microscope Unit (EMU) at UNSW Sydney (part of the Mark Wainwright Centre) and Sydney Microscopy & Microanalysis (SMM) at the University of Sydney (a core research facility). Both the EMU and SMM are nodes of Microscopy Australia. S. Primig is supported by the UNSW Scientia Fellowship scheme.

Funding

Open Access funding enabled and organized by CAUL and its Member Institutions.

Data availability

Where from our own research, data can be made available upon request.

Declarations

Conflict of interest The authors declare that there are no conflicts of interest.

References

[1] Berman B (2012) 3-D printing: the new industrial revolution. Bus Horiz 55:155–162. https://doi.org/10.1016/j.bushor.2011.11.003

[2] Gibson I, Rosen DW, Stucker B (2010) Additive manufacturing technologies. Springer, Boston. https://doi.org/10.1007/978-1-4419-1120-9

[3] Wang YM, Voisin T, McKeown JT, Ye J, Calta NP, Li Z, Zeng Z, Zhang Y, Chen W, Roehling TT, Ott RT, Santala MK, Depond PJ, Matthews MJ, Hamza AV, Zhu T (2018) Additively manufactured hierarchical stainless steels with high strength and ductility. Nat Mater 17:63–70. https://doi.org/10.1038/NMAT5021

[4] Herzog D, Seyda V, Wycisk E, Emmelmann C (2016) Additive manufacturing of metals. Acta Mater 117:371–392. https://doi.org/10.1016/j.actamat.2016.07.019

[5] Sing SL, Yeong WY (2020) Laser powder bed fusion for metal additive manufacturing: perspectives on recent developments. Virtual Phys Prototyp 15:359–370. https://doi.org/10.1080/17452759.2020.1779999

[6] Graybill B, Malawey D, Martinez-franco E (2018) Additive Manufacturing of Nickel-Based Superalloys. In: Proceedings of the ASME 2018 13th international manufacturing science and engineering conference (pp 1–17)

[7] Wang X, Gong X, Chou K (2017) Review on powder-bed laser additive manufacturing of Inconel 718 parts. Proc Inst Mech Eng Part B J Eng Manuf 231:1890–1903. https://doi.org/10.1177/0954405415619883

[8] Choudhury IA, El-Baradie MA (1998) Machinability of nickel-base super alloys: a general review. J Mater Process Technol 300:278–284. https://doi.org/10.1016/s0924-0136(97)00429-9

[9] Sames WJ, List FA, Pannala S, Dehoff RR, Babu SS (2016) The metallurgy and processing science of metal additive manufacturing. Int Mater Rev 61:315–360. https://doi.org/10.1080/09506608.2015.1116649

[10] Lewandowski JJ, Seifi M (2016) Metal additive manufacturing: a review of mechanical properties. Annu Rev Mater Res 46:151–186. https://doi.org/10.1146/annurev-matsci-070115-032024

[11] Yap CY, Chua CK, Dong ZL, Liu ZH, Zhang DQ, Loh LE, Sing SL (2015) Review of selective laser melting: materials and applications. Appl Phys Rev 2:041101. https://doi.org/10.1063/1.4935926

[12] Everton SK, Hirsch M, Stavroulakis PI, Leach RK, Clare AT (2016) Review of in-situ process monitoring and in-situ metrology for metal additive manufacturing. Mater Des 95:431–445. https://doi.org/10.1016/j.matdes.2016.01.099

[13] Körner C (2016) Additive manufacturing of metallic components by selective electron beam melting-a review. Int Mater Rev 61:361–377. https://doi.org/10.1080/09506608.2016.1176289

[14] Zhang Y, Wu L, Guo X, Kane S, Deng Y, Jung YG, Lee JH, Zhang J (2018) Additive manufacturing of metallic materials: a review. J Mater Eng Perform 27:1–13. https://doi.org/10.1007/s11665-017-2747-y

[15] Gu DD, Meiners W, Wissenbach K, Poprawe R (2012) Laser additive manufacturing of metallic components: materials, processes and mechanisms. Int Mater Rev 57:133–164. https://doi.org/10.1179/1743280411Y.0000000014

[16] Haghdadi N, Laleh M, Moyle M, Primig S (2021) Additive manufacturing of steels: a review of achievements and

challenges. J Mater Sci 56:64–107. https://doi.org/10.1007/s10853-020-05109-0

[17] DebRoy T, Wei HL, Zuback JS, Mukherjee T, Elmer JW, Milewski JO, Beese AM, Wilson-Heid A, De A, Zhang W (2018) Additive manufacturing of metallic components–process, structure and properties. Prog Mater Sci 92:112–224. https://doi.org/10.1016/j.pmatsci.2017.10.001

[18] Rahman MS, Schilling PJ, Herrington PD, Chakravarty UK (2021) A comparison of the thermo-fluid properties of Ti-6Al-4V melt pools formed by laser and electron-beam powder-bed fusion processes. J Eng Mater Technol Trans ASME 143:1–13. https://doi.org/10.1115/1.4048371

[19] Wu B, Pan Z, Ding D, Cuiuri D, Li H, Xu J, Norrish J (2018) A review of the wire arc additive manufacturing of metals: properties, defects and quality improvement. J Manuf Process 35:127–139. https://doi.org/10.1016/j.jmapro.2018.08.001

[20] Greer C, Nycz A, Noakes M, Richardson B, Post B, Kurfess T, Love L (2019) Introduction to the design rules for metal big area additive manufacturing. Addit Manuf 27:159–166. https://doi.org/10.1016/j.addma.2019.02.016

[21] Nycz A, Lee Y, Noakes M, Ankit D, Masuo C, Simunovic S, Bunn J, Love L, Oancea V, Payzant A, Fancher CM (2021) Effective residual stress prediction validated with neutron diffraction method for metal large-scale additive manufacturing. Mater Des 205:109751. https://doi.org/10.1016/j.matdes.2021.109751

[22] Shassere B, Nycz A, Noakes MW, Masuo C, Sridharan N (2019) Correlation of microstructure and mechanical properties of metal big area additive manufacturing. Appl Sci 9:787. https://doi.org/10.3390/app9040787

[23] Singamneni S, Yifan LV, Hewitt A, Chalk R, Thomas W, Jordison D (2019) Additive manufacturing for the aircraft industry: a review. J Aeronaut Aerosp Eng 08:1–13. https://doi.org/10.35248/2168-9792.19.8.215

[24] Gäumann M, Bezençon C, Canalis P, Kurz W (2001) Single-crystal laser deposition of superalloys: processing–microstructure maps. Acta Mater 49:1051–1062. https://doi.org/10.1016/S1359-6454(00)00367-0

[25] Tian Y, McAllister D, Colijn H, Mills M, Farson D, Nordin M, Babu S (2014) Rationalization of microstructure heterogeneity in INCONEL 718 builds made by the direct laser additive manufacturing process. Metall Mater Trans A Phys Metall Mater Sci 45:4470–4483. https://doi.org/10.1007/s11661-014-2370-6

[26] Colomo AG, Wood D, Martina F, Williams SW (2020) A comparison framework to support the selection of the best additive manufacturing process for specific aerospace applications. Int J Rapid Manuf 9:194. https://doi.org/10.1504/ijrapidm.2020.107736

[27] Smith RJ, Lewis GJ, Yates DH (2001) Development and application of nickel alloys in aerospace engineering. Aircr Eng Aerosp Technol 73:138–146. https://doi.org/10.1108/00022660110694995

[28] Pollock TM, Tin S (2006) Nickel-based superalloys for advanced turbine engines: chemistry, microstructure and properties. J Propuls Power 22:361–374. https://doi.org/10.2514/1.18239

[29] Abrantes I, Ferreira AF, Silva A, Costa M (2021) Sustainable aviation fuels and imminent technologies-CO_2 emissions evolution towards 2050. J Clean Prod 313:127937. https://doi.org/10.1016/j.jclepro.2021.127937

[30] Blakey-Milner B, Gradl P, Snedden G, Brooks M, Pitot J, Lopez E, Leary M, Berto F, du Plessis A (2021) Metal additive manufacturing in aerospace: a review. Mater Des 209:110008. https://doi.org/10.1016/j.matdes.2021.110008

[31] Sanchez S, Smith P, Xu Z, Gaspard G, Hyde CJ, Wits WW, Ashcroft IA, Chen H, Clare AT (2021) Powder bed fusion of nickel-based superalloys: a review. Int J Mach Tools Manuf 165:103729. https://doi.org/10.1016/j.ijmachtools.2021.103729

[32] Adegoke O, Andersson J, Brodin H, Pederson R (2020) Review of laser powder bed fusion of gamma-prime-strengthened nickel-based superalloys. Metals (Basel) 10:1–26. https://doi.org/10.3390/met10080996

[33] Hosseini E, Popovich VA (2019) A review of mechanical properties of additively manufactured Inconel 718. Addit Manuf 30:100877. https://doi.org/10.1016/j.addma.2019.100877

[34] Tian Z, Zhang C, Wang D, Liu W, Fang X, Wellmann D, Zhao Y, Tian Y (2019) A review on laser powder bed fusion of Inconel 625 nickel-based alloy. Appl Sci 10:81. https://doi.org/10.3390/app10010081

[35] a. Bauereiß, T. Scharowsky, C. Körner, (2014) Defect generation and propagation mechanism during additive manufacturing by selective beam melting. J Mater Process Technol 214:2497–2504. https://doi.org/10.1016/j.jmatprotec.2014.05.002

[36] Zhang B, Li Y, Bai Q (2017) Defect formation mechanisms in selective laser melting: a review. Chinese J Mech Eng (Engl Edn) 30:515–527. https://doi.org/10.1007/s10033-017-0121-5

[37] Lee HJ, Kim HK, Hong HU, Lee BS (2019) Influence of the focus offset on the defects, microstructure, and mechanical properties of an Inconel 718 superalloy fabricated by electron beam additive manufacturing. J Alloys Compd 781:842–856. https://doi.org/10.1016/j.jallcom.2018.12.070

[38] Polonsky AT, Echlin MP, Lenthe WC, Dehoff RR, Kirka MM, Pollock TM (2018) Defects and 3D structural

inhomogeneity in electron beam additively manufactured Inconel 718. Mater Charact 143:171–181. https://doi.org/10.1016/j.matchar.2018.02.020

[39] Reed RC (2007) The Superalloys. https://doi.org/10.1016/S1369-7021(07)70022-6

[40] Jena AK, Chaturvedi MC (1984) The role of alloying elements in the design of nickel-base superalloys. J Mater Sci 19:3121–3139. https://doi.org/10.1007/BF00549796

[41] Shaikh AS, Schulz F, Minet-Lallemand K, Hryha E (2021) Microstructure and mechanical properties of Haynes 282 superalloy produced by laser powder bed fusion. Mater Today Commun 26:102038. https://doi.org/10.1016/j.mtcomm.2021.102038

[42] Atabay SE, Sanchez-Mata O, Muñiz-Lerma JA, Gauvin R, Brochu M (2020) Microstructure and mechanical properties of rene 41 alloy manufactured by laser powder bed fusion. Mater Sci Eng A 773:138849. https://doi.org/10.1016/j.msea.2019.138849

[43] Muñiz-Lerma JA, Tian Y, Wang X, Gauvin R, Brochu M (2019) Microstructure evolution of Inconel 738 fabricated by pulsed laser powder bed fusion. Prog Addit Manuf 4:97–107. https://doi.org/10.1007/s40964-018-0062-2

[44] De Luca A, Kenel C, Griffiths S, Joglekar SS, Leinenbach C, Dunand DC (2021) Microstructure and defects in a Ni-Cr-Al-Ti γ/γ' model superalloy processed by laser powder bed fusion. Mater Des 201:109531. https://doi.org/10.1016/j.matdes.2021.109531

[45] Körner C, Ramsperger M, Meid C, Bürger D, Wollgramm P, Bartsch M, Eggeler G (2018) Microstructure and mechanical properties of CMSX-4 single crystals prepared by additive manufacturing. Metall Mater Trans A Phys Metall Mater Sci 49:3781–3792. https://doi.org/10.1007/s11661-018-4762-5

[46] Bürger D, Parsa AB, Ramsperger M, Körner C, Eggeler G (2019) Creep properties of single crystal Ni-base superalloys (SX): a comparison between conventionally cast and additive manufactured CMSX-4 materials. Mater Sci Eng A 762:138098. https://doi.org/10.1016/j.msea.2019.138098

[47] Davis JR (2000) Nickel, cobalt, and their alloys. ASM International, Materials Park. https://doi.org/10.1361/ncta2000p003

[48] M.J. Donachie, S.J. Donachie, Super alloys A Technical Guide, 2002.

[49] Yeh AC, Tin S (2006) Effects of Ru on the high-temperature phase stability of Ni-base single-crystal superalloys. Metall Mater Trans A Phys Metall Mater Sci 37:2621–2631. https://doi.org/10.1007/BF02586097

[50] Deng D, Peng RL, Söderberg H, Moverare J (2018) On the formation of microstructural gradients in a nickel-base superalloy during electron beam melting. Mater Des 160:251–261. https://doi.org/10.1016/j.matdes.2018.09.006

[51] Kirka MM, Unocic KA, Raghavan N, Medina F, Dehoff RR, Babu SS (2016) Microstructure development in electron beam-melted Inconel 718 and associated tensile properties. JOM 68:1012–1020. https://doi.org/10.1007/s11837-016-1812-6

[52] Aziz MJ (1982) Model for solute redistribution during rapid solidification. J Appl Phys 53:1158–1168. https://doi.org/10.1063/1.329867

[53] Trivedi R, Kurz W (1994) Dendritic growth. Int Mater Rev 39:49–74

[54] Xiao H, Li SM, Xiao WJ, Li YQ, Cha LM, Mazumder J, Song LJ (2017) Effects of laser modes on Nb segregation and Laves phase formation during laser additive manufacturing of nickel-based superalloy. Mater Lett 188:260–262. https://doi.org/10.1016/j.matlet.2016.10.118

[55] Foster SJ, Carver K, Dinwiddie RB, List F, Unocic KA, Chaudhary A, Babu SS (2018) Process-defect-structure-property correlations during laser powder bed fusion of alloy 718: role of in situ and ex situ characterizations. Metall Mater Trans A Phys Metall Mater Sci 49:5775–5798. https://doi.org/10.1007/s11661-018-4870-2

[56] Li C, White R, Fang XY, Weaver M, Guo YB (2017) Microstructure evolution characteristics of Inconel 625 alloy from selective laser melting to heat treatment. Mater Sci Eng A 705:20–31. https://doi.org/10.1016/j.msea.2017.08.058

[57] Li S, Wei Q, Shi Y, Chua CK, Zhu Z, Zhang D (2015) Microstructure characteristics of Inconel 625 superalloy manufactured by selective laser melting. J Mater Sci Technol 31:946–952. https://doi.org/10.1016/j.jmst.2014.09.020

[58] Porter DA, Easterling KE, Sherif MY (2009) Phase transformations in metals and alloys. CRC Press, Boca Raton

[59] Kirka MM, Nandwana P, Lee Y, Dehoff RR (2017) Solidification and solid-state transformation sciences in metals additive manufacturing. Scr Mater 135:130–134. https://doi.org/10.1016/j.scriptamat.2017.01.005

[60] Babu SS, Miller MK, Vitek JM, David SA (2001) Characterization of the microstructure evolution in a nickel base superalloy during continuous cooling conditions. Acta Mater 49:4149–4160. https://doi.org/10.1016/S1359-6454(01)00314-7

[61] Gokuldoss PK, Kolla S, Eckert J (2017) Additive manufacturing processes: Selective laser melting, electron beam melting and binder jetting-selection guidelines. Materials (Basel) 10:672. https://doi.org/10.3390/ma10060672

[62] Thijs L, Verhaeghe F, Craeghs T, Van Humbeeck J, Kruth JP (2010) A study of the microstructural evolution during

selective laser melting of Ti-6Al-4V. Acta Mater 58:3303–3312. https://doi.org/10.1016/j.actamat.2010.02.004

[63] Thijs L, Kempen K, Kruth JP, Van Humbeeck J (2013) Fine-structured aluminium products with controllable texture by selective laser melting of pre-alloyed AlSi10Mg powder. Acta Mater 61:1809–1819. https://doi.org/10.1016/j.actamat.2012.11.052

[64] Carter LN, Martin C, Withers PJ, Attallah MM (2014) The influence of the laser scan strategy on grain structure and cracking behaviour in SLM powder-bed fabricated nickel superalloy. J Alloys Compd 615:338–347. https://doi.org/10.1016/j.jallcom.2014.06.172

[65] Kim SI, Hart AJ (2022) A spiral laser scanning routine for powder bed fusion inspired by natural predator-prey behaviour. Virtual Phys Prototyp 17:239–255. https://doi.org/10.1080/17452759.2022.2031232

[66] Plotkowski A (2020) Geometry-dependent solidification regimes in metal additive manufacturing. Weld J 99:59S-66S. https://doi.org/10.29391/2020.99.006

[67] Halsey W, Ferguson J, Plotkowski A, Dehoff R, Paquit V (2020) Geometry-independent microstructure optimization for electron beam powder bed fusion additive manufacturing. Addit Manuf 35:101354. https://doi.org/10.1016/j.addma.2020.101354

[68] Moyle MS, Haghdadi N, Liao XZ, Ringer SP, Primig S (2022) On the microstructure and texture evolution in 17–4 PH stainless steel during laser powder bed fusion: towards textural design. J Mater Sci Technol 117:183–195. https://doi.org/10.1016/j.jmst.2021.12.015

[69] Catchpole-Smith S, Aboulkhair N, Parry L, Tuck C, Ashcroft IA, Clare A (2017) Fractal scan strategies for selective laser melting of 'unweldable' nickel superalloys. Addit Manuf 15:113–122. https://doi.org/10.1016/j.addma.2017.02.002

[70] Zhang H, Gu D, Dai D (2022) Laser printing path and its influence on molten pool configuration, microstructure and mechanical properties of laser powder bed fusion processed rare earth element modified Al-Mg alloy. Virtual Phys Prototyp 17:308–328. https://doi.org/10.1080/17452759.2022.2036530

[71] Raghavan N, Dehoff R, Pannala S, Simunovic S, Kirka MM, Turner J, Carlson N, Babu SS (2016) Numerical modeling of heat-transfer and the influence of process parameters on tailoring the grain morphology of IN718 in electron beam additive manufacturing. Acta Mater 112:303–314. https://doi.org/10.1016/j.actamat.2016.03.063

[72] McLouth TD, Witkin DB, Bean GE, Sitzman SD, Adams PM, Lohser JR, Yang JM, Zaldivar RJ (2020) Variations in ambient and elevated temperature mechanical behavior of IN718 manufactured by selective laser melting via process parameter control. Mater Sci Eng A 780:139184. https://doi.org/10.1016/j.msea.2020.139184

[73] Balachandramurthi AR, Olsson J, Ålgårdh J, Snis A, Moverare J, Pederson R (2019) Microstructure tailoring in electron beam powder bed fusion additive manufacturing and its potential consequences. Results Mater 1:100017. https://doi.org/10.1016/j.rinma.2019.100017

[74] Kirka MM, Lee Y, Greeley DA, Okello A, Goin MJ, Pearce MT, Dehoff RR (2017) Strategy for texture management in metals additive manufacturing. JOM 69:948. https://doi.org/10.1007/s11837-017-2297-7

[75] Geiger F, Kunze K, Etter T (2016) Tailoring the texture of IN738LC processed by selective laser melting (SLM) by specific scanning strategies. Mater Sci Eng A 661:240–246. https://doi.org/10.1016/j.msea.2016.03.036

[76] Nadammal N, Cabeza S, Mishurova T, Thiede T, Kromm A, Seyfert C, Farahbod L, Haberland C, Schneider JA, Portella PD, Bruno G (2017) Effect of hatch length on the development of microstructure, texture and residual stresses in selective laser melted superalloy Inconel 718. Mater Des 134:139–150. https://doi.org/10.1016/j.matdes.2017.08.049

[77] Wan HY, Zhou ZJ, Li CP, Chen GF, Zhang GP (2018) Effect of scanning strategy on grain structure and crystallographic texture of Inconel 718 processed by selective laser melting. J Mater Sci Technol 34:1799–1804. https://doi.org/10.1016/j.jmst.2018.02.002

[78] Jia H, Sun H, Wang H, Wu Y, Wang H (2021) Scanning strategy in selective laser melting (SLM): a review. Int J Adv Manuf Technol 113:2413–2435. https://doi.org/10.1007/s00170-021-06810-3

[79] Jhabvala J, Boillat E, Antignac T, Glardon R (2010) On the effect of scanning strategies in the selective laser melting process. Virtual Phys Prototyp 5:99–109. https://doi.org/10.1080/17452751003688368

[80] Lopez-Galilea I, Ruttert B, He J, Hammerschmidt T, Drautz R, Gault B, Theisen W (2019) Additive manufacturing of CMSX-4 Ni-base superalloy by selective laser melting: Influence of processing parameters and heat treatment. Addit Manuf 30:100874. https://doi.org/10.1016/j.addma.2019.100874

[81] Ding X, Koizumi Y, Aoyagi K, Kii T, Sasaki N, Hayasaka Y, Yamanaka K, Chiba A (2019) Microstructural control of alloy 718 fabricated by electron beam melting with expanded processing window by adaptive offset method. Mater Sci Eng A 764:138058. https://doi.org/10.1016/j.msea.2019.138058

[82] Gokcekaya O, Ishimoto T, Hibino S, Yasutomi J, Narushima T, Nakano T (2021) Unique crystallographic texture

formation in Inconel 718 by laser powder bed fusion and its effect on mechanical anisotropy. Acta Mater 212:116876. https://doi.org/10.1016/j.actamat.2021.116876

[83] Dehoff RR, Kirka MM, List FA, Unocic KA, Sames WJ (2015) Crystallographic texture engineering through novel melt strategies via electron beam melting: Inconel 718. Mater Sci Technol (United Kingdom) 31:939–944. https://doi.org/10.1179/1743284714Y.0000000697

[84] Körner C, Helmer H, Bauereiß A, Singer RF (2014) Tailoring the grain structure of IN718 during selective electron beam melting. MATEC Web Conf 14:08001. https://doi.org/10.1051/matecconf/20141408001

[85] Plotkowski A, Ferguson J, Stump B, Halsey W, Paquit V, Joslin C, Babu SS, Marquez Rossy A, Kirka MM, Dehoff RR (2021) A stochastic scan strategy for grain structure control in complex geometries using electron beam powder bed fusion. Addit Manuf 46:102092. https://doi.org/10.1016/j.addma.2021.102092

[86] Zavala-Arredondo M, Boone N, Willmott J, Childs DTD, Ivanov P, Groom KM, Mumtaz K (2017) Laser diode area melting for high speed additive manufacturing of metallic components. Mater Des 117:305–315. https://doi.org/10.1016/j.matdes.2016.12.095

[87] Holland S, Wang X, Fang XY, Guo YB, Yan F, Li L (2018) Grain boundary network evolution in Inconel 718 from selective laser melting to heat treatment. Mater Sci Eng A 725:406–418. https://doi.org/10.1016/j.msea.2018.04.045

[88] Wang X, Keya T, Chou K (2016) Build height effect on the Inconel 718 parts fabricated by selective laser melting. Procedia Manuf 5:1006–1017. https://doi.org/10.1016/j.promfg.2016.08.089

[89] Du D, Dong A, Shu D, Zhu G, Sun B, Li X, Lavernia E (2019) Influence of build orientation on microstructure, mechanical and corrosion behavior of Inconel 718 processed by selective laser melting. Mater Sci Eng A 760:469–480. https://doi.org/10.1016/j.msea.2019.05.013

[90] Karimi P, Sadeghi E, Deng D, Gruber H, Andersson J, Nylén P (2018) Influence of build layout and orientation on microstructural characteristics of electron beam melted Alloy 718. Int J Adv Manuf Technol 99:2903–2913. https://doi.org/10.1007/s00170-018-2621-6

[91] Bean GE, McLouth TD, Witkin DB, Sitzman SD, Adams PM, Zaldivar RJ (2019) Build orientation effects on texture and mechanical properties of selective laser melting Inconel 718. J Mater Eng Perform 28:1942–1949. https://doi.org/10.1007/s11665-019-03980-w

[92] Watring DS, Benzing JT, Hrabe N, Spear AD (2020) Effects of laser-energy density and build orientation on the structure–property relationships in as-built Inconel 718 manufactured by laser powder bed fusion. Addit Manuf 36:101425. https://doi.org/10.1016/j.addma.2020.101425

[93] Kotzem D, Arold T, Niendorf T, Walther F (2020) Influence of specimen position on the build platform on the mechanical properties of as-built direct aged electron beam melted Inconel 718 alloy. Mater Sci Eng A 772:138785. https://doi.org/10.1016/j.msea.2019.138785

[94] Sun SH, Koizumi Y, Saito T, Yamanaka K, Li YP, Cui Y, Chiba A (2018) Electron beam additive manufacturing of Inconel 718 alloy rods: Impact of build direction on microstructure and high-temperature tensile properties. Addit Manuf 23:457–470. https://doi.org/10.1016/j.addma.2018.08.017

[95] David SA, Vitek JM (1989) Correlation between solidification parameters and weld microstructures. Int Mater Rev 34:213–245. https://doi.org/10.1179/imr.1989.34.1.213

[96] Kuo YL, Horikawa S, Kakehi K (2017) The effect of interdendritic δ phase on the mechanical properties of alloy 718 built up by additive manufacturing. Mater Des 116:411–418. https://doi.org/10.1016/j.matdes.2016.12.026

[97] Cheng B, Gu J, Song M (2020) An investigation of the microstructural evolution and tensile properties of a nickel-based GH648 superalloy manufactured through selective laser melting. Mater Sci Eng A 790:1–10. https://doi.org/10.1016/j.msea.2020.139704

[98] Song H, McGaughy T, Sadek A, Zhang W (2019) Effect of structural support on microstructure of nickel base superalloy fabricated by laser-powder bed fusion additive manufacturing. Addit Manuf 26:30–40. https://doi.org/10.1016/j.addma.2018.12.017

[99] Hilaire A, Andrieu E, Wu X (2019) High-temperature mechanical properties of alloy 718 produced by laser powder bed fusion with different processing parameters. Addit Manuf 26:147–160. https://doi.org/10.1016/j.addma.2019.01.012

[100] Pröbstle M, Neumeier S, Hopfenmüller J, Freund LP, Niendorf T, Schwarze D, Göken M (2016) Superior creep strength of a nickel-based superalloy produced by selective laser melting. Mater Sci Eng A 674:299–307. https://doi.org/10.1016/j.msea.2016.07.061

[101] Bertsch KM, Meric de Bellefon G, Kuehl B, Thoma DJ (2020) Origin of dislocation structures in an additively manufactured austenitic stainless steel 316L. Acta Mater 199:19–33. https://doi.org/10.1016/j.actamat.2020.07.063

[102] Gallmeyer TG, Moorthy S, Kappes BB, Mills MJ, Amin-Ahmadi B, Stebner AP (2020) Knowledge of process-structure-property relationships to engineer better heat treatments for laser powder bed fusion additive manufactured Inconel 718. Addit Manuf 31:100977. https://doi.org/10.1016/j.addma.2019.100977

[103] Vilaro T, Colin C, Bartout JD, Nazé L, Sennour M (2012) Microstructural and mechanical approaches of the selective laser melting process applied to a nickel-base superalloy. Mater Sci Eng A 534:446–451. https://doi.org/10.1016/j.msea.2011.11.092

[104] Kumara C, Balachandramurthi AR, Goel S, Hanning F, Moverare J (2020) Toward a better understanding of phase transformations in additive manufacturing of alloy 718. Materialia 13:100862. https://doi.org/10.1016/j.mtla.2020.100862

[105] Wills VA, McCartney DG (1991) A comparative study of solidification features in nickel-base superalloys: microstructural evolution and microsegregation. Mater Sci Eng A 145:223–232. https://doi.org/10.1016/0921-5093(91)90252-I

[106] Frederick CL, Plotkowski A, Kirka MM, Haines M, Staub A, Schwalbach EJ, Cullen D, Babu SS (2018) Geometry-induced spatial variation of microstructure evolution during selective electron beam melting of Rene-N5. Metall Mater Trans A Phys Metall Mater Sci 49:5080–5096. https://doi.org/10.1007/s11661-018-4793-y

[107] Kirka MM, Medina F, Dehoff R, Okello A (2017) Mechanical behavior of post-processed Inconel 718 manufactured through the electron beam melting process. Mater Sci Eng A 680:338–346. https://doi.org/10.1016/j.msea.2016.10.069

[108] Parsa AB, Ramsperger M, Kostka A, Somsen C, Körner C, Eggeler G (2016) Transmission electron microscopy of a CMSX-4 Ni-base superalloy produced by selective electron beam melting. Metals (Basel) 6:1–17. https://doi.org/10.3390/met6110258

[109] Chauvet E, Tassin C, Blandin JJ, Dendievel R, Martin G (2018) Producing Ni-base superalloys single crystal by selective electron beam melting. Scr Mater 152:15–19. https://doi.org/10.1016/j.scriptamat.2018.03.041

[110] Kuo YL, Kamigaichi A, Kakehi K (2018) Characterization of Ni-based superalloy built by selective laser melting and electron beam melting. Metall Mater Trans A Phys Metall Mater Sci 49:3831–3837. https://doi.org/10.1007/s11661-018-4769-y

[111] Yoo MH (1986) Effects of elastic anisotropy on the anomalous yield behavior of cubic ordered alloys. MRS Proc 81:207. https://doi.org/10.1557/PROC-81-207

[112] Reed RC (2008) The superalloys: fundamentals and applications. Cambridge University Press, Cambridge

[113] Design A, Turbine G, Transfer H, Technology C, Aminaee A (2014) Turbine aerodynamics, heat transfer, materials, and mechanics. American Institute of Aeronautics and Astronautics, Inc., Reston. https://doi.org/10.2514/4.102660

[114] Reed RC, Yeh AC, Tin S, Babu SS, Miller MK (2004) Identification of the partitioning characteristics of ruthenium in single crystal superalloys using atom probe tomography. Scr Mater 51:327–331. https://doi.org/10.1016/j.scriptamat.2004.04.019

[115] Grose DA, Ansell GS (1981) The influence of coherency strain on the elevated temperature tensile behavior of Ni-15Cr-AI-Ti-Mo alloys. Metall Trans A 12:1631–1645. https://doi.org/10.1007/BF02643569

[116] Divya VD, Muñoz-Moreno R, Messé OMDM, Barnard JS, Baker S, Illston T, Stone HJ (2016) Microstructure of selective laser melted CM247LC nickel-based superalloy and its evolution through heat treatment. Mater Charact 114:62–74. https://doi.org/10.1016/j.matchar.2016.02.004

[117] Otto R, Brøtan V, Carvalho PA, Reiersen M, Graff JS, Sunding MF, Berg OÅ, Diplas S, Azar AS (2021) Roadmap for additive manufacturing of HAYNES® 282® superalloy by laser beam powder bed fusion (PBF-LB) technology. Mater Des 204:109656. https://doi.org/10.1016/j.matdes.2021.109656

[118] Babu SS, Raghavan N, Raplee J, Foster SJ, Frederick C, Haines M, Dinwiddie R, Kirka MK, Plotkowski A, Lee Y, Dehoff RR (2018) Additive Manufacturing of Nickel Superalloys: opportunities for Innovation and challenges related to qualification. Metall Mater Trans A Phys Metall Mater Sci 49:3764–3780. https://doi.org/10.1007/s11661-018-4702-4

[119] Lim B, Chen H, Chen Z, Haghdadi N, Liao X, Primig S, Babu SS, Breen AJ, Ringer SP (2021) Microstructure-property gradients in Ni-based superalloy (Inconel 738) additively manufactured via electron beam powder bed fusion. Addit Manuf 46:102121. https://doi.org/10.1016/j.addma.2021.102121

[120] Unocic KA, Kirka MM, Cakmak E, Greeley D, Okello AO, Dryepondt S (2020) Evaluation of additive electron beam melting of Haynes 282 alloy. Mater Sci Eng A 772:138607. https://doi.org/10.1016/j.msea.2019.138607

[121] Wang Y, Khachaturyan AG (1995) Shape instability during precipitate growth in coherent solids. Acta Metall Mater 43:1837–1857. https://doi.org/10.1016/0956-7151(94)00406-8

[122] Ramsperger M, Singer RF, Körner C (2016) Microstructure of the nickel-base superalloy CMSX-4 fabricated by selective electron beam melting. Metall Mater Trans A Phys Metall Mater Sci 47:1469–1480. https://doi.org/10.1007/s11661-015-3300-y

[123] Chauvet E, Kontis P, Jägle EA, Gault B, Raabe D, Tassin C, Blandin JJ, Dendievel R, Vayre B, Abed S, Martin G (2018) Hot cracking mechanism affecting a non-weldable Ni-based superalloy produced by selective electron beam

melting. Acta Mater 142:82–94. https://doi.org/10.1016/j.actamat.2017.09.047

[124] Ruttert B, Ramsperger M, Mujica Roncery L, Lopez-Galilea I, Körner C, Theisen W (2016) Impact of hot isostatic pressing on microstructures of CMSX-4 Ni-base superalloy fabricated by selective electron beam melting. Mater Des 110:720–727. https://doi.org/10.1016/j.matdes.2016.08.041

[125] Murr LE, Martinez E, Pan XM, Gaytan SM, Castro JA, Terrazas CA, Medina F, Wicker RB, Abbott DH (2013) Microstructures of Rene 142 nickel-based superalloy fabricated by electron beam melting. Acta Mater 61:4289–4296. https://doi.org/10.1016/j.actamat.2013.04.002

[126] Frederick CL (2018) Control of grain structure in selective-electron beam melting of nickel-based superalloys. Knoxville: University of Tennessee. https://trace.tennessee.edu/utk_graddiss/4952

[127] Haghdadi N, Whitelock E, Lim B, Chen H, Liao X, Babu SS, Ringer SP, Primig S (2020) Multimodal γ′ precipitation in Inconel-738 Ni-based superalloy during electron-beam powder bed fusion additive manufacturing. J Mater Sci 55:13342–13350. https://doi.org/10.1007/s10853-020-04915-w

[128] Hagel W, Beattie H (1959) Iron and steel institute special report, London

[129] Chaudhari M, Singh A, Gopal P, Nag S, Viswanathan GB, Tiley J, Banerjee R, Du J (2012) Site occupancy of chromium in the γ′-Ni_3Al phase of nickel-based superalloys: a combined 3D atom probe and first-principles study. Philos Mag Lett 92:495–506. https://doi.org/10.1080/09500839.2012.690904

[130] Eriş R, Akdeniz MV, Mekhrabov AO (2021) The site preferences of transition elements and their synergistic effects on the bonding strengthening and structural stability of γ′-Ni_3Al precipitates in Ni-based superalloys: a first-principles investigation. Metall Mater Trans A 52:2298–2313. https://doi.org/10.1007/s11661-021-06222-8

[131] Chandra S, Tan X, Narayan RL, Descoins M, Mangelinck D, Tor SB, Liu E, Seet G (2021) Nanometer-scale precipitations in a selective electron beam melted nickel-based superalloy. Scr Mater 194:113661. https://doi.org/10.1016/j.scriptamat.2020.113661

[132] Yang H, Yang J, Huang W, Jing G, Wang Z, Zeng X (2019) Controllable in-situ aging during selective laser melting: Stepwise precipitation of multiple strengthening phases in Inconel 718 alloy. J Mater Sci Technol 35:1925–1930. https://doi.org/10.1016/j.jmst.2019.05.024

[133] Zhao JR, Hung FY, Lui TS (2020) Microstructure and tensile fracture behavior of three-stage heat treated inconel 718 alloy produced via laser powder bed fusion process. J Mater Res Technol 9:3357–3367. https://doi.org/10.1016/j.jmrt.2020.01.030

[134] Cao GH, Sun TY, Wang CH, Li X, Liu M, Zhang ZX, Hu PF, Russell AM, Schneider R, Gerthsen D, Zhou ZJ, Li CP, Chen GF (2018) Investigations of γ′ γ″ and δ precipitates in heat-treated Inconel 718 alloy fabricated by selective laser melting. Mater Charact 136:398–406. https://doi.org/10.1016/j.matchar.2018.01.006

[135] Peng H, Shi Y, Gong S, Guo H, Chen B (2018) Microstructure, mechanical properties and cracking behaviour in a γ′-precipitation strengthened nickel-base superalloy fabricated by electron beam melting. Mater Des 159:155–169. https://doi.org/10.1016/j.matdes.2018.08.054

[136] Matache G, Stefanescu DM, Puscasu C, Alexandrescu E (2016) Dendritic segregation and arm spacing in directionally solidified CMSX-4 superalloy. Int J Cast Met Res 29:303–316. https://doi.org/10.1080/13640461.2016.1166726

[137] Wang F, Ma D, Zhang J, Liu L, Hong J, Bogner S, Bührig-Polaczek A (2014) Effect of solidification parameters on the microstructures of superalloy CMSX-6 formed during the downward directional solidification process. J Cryst Growth 389:47–54. https://doi.org/10.1016/j.jcrysgro.2013.11.084

[138] Zhao X, Liu L, Yu Z, Zhang W, Zhang J, Fu H (2010) Influence of directional solidification variables on the microstructure and crystal orientation of AM3 under high thermal gradient. J Mater Sci 45:6101–6107. https://doi.org/10.1007/s10853-010-4696-9

[139] Pistor J, Körner C (2019) Formation of topologically closed packed phases within CMSX-4 single crystals produced by additive manufacturing. Mater Lett X 1:100003. https://doi.org/10.1016/j.mlblux.2019.100003

[140] Raghavan N, Simunovic S, Dehoff R, Plotkowski A, Turner J, Kirka M, Babu S (2017) Localized melt-scan strategy for site specific control of grain size and primary dendrite arm spacing in electron beam additive manufacturing. Acta Mater 140:375–387. https://doi.org/10.1016/j.actamat.2017.08.038

[141] Oblak JM, Paulonis DF, Duvall DS (1974) Coherency strengthening in Ni base alloys hardened by DO22 γ′ precipitates. Metall Trans 5:143–153. https://doi.org/10.1007/BF02642938

[142] Cozar R, Pineau A (1973) Morphology of gamma prime and gamma double prime precipitates and thermal stability of Inconel 718 type alloys. Metall Mater Trans B 4:47–59. https://doi.org/10.1007/BF02649604

[143] Theska F, Stanojevic A, Oberwinkler B, Ringer SP, Primig S (2018) On conventional versus direct ageing of Alloy 718. Acta Mater 156:116–124. https://doi.org/10.1016/j.actamat.2018.06.034

[144] Rielli VV, Theska F, Godor F, Stanojevic A, Oberwinkler B, Primig S (2021) Evolution of nanoscale precipitates during common Alloy 718 ageing treatments. Mater Des 205:109762. https://doi.org/10.1016/j.matdes.2021.109762

[145] Zhang S, Lin X, Wang L, Yu X, Hu Y, Yang H, Lei L, Huang W (2021) Strengthening mechanisms in selective laser-melted Inconel 718 superalloy. Mater Sci Eng A 812:141145. https://doi.org/10.1016/j.msea.2021.141145

[146] Sames WJ, Unocic KA, Dehoff RR, Lolla T, Babu SS (2014) Thermal effects on microstructural heterogeneity of Inconel 718 materials fabricated by electron beam melting. J Mater Res 29:1920–1930. https://doi.org/10.1557/jmr.2014.140

[147] Wang X, Wang J, Kang J, Wang T, Wu P, Feng T, Zheng L, Rong Y (2021) High-throughput investigation of laser powder bed fabricated Inconel 718 alloy: fabrication, microstructure and performance. Mater Today Commun 27:102303. https://doi.org/10.1016/j.mtcomm.2021.102303

[148] Calandri M, Yin S, Aldwell B, Calignano F, Lupoi R, Ugues D (2019) Texture and microstructural features at different length scales in Inconel 718 produced by selective laser melting. Materials (Basel) 12(8):1293. https://doi.org/10.3390/ma12081293

[149] Piglione A, Attard B, Rielli VV, Maldonado C-TS, Attallah MM, Primig S, Pham M-S (2021) On the constitutive relationship between solidification cells and the fatigue behaviour of IN718 fabricated by laser powder bed fusion. Addit Manuf 47:102347. https://doi.org/10.1016/j.addma.2021.102347

[150] Rielli VV, Godor F, Gruber C, Stanojevic A, Oberwinkler B, Primig S (2021) Effects of processing heterogeneities on the micro- to nanostructure strengthening mechanisms of an alloy 718 turbine disk. Mater Des 212:110295. https://doi.org/10.1016/j.matdes.2021.110295

[151] Goodfellow AJ (2018) Strengthening mechanisms in polycrystalline nickel-based superalloys. Mater Sci Technol (United Kingdom) 34:1793–1808. https://doi.org/10.1080/02670836.2018.1461594

[152] Sui S, Tan H, Chen J, Zhong C, Li Z, Fan W, Gasser A, Huang W (2019) The influence of Laves phases on the room temperature tensile properties of Inconel 718 fabricated by powder feeding laser additive manufacturing. Acta Mater 164:413–427. https://doi.org/10.1016/j.actamat.2018.10.032

[153] Radavich JF (2012) The physical metallurgy of cast and wrought Alloy 718. Superalloy 718:229–240. https://doi.org/10.7449/1989/superalloys_1989_229_240

[154] Slama C, Cizeron G (1997) Étude du comportement structural de l'alliage NC 19 Fe Nb (Inconel 718). J Phys III 7:665–688

[155] Geng L, Na YS, Park NK (1997) Continuous cooling transformation behavior of Alloy 718. Mater Lett 30:401–405. https://doi.org/10.1016/S0167-577X(96)00225-X

[156] Kumara C, Deng D, Hanning F, Raanes M, Moverare J, Nylén P (2019) Predicting the microstructural evolution of electron beam melting of Alloy 718 with phase-field modeling. Metall Mater Trans A Phys Metall Mater Sci 50:2527–2537. https://doi.org/10.1007/s11661-019-05163-7

[157] Promoppatum P, Yao S-C, Pistorius PC, Rollett AD, Coutts PJ, Lia F, Martukanitz R (2018) Numerical modeling and experimental validation of thermal history and microstructure for additive manufacturing of an Inconel 718 product. Prog Addit Manuf 3:15–32

[158] Deng D, Moverare J, Peng RL, Söderberg H (2017) Microstructure and anisotropic mechanical properties of EBM manufactured Inconel 718 and effects of post heat treatments. Mater Sci Eng A 693:151–163. https://doi.org/10.1016/j.msea.2017.03.085

[159] Strondl A, Fischer R, Frommeyer G, Schneider A (2008) Investigations of MX and γ'/γ'' precipitates in the nickel-based superalloy 718 produced by electron beam melting. Mater Sci Eng A 480:138–147. https://doi.org/10.1016/j.msea.2007.07.012

[160] Sadeghi E, Karimi P, Momeni S, Seifi M, Eklund A, Andersson J (2019) Influence of thermal post treatments on microstructure and oxidation behavior of EB-PBF manufactured Alloy 718. Mater Charact 150:236–251. https://doi.org/10.1016/j.matchar.2019.02.016

[161] Amato KN, Gaytan SM, Murr LE, Martinez E, Shindo PW, Hernandez J, Collins S, Medina F (2012) Microstructures and mechanical behavior of Inconel 718 fabricated by selective laser melting. Acta Mater 60:2229–2239. https://doi.org/10.1016/j.actamat.2011.12.032

[162] Jeyaprakash N, Yang CH, Ramkumar KR (2021) Microstructural, mechanical and wear behaviour of Inconel-718 produced through laser-powder bed-fused additive manufacturing. Mater Sci Technol (United Kingdom) 37:326–337. https://doi.org/10.1080/02670836.2021.1893457

[163] Ni M, Chen C, Wang X, Wang P, Li R, Zhang X, Zhou K (2017) Anisotropic tensile behavior of in situ precipitation strengthened Inconel 718 fabricated by additive

manufacturing. Mater Sci Eng A 701:344–351. https://doi.org/10.1016/j.msea.2017.06.098

[164] Čapek J, Polatidis E, Knapek M, Lyphout C, Casati N, Pederson R, Strobl M (2021) The effect of γ″ and δ phase precipitation on the mechanical properties of Inconel 718 manufactured by selective laser melting: an in situ neutron diffraction and acoustic emission study. JOM 73:223–232. https://doi.org/10.1007/s11837-020-04463-3

[165] Zhang B, Wang P, Chew Y, Wen Y, Zhang M, Wang P, Bi G, Wei J (2020) Mechanical properties and microstructure evolution of selective laser melting Inconel 718 along building direction and sectional dimension. Mater Sci Eng A 794:139941. https://doi.org/10.1016/j.msea.2020.139941

[166] Tucho WM, Cuvillier P, Sjolyst-Kverneland A, Hansen V (2017) Microstructure and hardness studies of Inconel 718 manufactured by selective laser melting before and after solution heat treatment. Mater Sci Eng A 689:220–232. https://doi.org/10.1016/j.msea.2017.02.062

[167] Yang H, Yang J, Huang W, Wang Z, Zeng X (2018) The printability, microstructure, crystallographic features and microhardness of selective laser melted Inconel 718 thin wall. Mater Des 156:407–418. https://doi.org/10.1016/j.matdes.2018.07.007

[168] Eiselstein HL, Tillack DJ (1991) The invention and definition of Alloy 625. Superalloys 718:1–14. https://doi.org/10.7449/1991/Superalloys_1991_1_14

[169] Rivera OG, Allison PG, Jordon JB, Rodriguez OL, Brewer LN, McClelland Z, Whittington WR, Francis D, Su J, Martens RL, Hardwick N (2017) Microstructures and mechanical behavior of Inconel 625 fabricated by solid-state additive manufacturing. Mater Sci Eng A 694:1–9. https://doi.org/10.1016/j.msea.2017.03.105

[170] Cooper DE, Blundell N, Maggs S, Gibbons GJ (2013) Additive layer manufacture of Inconel 625 metal matrix composites, reinforcement material evaluation. J Mater Process Technol 213:2191–2200. https://doi.org/10.1016/j.jmatprotec.2013.06.021

[171] Marchese G, Lorusso M, Parizia S, Bassini E, Lee JW, Calignano F, Manfredi D, Terner M, Hong HU, Ugues D, Lombardi M, Biamino S (2018) Influence of heat treatments on microstructure evolution and mechanical properties of Inconel 625 processed by laser powder bed fusion. Mater Sci Eng A 729:64–75. https://doi.org/10.1016/j.msea.2018.05.044

[172] De Terris T, Castelnau O, Hadjem-Hamouche Z, Haddadi H, Michel V, Peyre P (2021) Analysis of as-built microstructures and recrystallization phenomena on Inconel 625 Alloy obtained via laser powder bed fusion (L-PBF). Metals (Basel) 11:619. https://doi.org/10.3390/met11040619

[173] Amato K (2012) Comparison of microstructures and properties for a Ni-base superalloy (Alloy 625) fabricated by electron beam melting. J Mater Sci Res 1:3. https://doi.org/10.5539/jmsr.v1n2p3

[174] Murr LE (2015) Metallurgy of additive manufacturing: examples from electron beam melting. Addit Manuf 5:40–53. https://doi.org/10.1016/j.addma.2014.12.002

[175] Kelkar R, Andreaco A, Ott E, Groh J (2018) Alloy 718: laser powder bed additive manufacturing for turbine applications BT. In: Ott E, Liu X, Andersson J, Bi Z, Bockenstedt K, Dempster I, Groh J, Heck K, Jablonski P, Kaplan M, Nagahama D, Sudbrack C (eds) Proceedings of the 9th international symposium on superalloy 718 & Derivatives: energy, aerospace, and industrial applications. Springer International Publishing, Cham, pp 53–68

[176] Gundgire T, Goel S, Klement U, Joshi S (2020) Response of different electron beam melting produced Alloy 718 microstructures to thermal post-treatments. Mater Charact 167:110498. https://doi.org/10.1016/j.matchar.2020.110498

[177] Goel S, Mehtani H, Yao SW, Samajdar I, Klement U, Joshi S (2020) As-built and post-treated microstructures of an electron beam melting (EBM) produced nickel-based superalloy. Metall Mater Trans A Phys Metall Mater Sci 51:6546–6559. https://doi.org/10.1007/s11661-020-06037-z

[178] Nandwana P, Kirka M, Okello A, Dehoff R (2018) Electron beam melting of Inconel 718: effects of processing and post-processing. Mater Sci Technol (United Kingdom) 34:612–619. https://doi.org/10.1080/02670836.2018.1424379

[179] Ramakrishna M, Koppoju S, Telasang G, Korla R, Padmanabham G (2021) Effect of solutionizing temperature on the microstructural evolution during double aging of powder bed fusion-additive manufactured IN718 alloy. Mater Charact 172:110868. https://doi.org/10.1016/j.matchar.2020.110868

[180] Wang Z, Guan K, Gao M, Li X, Chen X, Zeng X (2012) The microstructure and mechanical properties of deposited-IN718 by selective laser melting. J Alloys Compd 513:518–523. https://doi.org/10.1016/j.jallcom.2011.10.107

[181] Ferreri NC, Vogel SC, Knezevic M (2020) Determining volume fractions of γ, γ′, γ″, δ, and MC-carbide phases in Inconel 718 as a function of its processing history using an advanced neutron diffraction procedure. Mater Sci Eng A 781:139228. https://doi.org/10.1016/j.msea.2020.139228

[182] Sarley B, Manero A, Cotelo J, Okasinski J, Kenesei P, Almer J, Wischek J, Bartsch M, Raghavan S (2017) Real-time phase evolution of selective laser melted (SLM) Inconel 718 with temperature through synchrotron X-rays.

In: 58th AIAA/ASCE/AHS/ASC Struct Struct Dyn Mater Conf 2017. https://doi.org/10.2514/6.2017-1542.

[183] Gribbin S, Ghorbanpour S, Ferreri NC, Bicknell J, Tsukrov I, Knezevic M (2019) Role of grain structure, grain boundaries, crystallographic texture, precipitates, and porosity on fatigue behavior of Inconel 718 at room and elevated temperatures. Mater Charact 149:184–197. https://doi.org/10.1016/j.matchar.2019.01.028

[184] Yang B, Shang Z, Ding J, Lopez J, Jarosinski W, Sun T, Richter N, Zhang Y, Wang H, Zhang X (2022) Investigation of strengthening mechanisms in an additively manufactured Haynes 230 alloy. Acta Mater 222:117404. https://doi.org/10.1016/j.actamat.2021.117404

[185] Messé OMDM, Muñoz-Moreno R, Illston T, Baker S, Stone HJ (2018) Metastable carbides and their impact on recrystallisation in IN738LC processed by selective laser melting. Addit Manuf 22:394–404. https://doi.org/10.1016/j.addma.2018.05.030

[186] Youdelis WV, Kwon O (1983) Carbide phases in nickel base superalloy: nucleation properties of MC type carbide. Met Sci 17:385–388. https://doi.org/10.1179/030634583790420673

[187] Chen QZ, Jones N, Knowles DM (2002) The microstructures of base/modified RR2072 SX superalloys and their effects on creep properties at elevated temperatures. Acta Mater 50:1095–1112. https://doi.org/10.1016/S1359-6454(01)00410-4

[188] Fernandez R, LeComte JC, Kattamis TZ (1978) Effect of solidification parameters on the growth geometry of MC carbide in IN-100 dendritic monocrystals. Metall Trans A 9:1381–1386. https://doi.org/10.1007/BF02661809

[189] Ghasemi A, Kolagar AM, Pouranvari M (2020) Microstructure-performance relationships in gas tungsten arc welded Hastelloy X nickel-based superalloy. Mater Sci Eng A 793:139861. https://doi.org/10.1016/j.msea.2020.139861

[190] Liu L, Sommer F, Fu HZ (1994) Effect of solidification conditions on MC carbides in a nickel-base superalloy IN 738 LC. Scr Metall Mater 30:587–591. https://doi.org/10.1016/0956-716X(94)90434-0

[191] Popovich VA, Borisov EV, Popovich AA, Sufiiarov VS, Masaylo DV, Alzina L (2017) Impact of heat treatment on mechanical behaviour of Inconel 718 processed with tailored microstructure by selective laser melting. Mater Des 131:12–22. https://doi.org/10.1016/j.matdes.2017.05.065

[192] Marchese G, Colera XG, Calignano F, Lorusso M, Biamino S, Minetola P, Manfredi D (2017) Characterization and comparison of Inconel 625 processed by selective laser melting and laser metal deposition. Adv Eng Mater 19:1–9. https://doi.org/10.1002/adem.201600635

[193] Garosshen TJ, McCarthy GP (1985) Low temperature carbide precipitation in a nickel base superalloy. Metall Trans A 16:1213–1223. https://doi.org/10.1007/BF02670326

[194] Sundararaman M, Mukhopadhyay P, Banerjee S (2012) Carbide precipitation in nickel base superalloys 718 and 625 and their effect on mechanical Properties. Superalloys 718:367–378. https://doi.org/10.7449/1997/superalloys_1997_367_378

[195] Tomus D, Tian Y, Rometsch PA, Heilmaier M, Wu X (2016) Influence of post heat treatments on anisotropy of mechanical behaviour and microstructure of Hastelloy-X parts produced by selective laser melting. Mater Sci Eng A 667:42–53. https://doi.org/10.1016/j.msea.2016.04.086

[196] Ramsperger M, Roncery LM, Lopez-Galilea I, Singer RF, Theisen W, Körner C (2015) Solution heat treatment of the single crystal nickel-base superalloy CMSX-4 fabricated by selective electron beam melting. Adv Eng Mater 17:1486–1493. https://doi.org/10.1002/adem.201500037

[197] Montero-Sistiaga ML, Liu Z, Bautmans L, Nardone S, Ji G, Kruth JP, Van Humbeeck J, Vanmeensel K (2020) Effect of temperature on the microstructure and tensile properties of micro-crack free hastelloy X produced by selective laser melting. Addit Manuf 31:100995. https://doi.org/10.1016/j.addma.2019.100995

[198] Harrison NJ, Todd I, Mumtaz K (2015) Reduction of micro-cracking in nickel superalloys processed by selective laser melting: a fundamental alloy design approach. Acta Mater 94:59–68. https://doi.org/10.1016/j.actamat.2015.04.035

[199] Han Q, Gu Y, Soe S, Lacan F, Setchi R (2020) Effect of hot cracking on the mechanical properties of Hastelloy X superalloy fabricated by laser powder bed fusion additive manufacturing. Opt Laser Technol 124:105984. https://doi.org/10.1016/j.optlastec.2019.105984

[200] Ni X, Kong D, Zhang L, Dong C, Song J, Wu W (2019) Effect of process parameters on the mechanical properties of Hastelloy X Alloy fabricated by selective laser melting. J Mater Eng Perform 28:5533–5540. https://doi.org/10.1007/s11665-019-04275-w

[201] Sanchez-Mata O, Wang X, Muñiz-Lerma JA, Shandiz MA, Gauvin R, Brochu M (2018) Fabrication of crack-free nickel-based superalloy considered non-weldable during laser powder bed fusion. Materials (Basel) 11:1–9. https://doi.org/10.3390/ma11081288

[202] Marchese G, Basile G, Bassini E, Aversa A, Lombardi M, Ugues D, Fino P, Biamino S (2018) Study of the microstructure and cracking mechanisms of hastelloy X produced by laser powder bed fusion. Materials (Basel) 11:106. https://doi.org/10.3390/ma11010106

[203] Kong D, Ni X, Dong C, Zhang L, Yao J, Man C, Wang L, Xiao K, Li X (2019) Anisotropic response in mechanical and corrosion properties of hastelloy X fabricated by selective laser melting. Constr Build Mater 221:720–729. https://doi.org/10.1016/j.conbuildmat.2019.06.132

[204] Romedenne M, Pillai R, Kirka M, Dryepondt S (2020) High temperature air oxidation behavior of Hastelloy X processed by Electron Beam Melting (EBM) and Selective Laser Melting (SLM). Corros Sci 171:108647. https://doi.org/10.1016/j.corsci.2020.108647

[205] Karapuzha AS, Fraser D, Schliephake D, Dietrich S, Zhu Y, Wu X, Huang A (2021) Microstructure, mechanical behaviour and strengthening mechanisms in Hastelloy X manufactured by electron beam and laser beam powder bed fusion. J Alloys Compd 862:158034. https://doi.org/10.1016/j.jallcom.2020.158034

[206] Karapuzha AS, Fraser D, Zhu Y, Wu X, Huang A (2022) Effect of solution heat treatment and hot isostatic pressing on the microstructure and mechanical properties of Hastelloy X manufactured by electron beam powder bed fusion. J Mater Sci Technol 98:99–117. https://doi.org/10.1016/j.jmst.2021.04.059

[207] Kreitcberg A, Brailovski V, Turenne S (2017) Elevated temperature mechanical behavior of IN625 alloy processed by laser powder-bed fusion. Mater Sci Eng A 700:540–553. https://doi.org/10.1016/j.msea.2017.06.045

[208] Li J, Zhao Z, Bai P, Qu H, Liu B, Li L, Wu L, Guan R, Liu H, Guo Z (2019) Microstructural evolution and mechanical properties of IN718 alloy fabricated by selective laser melting following different heat treatments. J Alloys Compd 772:861–870. https://doi.org/10.1016/j.jallcom.2018.09.200

[209] Chlebus E, Gruber K, Kuźnicka B, Kurzac J, Kurzynowski T (2015) Effect of heat treatment on the microstructure and mechanical properties of Inconel 718 processed by selective laser melting. Mater Sci Eng A 639:647–655. https://doi.org/10.1016/j.msea.2015.05.035

[210] Hariharan A, Lu L, Risse J, Kostka A, Gault B, Jägle EA, Raabe D (2019) Misorientation-dependent solute enrichment at interfaces and its contribution to defect formation mechanisms during laser additive manufacturing of superalloys. Phys Rev Mater 3:123602. https://doi.org/10.1103/PhysRevMaterials.3.123602

[211] Miner RV, Castelli MG (1992) Hardening mechanisms in a dynamic strain aging alloy, Hastelloy X, during isothermal and thermomechanical cyclic deformation. Metall Trans A 23:551–561. https://doi.org/10.1007/BF02801173

[212] Tomus D, Jarvis T, Wu X, Mei J, Rometsch P, Herny E, Rideau JF, Vaillant S (2013) Controlling the microstructure of Hastelloy-X components manufactured by selective laser melting. Phys Procedia 41:823–827. https://doi.org/10.1016/j.phpro.2013.03.154

[213] Han Q, Gu Y, Setchi R, Lacan F, Johnston R, Evans SL, Yang S (2019) Additive manufacturing of high-strength crack-free Ni-based Hastelloy X superalloy. Addit Manuf 30:100919. https://doi.org/10.1016/j.addma.2019.100919

[214] Dantzig JA, Rappaz M (2009) Solidification. CRC Press, Boca Raton

[215] Montero-Sistiaga ML, Pourbabak S, Van Humbeeck J, Schryvers D, Vanmeensel K (2019) Microstructure and mechanical properties of Hastelloy X produced by HP-SLM (high power selective laser melting). Mater Des 165:107598. https://doi.org/10.1016/j.matdes.2019.107598

[216] Wang F (2012) Mechanical property study on rapid additive layer manufacture Hastelloy® X alloy by selective laser melting technology. Int J Adv Manuf Technol 58:545–551. https://doi.org/10.1007/s00170-011-3423-2

[217] Huang X, Zhang Y, Liu Y, Hu Z (1997) Effect of small amount of nitrogen on carbide characteristics in unidirectional Ni-base superalloy. Metall Mater Trans A Phys Metall Mater Sci 28:2143–2147. https://doi.org/10.1007/s11661-997-0172-9

[218] Mitchell A, Schmalz AJ, Schvezov C, Cockroft SL (1994) The precipitation of primary carbides in Alloy 718. Superalloys 718(625):65–78. https://doi.org/10.7449/1994/Superalloys_1994_65_78

[219] Xu J, Ma T, Peng RL, Hosseini S (2021) Effect of post-processes on the microstructure and mechanical properties of laser powder bed fused IN718 superalloy. Addit Manuf 48:102416. https://doi.org/10.1016/j.addma.2021.102416

[220] Zhao Y, Li K, Gargani M, Xiong W (2020) A comparative analysis of Inconel 718 made by additive manufacturing and suction casting: Microstructure evolution in homogenization. Addit Manuf 36:101404. https://doi.org/10.1016/j.addma.2020.101404

[221] Sui S, Li Z, Zhong C, Zhang Q, Gasser A, Chen J, Chew Y, Bi G (2021) Laves phase tuning for enhancing high temperature mechanical property improvement in laser directed energy deposited Inconel 718. Compos Part B Eng 215:108819. https://doi.org/10.1016/j.compositesb.2021.108819

[222] Antonsson T, Fredriksson H (2005) The effect of cooling rate on the solidification of INCONEL 718. Metall Mater Trans B 36:85–96

[223] Rielli VV, Piglione A, Pham MS, Primig S (2022) On the detailed morphological and chemical evolution of phases during laser powder bed fusion and common post-processing heat treatments of IN718. Addit Manuf 50:102540. https://doi.org/10.1016/j.addma.2021.102540

[224] Lee YS, Kirka MM, Kim S, Sridharan N, Okello A, Dehoff RR, Babu SS (2018) Asymmetric cracking in Mar-M247 alloy builds during electron beam powder bed fusion additive manufacturing. Metall Mater Trans A Phys Metall Mater Sci 49:5065–5079. https://doi.org/10.1007/s11661-018-4788-8

[225] Davidson MW, Abramowitz M (2002) Optical microscopy. In: Hornak JP (ed) Encyclopedia of imaging science and technology. John Wiley & Sons Inc., Hoboken. https://doi.org/10.1002/0471443395.img074

[226] Kanagarajah P, Brenne F, Niendorf T, Maier HJ (2013) Inconel 939 processed by selective laser melting: effect of microstructure and temperature on the mechanical properties under static and cyclic loading. Mater Sci Eng A 588:188–195. https://doi.org/10.1016/j.msea.2013.09.025

[227] Huynh T, Mehta A, Graydon K, Woo J, Park S, Hyer H, Zhou L, Imholte DD, Woolstenhulme NE, Wachs DM, Sohn Y (2022) Microstructural development in Inconel 718 nickel-based superalloy additively manufactured by laser powder bed fusion. Metallogr Microstruct Anal 11:88–107. https://doi.org/10.1007/s13632-021-00811-0

[228] Tillmann W, Schaak C, Nellesen J, Schaper M, Aydinöz ME, Hoyer KP (2017) Hot isostatic pressing of IN718 components manufactured by selective laser melting. Addit Manuf 13:93–102. https://doi.org/10.1016/j.addma.2016.11.006

[229] Liu SY, Li HQ, Qin CX, Zong R, Fang XY (2020) The effect of energy density on texture and mechanical anisotropy in selective laser melted Inconel 718. Mater Des 191:108642. https://doi.org/10.1016/j.matdes.2020.108642

[230] Radavich JF (1988) Metallography of Alloy 718. JOM 40:42–43. https://doi.org/10.1007/BF03258150

[231] Voort GFV (2003) Metallography of superalloys. Ind Heat 70:40

[232] Foxman Z, Sobol OV, Pinkas M, Landau A, Hähner P, Krsjak V, Meshi L (2012) Microstructural evolution of Cr-Rich ODS steels as a function of heat treatment at 475 °C. Metallogr Microstruct Anal 1:158–164. https://doi.org/10.1007/s13632-012-0028-6

[233] Renderos M, Girot F, Lamikiz A, Torregaray A, Saintier N (2016) Ni based powder reconditioning and reuse for LMD process. Phys Procedia 83:769–777. https://doi.org/10.1016/j.phpro.2016.08.079

[234] Keshavarzkermani A, Marzbanrad E, Esmaeilizadeh R, Mahmoodkhani Y, Ali U, Enrique PD, Zhou NY, Bonakdar A, Toyserkani E (2019) An investigation into the effect of process parameters on melt pool geometry, cell spacing, and grain refinement during laser powder bed fusion. Opt Laser Technol 116:83–91. https://doi.org/10.1016/j.optlastec.2019.03.012

[235] Zaefferer S, Elhami NN (2014) Theory and application of electron channelling contrast imaging under controlled diffraction conditions. Acta Mater 75:20–50. https://doi.org/10.1016/j.actamat.2014.04.018

[236] Goldstein J, Newbury D, Joy D, Lyman C, Echlin P, Lifshin E, Sawyer L, Michael J (2003) Scanning electron microscopy and X-Ray microanalysis, 3rd edn. Springer Science & Business Media, New York

[237] Humphreys FJ, Bate PS, Hurley PJ (2001) Orientation averaging of electron backscattered diffraction data. J Microsc 201:50–58. https://doi.org/10.1046/j.1365-2818.2001.00777.x

[238] Dehoff RR, Kirka MM, Sames WJ, Bilheux H, Tremsin AS, Lowe LE, Babu SS (2015) Site specific control of crystallographic grain orientation through electron beam additive manufacturing. Mater Sci Technol 31:931–938. https://doi.org/10.1179/1743284714Y.0000000734

[239] Leicht A, Rashidi M, Klement U, Hryha E (2020) Effect of process parameters on the microstructure, tensile strength and productivity of 316L parts produced by laser powder bed fusion. Mater Charact 159:110016. https://doi.org/10.1016/j.matchar.2019.110016

[240] Serrano-Munoz I, Mishurova T, Thiede T, Sprengel M, Kromm A, Nadammal N, Nolze G, Saliwan-Neumann R, Evans A, Bruno G (2020) The residual stress in as-built Laser Powder Bed Fusion IN718 alloy as a consequence of the scanning strategy induced microstructure. Sci Rep 10:1–15. https://doi.org/10.1038/s41598-020-71112-9

[241] Polonsky AT, Raghavan N, Echlin MP, Kirka MM, Dehoff RR, Pollock TM (2020) 3D Characterization of the columnar-to-equiaxed transition in additively manufactured Inconel 718. Miner Met Mater Ser 2020:990–1002. https://doi.org/10.1007/978-3-030-51834-9_97

[242] Witzen WA, Polonsky AT, Pollock TM, Beyerlein IJ (2020) Three-dimensional maps of geometrically necessary dislocation densities in additively manufactured Ni-based superalloy IN718. Int J Plast 131:102709. https://doi.org/10.1016/j.ijplas.2020.102709

[243] Carter CB, Williams DB (eds) (2016) Transmission electron microscopy. Springer International Publishing, Cham. https://doi.org/10.1007/978-3-319-26651-0

[244] Wirth R (2009) Focused Ion Beam (FIB) combined with SEM and TEM: advanced analytical tools for studies of chemical composition, microstructure and crystal structure in geomaterials on a nanometre scale. Chem Geol 261:217–229. https://doi.org/10.1016/j.chemgeo.2008.05.019

[245] Segura IA, Murr LE, Terrazas CA, Bermudez D, Mireles J, Injeti VSV, Li K, Yu B, Misra RDK, Wicker RB (2019) Grain boundary and microstructure engineering of Inconel

690 cladding on stainless-steel 316L using electron-beam powder bed fusion additive manufacturing. J Mater Sci Technol 35:351–367. https://doi.org/10.1016/j.jmst.2018.09.059

[246] Fultz B, Howe J (2013) Transmission electron microscopy and diffractometry of materials. Springer, Berlin. https://doi.org/10.1007/978-3-642-29761-8

[247] Griffiths S, Ghasemi Tabasi H, Ivas T, Maeder X, De Luca A, Zweiacker K, Wróbel R, Jhabvala J, Logé RE, Leinenbach C (2020) Combining alloy and process modification for micro-crack mitigation in an additively manufactured Ni-base superalloy. Addit Manuf 36:101443. https://doi.org/10.1016/j.addma.2020.101443

[248] Wang X, Carter LN, Pang B, Attallah MM, Loretto MH (2017) Microstructure and yield strength of SLM-fabricated CM247LC Ni-Superalloy. Acta Mater 128:87–95. https://doi.org/10.1016/j.actamat.2017.02.007

[249] Unocic KA, Kolbus LM, Dehoff RR, Dryepondt SN, Pint BA (2014) High-temperature performance of UNS N07718 processed by additive manufacturing. NACE Corros 2014

[250] Zheng H, Meng YS, Zhu Y (2015) Frontiers of in situ electron microscopy. MRS Bull 40:12–18. https://doi.org/10.1557/mrs.2014.305

[251] Field RD, Papin PA (2004) Location specific in situ TEM straining specimens made using FIB. Ultramicroscopy 102:23–26. https://doi.org/10.1016/j.ultramic.2004.08.002

[252] Tomus D, Ng HP (2013) In situ lift-out dedicated techniques using FIB–SEM system for TEM specimen preparation. Micron 44:115–119. https://doi.org/10.1016/j.micron.2012.05.006

[253] Li J, Malis T, Dionne S (2006) Recent advances in FIB–TEM specimen preparation techniques. Mater Charact 57:64–70. https://doi.org/10.1016/j.matchar.2005.12.007

[254] Andersson H, Persson C (2004) In-situ SEM study of fatigue crack growth behaviour in IN718. Int J Fatigue 26:211–219. https://doi.org/10.1016/S0142-1123(03)00172-5

[255] McKeown JT, Zweiacker K, Liu C, Coughlin DR, Clarke AJ, Baldwin JK, Gibbs JW, Roehling JD, Imhoff SD, Gibbs PJ, Tourret D, Wiezorek JMK, Campbell GH (2016) Time-resolved in situ measurements during rapid alloy solidification: experimental insight for additive manufacturing. JOM 68:985–999. https://doi.org/10.1007/s11837-015-1793-x

[256] Daryadel S, Behroozfar A, Minary-Jolandan M (2019) A microscale additive manufacturing approach for in situ nanomechanics. Mater Sci Eng A 767:138441. https://doi.org/10.1016/j.msea.2019.138441

[257] Koul S, Zhou L, Ahmed O, Sohn Y, Jiang T, Kushima A (2021) In situ TEM characterization of microstructure evolution and mechanical behavior of the 3D-printed Inconel 718 exposed to high temperature. Microsc Microanal 27:250–256. https://doi.org/10.1017/S1431927621000052

[258] Koul S, Zhou L, Sohn Y, Kushima A (2018) Microstructure and mechanical behavior of the 3D printed Inconel 718: in-situ TEM study. Microsc Microanal 24:1942–1943. https://doi.org/10.1017/s143192761801019x

[259] Sneddon GC, Trimby PW, Cairney JM (2016) Transmission Kikuchi diffraction in a scanning electron microscope: a review. Mater Sci Eng R Rep 110:1–12. https://doi.org/10.1016/j.mser.2016.10.001

[260] Trimby PW (2012) Orientation mapping of nanostructured materials using transmission Kikuchi diffraction in the scanning electron microscope. Ultramicroscopy 120:16–24. https://doi.org/10.1016/j.ultramic.2012.06.004

[261] Tang YT, Ghoussoub JN, Panwisawas C, Collins DM, Amirkhanlou S, Clark JWG, Németh AAN, McCartney DG, Reed RC (2020) The effect of heat treatment on tensile yielding response of the new superalloy ABD-900AM for additive manufacturing. Springer International Publishing, Chem. https://doi.org/10.1007/978-3-030-51834-9_103

[262] Tang YT, Campbell JE, Burley M, Dean J, Reed RC, Clyne TW (2021) Profilometry-based indentation plastometry to obtain stress-strain curves from anisotropic superalloy components made by additive manufacturing. Materialia 15:101017. https://doi.org/10.1016/j.mtla.2021.101017

[263] Gault B, Moody MP, Cairney JM, Ringer SP (2012) Atom probe microscopy. Springer Science & Business Media, New York

[264] I. Blum, F. Cuvilly, W. Lefebvre-Ulrikson (2016) Atom probe sample preparation. In: Atom Probe Tomography. Amsterdam: Elsevier, pp 97–121

[265] Miller MK, Russell KF, Thompson K, Alvis R, Larson DJ (2007) Review of atom probe FIB-based specimen preparation methods. Microsc Microanal 13:428–436. https://doi.org/10.1017/S1431927607070845

[266] Babinsky K, De Kloe R, Clemens H, Primig S (2014) A novel approach for site-specific atom probe specimen preparation by focused ion beam and transmission electron backscatter diffraction. Ultramicroscopy 144:9–18. https://doi.org/10.1016/j.ultramic.2014.04.003

[267] Rielli VV, Theska F, Primig S (2021) Correlative approach for atom probe sample preparation of interfaces using plasma focused ion beam without lift-out. Microsc Microanal 28:1–11. https://doi.org/10.1017/S1431927621000349

[268] Larson DJ, Prosa TJ, Ulfig RM, Geiser BP, Kelly TF (2013) Local Electrode atom probe tomography. Springer, New York

[269] Lefebvre-Ulrikson W, Da Costa G, Rigutti L, Blum I (2016) Data mining. Elsevier Inc., Amsterdam

[270] Kontis P, Chauvet E, Peng Z, He J, da Silva AK, Raabe D, Tassin C, Blandin JJ, Abed S, Dendievel R, Gault B, Martin G (2019) Atomic-scale grain boundary engineering to overcome hot-cracking in additively-manufactured superalloys. Acta Mater 177:209–221. https://doi.org/10.1016/j.actamat.2019.07.041

[271] Cloots M, Uggowitzer PJ, Wegener K (2016) Investigations on the microstructure and crack formation of IN738LC samples processed by selective laser melting using Gaussian and doughnut profiles. Mater Des 89:770–784. https://doi.org/10.1016/j.matdes.2015.10.027

[272] Philippe T, De Geuser F, Duguay S, Lefebvre W, Cojocaru-Mirédin O, Da Costa G, Blavette D (2009) Clustering and nearest neighbour distances in atom-probe tomography. Ultramicroscopy 109:1304–1309. https://doi.org/10.1016/j.ultramic.2009.06.007

[273] De Geuser F, Gault B (2020) Metrology of small particles and solute clusters by atom probe tomography. Acta Mater 188:406–415. https://doi.org/10.1016/j.actamat.2020.02.023

[274] Cullity BD (1956) Elements of X-ray diffraction. Addison-Wesley Publishing, Boston

[275] Li L, Gong X, Ye X, Teng J, Nie Y, Li Y, Lei Q (2018) Influence of building direction on the oxidation behavior of Inconel 718 alloy fabricated by additive manufacture of electron beam melting. Materials (Basel) 11:2549. https://doi.org/10.3390/ma11122549

[276] Murr LE, Martinez E, Gaytan SM, Ramirez DA, MacHado BI, Shindo PW, Martinez JL, Medina F, Wooten J, Ciscel D, Ackelid U, Wicker RB (2011) Microstructural architecture, microstructures, and mechanical properties for a nickel-base superalloy fabricated by electron beam melting. Metall Mater Trans A Phys Metall Mater Sci 42:3491–3508. https://doi.org/10.1007/s11661-011-0748-2

[277] Wiedemann H (2003) Synchrotron radiation. In: Wiedemann H (ed) Particle accelerator physics. Springer, Berlin, pp 647–686

[278] Ioannidou C, König H-H, Semjatov N, Ackelid U, Staron P, Körner C, Hedström P, Lindwall G (2022) In-situ synchrotron X-ray analysis of metal additive manufacturing: current state, opportunities and challenges. Mater Des 219:110790. https://doi.org/10.1016/j.matdes.2022.110790

[279] Willmott P (2019) An introduction to synchrotron radiation: techniques and applications. John Wiley & Sons, Hoboken

[280] Feigin LA, Svergun DI (1987) Structure analysis by small-angle X-ray and neutron scattering. Springer, Boston

[281] Guinier A, Fournet G, Yudowitch KL (1955) Small-angle scattering of X-rays. Wiley, New York

[282] Idell Y, Levine LE, Allen AJ, Zhang F, Campbell CE, Olson GB, Gong J, Snyder DR, Deutchman HZ (2016) Unexpected δ-phase formation in additive-manufactured Ni-based superalloy. JOM 68:950–959. https://doi.org/10.1007/s11837-015-1772-2

[283] Zhang F, Levine LE, Allen AJ, Stoudt MR, Lindwall G, Lass EA, Williams ME, Idell Y, Campbell CE (2018) Effect of heat treatment on the microstructural evolution of a nickel-based superalloy additive-manufactured by laser powder bed fusion. Acta Mater 152:200–214. https://doi.org/10.1016/j.actamat.2018.03.017

[284] Wahlmann B, Galgon F, Stark A, Gayer S, Schell N, Staron P, Körner C (2019) Growth and coarsening kinetics of gamma prime precipitates in CMSX-4 under simulated additive manufacturing conditions. Acta Mater 180:84–96. https://doi.org/10.1016/j.actamat.2019.08.049

[285] Wahlmann B, Krohmer E, Breuning C, Schell N, Staron P, Uhlmann E, Körner C (2021) In situ observation of γ′ phase transformation dynamics during selective laser melting of CMSX-4. Adv Eng Mater 23:2100112. https://doi.org/10.1002/adem.202100112

[286] Pesach A, Tiferet E, Vogel SC, Chonin M, Diskin A, Zilberman L, Rivin O, Yeheskel O, Caspi EN (2018) Texture analysis of additively manufactured Ti-6Al-4V using neutron diffraction. Addit Manuf 23:394–401. https://doi.org/10.1016/j.addma.2018.08.010

[287] Kumar S, Kamath R, Nandwana P, Chen Y, Babu S (2020) Dynamic phase transformations in additively manufactured Ti-6Al-4V during thermo-mechanical gyrations. Materialia 14:100883. https://doi.org/10.1016/j.mtla.2020.100883

[288] Neikter M, Woracek R, Durniak C, Persson M, Antti M-L, Åkerfeldt P, Pederson R, Zhang J, Vogel SC, Strobl M (2020) Texture of electron beam melted Ti-6Al-4V measured with neutron diffraction. MATEC Web Conf 321:03021. https://doi.org/10.1051/matecconf/202032103021

[289] Qin H, Bi Z, Yu H, Feng G, Zhang R, Guo X, Chi H, Du J, Zhang J (2018) Assessment of the stress-oriented precipitation hardening designed by interior residual stress during ageing in IN718 superalloy. Mater Sci Eng A 728:183–195. https://doi.org/10.1016/j.msea.2018.05.016

[290] I.S. Organization (2019) Non-destructive testing—Standard test method for determining residual stresses by neutron diffraction, ISO 21432. 12.

[291] Hutchings MT, Withers PJ, Holden TM, Lorentzen T (2005) Introduction to the characterization of residual stress by neutron diffraction. CRC Press, Boca Raton

[292] Cakmak E, Watkins TR, Bunn JR, Cooper RC, Cornwell PA, Wang Y, Sochalski-Kolbus LM, Dehoff RR, Babu SS (2016) Mechanical characterization of an additively manufactured Inconel 718 Theta-shaped specimen. Metall Mater Trans A Phys Metall Mater Sci 47:971–980. https://doi.org/10.1007/s11661-015-3186-8

[293] Sochalski-Kolbus LM, Payzant EA, Cornwell PA, Watkins TR, Babu SS, Dehoff RR, Lorenz M, Ovchinnikova O, Duty C (2015) Comparison of residual stresses in Inconel 718 simple parts made by electron beam melting and direct laser metal sintering. Metall Mater Trans A 46:1419–1432. https://doi.org/10.1007/s11661-014-2722-2

[294] Goel S, Neikter M, Capek J, Polatidis E, Colliander MH, Joshi S, Pederson R (2020) Residual stress determination by neutron diffraction in powder bed fusion-built Alloy 718: influence of process parameters and post-treatment. Mater Des 195:109045. https://doi.org/10.1016/j.matdes.2020.109045

[295] Pant P, Proper S, Luzin V, Sjöström S, Simonsson K, Moverare J, Hosseini S, Pacheco V, Peng RL (2020) Mapping of residual stresses in as-built Inconel 718 fabricated by laser powder bed fusion: a neutron diffraction study of build orientation influence on residual stresses. Addit Manuf 36:101501. https://doi.org/10.1016/j.addma.2020.101501

[296] Pollock TM, Clarke AJ, Babu SS (2020) Design and tailoring of alloys for additive manufacturing. Metall Mater Trans A Phys Metall Mater Sci 51:6000–6019. https://doi.org/10.1007/s11661-020-06009-3